3D Bioprinting Pediatric Trachea

A Dissertation
SUBMITTED TO THE FACULTY OF
THE UNIVERSITY OF MINNESOTA
By

Zachary Galliger

IN PARTIAL FULFILMENT OF THE REQUIREMENTS
FOR THE DEGREE OF
DOCTOR OF PHILOSOPHY

Angela Panoskaltsis-Mortari PhD, Brenda Ogle PhD

February 2022

Acknowledgments

I want to acknowledge and thank the many people, departments, and resources that not only made thesis possible, but helped me preserve through countless challenges.

Firstly, I would like to thank my funding sources: the Biomedical Engineering department, the department of Pediatrics in the Division of Blood and Marrow Transplant & Cellular Therapy, National Institutes of Health (NHLBI), and the Clinical & Translational Science Institute (CTSI), without which I would have not been able to do any of the work in this thesis.

I would like to thank the labs and facilities across campus that have helped me learn so much. Thank you to the UMN Visible Heart Lab for your reliable supply of porcine tissues. Thank you to the UMN Polymer Characterization Facility and David Giles for teaching me about rheometry and training me on their instruments. Thank you to the Minnesota Dental Research Center for Biomaterials and Biomechanics and Bonnie VanHeel for teaching me about micro CT and 3D reconstruction. Thank you to the UMN CSE Characterization Facility and Dr. John C. Nelson for teaching about nanoindentation. I would like to thank the Center for Mass Spectrometry & Proteomics, Todd Markowski, and LeeAnn Higgins for teaching about proteomics. Dr. James Wollack from St. Catherine University for his help in developing our gelatin methacrylate synthesis protocol. I would also like to thank the BME department administrative staff, especially Rachel Jorgenson, for their patience and help throughout my PhD. I would like to thank the Pediatrics department administrative staff for their support and guidance when things went wrong, especially Emily Kukacka, Lisa Gow, and Brett Steger.

I would like to thank my surgical collaborators Dr. Benjamin Zhang, Dr. Ilitch Diaz Gutierrez, and mentor Dr. Rafael Andrade for teaching me about *in vivo* research and spending hours in the operating room with me over their shoulders. I would also like to thank Experimental Surgical Services and specifically Peggy Norris, Teri Ulferts, and Michele Dunning for their help both during surgeries and in preparation for our animal protocols navigating IACUC.

I would like to thank my other lab members, without whom everyone step of this process would have 1000 times harder. I would like to thank Carolyn Meyer for her support and training in the lab's protocols. I would like to thank Caleb Vogt and Iffy Akinnola for their help as sounding boards and experimental design consultants. I would like to thank Haylie Helms for her support and enthusiasm for science, reminding me near the end of PhD why I started. I would like to thank my undergraduate and high school mentees Jennifer Day, Avni Jain, and George Lyu for their curiosity and dedication to science.

I would like to thank my advisors. Dr. Angela Panoskaltsis-Mortari has been an invaluable mentor for my graduate career. Without her support, humor, and patience I would not be where I am today. Dr. Brenda Ogle has been a fantastic resource and an excellent reminder to keep my work focused and aware of the greater context.

If an army marches on its stomach, it is equally true that a graduate student is run on caffeine. I would like thank Starbucks, Caribou Coffee, and Espresso Expose for providing countless gallons of coffee.

Dedication

This thesis is dedicated to my family and my friends who have supported me on this journey.

Abstract

Tracheal failures due to trauma, disease, or congenital anomalies, if not fatal, severely decrease quality of life. While small defects can be resolved surgically with resection and anastomosis, defects exceeding a critical length of trachea require graft material. This critical length varies from 50% in adults to 30% in children. Current silicone grafts pose further challenges for pediatric patients, who require yearly follow up surgeries to adjust the implant to their growing bodies. To assuage these challenges, the work in this thesis seeks to develop biologically derived grafts with the potential to grow and respond to the needs of pediatric patients. First, this work focuses on incorporating extracellular matrix (ECM) into bioinks for 3D bioprinting patient specific, tissue engineered constructs. The results discussed in this dissertation show while ECM is a powerful mediator of cell behavior, its efficacy can be inhibited by chemical modification. Lastly, this work investigates an *in vivo* rabbit model for evaluating tracheal transplants and poses further questions concerning the regenerative capabilities of tracheal cartilage.

Table of Contents

List of Tables

List of Figures

Chapter 1 Introduction

The material in this Chapter is adapted from:

Galliger Z, Vogt CD, Panoskaltsis-Mortari A. 3D bioprinting for lungs and hollow organs. Translational Research. 2019;211:19-34. doi:10.1016/j.trsl.2019.05.001[1]

1.1: The Trachea

The trachea is a simple but vital organ whose failure can be acutely fatal [2]. Tracheal failure primarily pertains to obstruction of the airway. While there are several treatment options for minor cases, large scale defects, such as congenital atresia, require a graft replacement. Robust, solid, synthetic materials such as silicone are used to replace the diseased tissue. However, these implants present several challenges when used to treat pediatric patients since they cannot grow with the child, requiring multiple replacement surgeries over their lifetime. This thesis work seeks to develop strategies for biologically derived tracheal grafts produced from porcine tracheal cartilage and human cells, with the potential to grow with the pediatric patient.

1.1.1: Tracheal Anatomy

The trachea begins at the end of the larynx and branches into the main bronchi of the lungs. It is composed of 16 to 20 cartilaginous crescent shaped rings, which resist compressive force to the throat and hold the airway open during inhalation.[3] Small sections of transverse smooth muscle connect to either end of the crescents completing the posterior portion of each ring, this region is overlapped transversely by a layer of smooth muscle running along the entire length of the trachea. These rings are further secured by two fibro-elastic membranes, a thinner membrane on the luminal side and a thicker one on the outer layer. The lumen of the trachea is lined by a ciliated epithelium and mucosa which clears the airway of debris.

At birth, the trachea is on average 5 cm long and roughly circular with an inner diameter of 4 to 5 mm. As the trachea grows it becomes more oblong, reaching inner diameters of 10-27 mm sagittally and 10-25 mm coronally. The final adult human length between 8.5 cm to 15 cm is reached at around 14 years of age, but may continue to dilate.[4] On average the male trachea is 11 cm, slightly longer than the female trachea at 10 cm. The length of the trachea is also dynamic, able to increase by 25% during respiration and hyperflexion.[3]

1.1.2: Tracheal Failure

The most common disease state is tracheal stenosis, it is estimated that there are 4.9 severe stenosis cases per million each year in the general population.[5] Tracheal stenosis has many potential causes including perichondritis, chondritis, tumors, burns, trauma, congenital hypoplasia, malformed tracheal rings, and post-intubation injury.[6] During intubation, the endotracheal tube may damage the epithelial lining of the trachea. The damaged region then signals the surrounding cells to proliferate and begin the wound healing process, often forming scar tissue. Excess scar tissue may then grow into the airway, causing the stenosis.[7,8] Less common but equally challenging is tracheal malacia, where the cartilaginous rings of the trachea are either misshaped or weakened. Without the support of the cartilage, the airway can collapse during inhalation and suffocate the patient.[9] This can be caused by a congenital defect, acquired as a result of prolonged intubation, or severe tracheobronchitis. Specifically affecting pediatric patients are congenital defects, such as tracheal atresia, the complete absence of the trachea, often coinciding with the absence of the esophagus.[10,11] In addition, tracheoesophageal fistula is the fusion of the trachea and esophagus, which creates many issues.[12]

1.1.3: Current Treatments & Limitations

Current treatments for tracheal failure focus on reshaping or clearing diseased tissue but most are only effective on small areas. Bronchoscopic tracheal dilation uses an inflatable balloon or other tools to force the walls of a stenotic trachea open. Unfortunately, it usually only relieves symptoms for a short time, but allows physicians to examine the extent of stenosis.[13] Laser bronchoscopy can be used to remove scar tissue blocking the airway, but may cause further scar formation and exacerbate stenosis long term.[14] Tracheo-bronchial airway stents function similarly to cardiovascular stents, holding the walls of the airway open with a metal mesh. However, they can damage the epithelial lining or be dislodged and expelled from the airway. [5]

The few permanent solutions are surgical. Slide tracheoplasty is the most common treatment for stenosis, where the affected region is surgically excised and the remaining tissue is anastomosed.[15] However, this technique is ineffective when the damaged portion of the trachea reaches a critical length. In adults, that length is anything greater than 50% of the trachea, on average 6 cm or more.[6] For pediatric patients that length can be as little as 30% of the total trachea, ranging between 1 and 3 cm.[16] In these cases, the current standard is a tracheostoma, where the lower remnant of the trachea is surgically anchored to the exterior of the neck.[6] Unfortunately, this procedure raises concerns on quality of life. This essentially bypasses the upper respiratory system including the sinuses and larynx, eliminating the body's natural air quality conditioning system and making speech more challenging. If there is an insufficient length of trachea to even accomplish this, an implant must be used to replace the lost tissue.

Many tissues and materials have been investigated as replacement tissues with mixed results. The obvious first choice would be a compatible, cadaveric allograft, however these often fail to properly engraft and are rejected by the host.[17] Even tracheal autografts, momentarily separated from the surrounding tissue, often fail because the revascularization is insufficient to support the transplanted cells.[17] Synthetic materials such as silicone tubes have also been used to replace the airway, but they lack the epithelial layer needed for normal transport of mucous and cannot adapt to growing patients.

There have been many attempts to engineer tracheal tissue, but most have relied on a synthetic component to provide mechanical strength which cannot serve as a long-term solution for pediatric patients, because the material cannot grow over time.[18–22] Pediatric patients require multiple surgeries until their airway reaches its terminal size. These engineered constructs also face challenges integrating with the host tissue. The most promising approach so far has been transplanting decellularized, cadaveric tracheal tissue seeded with the patient’s own cells but there have been mixed results with severe complications.[23,24] Decellularization of the donor tissue removes most antigenic components and, combined with recolonizing the tissue with autologous cells, minimizes the need for immune suppression. However, the cartilage tissue can lose mechanical strength through the decellularization process and does not fully recolonize, leaving large acellular regions in the construct.

1.2: Current 3D Bioprinting Approaches

Over the last decade, 3D bioprinting has emerged as a promising technology to rapidly produce patient-specific tissue constructs.[25] Bioprinting, as opposed to regular 3D printing, involves the layer-by-layer deposition of biologically-derived materials or cells.[26] There are multiple modalities, but often they can be categorized as acellular printing with subsequent recellularization versus direct printing with cells suspended in a “bioink”.[27] Compared to cell-sheet engineering techniques, 3D bioprinting has an advantage of creating more complex architectures. It also has the potential to address problems of insufficient cell ingrowth into decellularized matrices, since cells can be introduced directly throughout the volume of the bioprinted construct. There is an ever-growing number of methods for material deposition, and each has its limitations. Laser-based printers can achieve single-cell resolution but cannot quickly produce large volumes of material, whereas extrusion-based printers can print quickly but are generally limited to a resolution of approximately 100 microns.[28] Possibly the greatest benefit of 3D bioprinters in airway tissue engineering is the ability to create hollow structures with multiple layers of different cells and materials.

1.2.1: Dual-Headed Printing:

In a recent study by Kaye et al., a dual-headed system was used to print both polycaprolactone (**PCL**) and an alginate/collagen I hydrogel using a partial ring segment design.[29] The hydrogel used was a 50/50 blend of 3% alginate and a 2.8 mg/ml collagen type 1 hydrogel, seeded with chondrocytes from rabbit tracheal cartilage. Using a dual-head extruder, a layer of PCL was printed, allowed to cool, then followed by a layer of hydrogel. The completed graft was then implanted in New Zealand white rabbits. The opening of the graft aligned with the trachealis muscle, which runs vertically on the posterior of the trachea. These grafts were harvested at three or six weeks after implantation. The cartilage formation was histologically evaluated using the modified O'Driscoll score, a histological scoring system that evaluates cartilage regeneration.[30] While there was not a significant difference in scores between the two time points, the score was higher at either end of the graft where it overlapped native tissue compared to the center, indicating better cartilage growth. Unfortunately, all grafts had significant stenosis. The authors noted decreased inflammation where native tracheal epithelium had grown over the graft, acting as a boundary. The authors suggested that this boundary may decrease the shear stress on the graft from the air or isolate the graft from fluids in the airway. Either of these mechanisms could be replicated by seeding the airway with autologous epithelial cells in future constructs.

One major advantage of bioprinting, compared to other fabrication methods, is the ability to print complex patterns within a larger geometry. Exploring this benefit, Bae et al. produced a tracheal graft made of alternating layers of PCL and cell-laden alginate printed in overlapping patterns.[31] A diagram of this method is shown in **Figure 1-1A**. PCL was printed in the diagonal grids for the first and fifth layers, providing structural support while leaving negative space for nutrient transport. The center layers were helical form. The second and fourth layers were alginate seeded with epithelial cells and mesenchymal stromal cells (**MSCs**) respectively, with a layer of PCL between them. This resulted in a mechanically robust graft. These grafts were implanted in New Zealand white rabbits and observed for twelve weeks. Over this time course, there were no significant respiratory complications or stenoses. Epithelial mucosa over the entire defect area was observed as well as localized neo-cartilage formation. This work was followed up by Park et al, with a longer *in vivo* study examining the grafts up to one year post implant.[32] After 3 months, histology revealed ciliated epithelium on the bioprinted grafts, while the PCL-alone controls had only granulated tissue. Immature cartilage islets were seen after 6 months, but they did not form cartilage rings. These promising survival results exemplify the benefits of 3D bioprinting, based on strategic patterning of both matrix and cells.

1.2.2: Organoid Printing:

Shifting away from using polymers, Taniguchi et al. used a removable needle array to organize spherical organoids into a tracheal structure. Rat chondrocytes, endothelial cells, and MSCs were combined in pellet culture to form cell aggregates.[33]

Aggregated spheroids were then assembled into a tracheal construct in a needle array. After 7 days, the needles were removed, and a stent was placed in the lumen to prevent lumen compaction. The construct was moved to a bioreactor for 28 days. The mature construct was then implanted in an isogenic rat, with the stent included for 23 days. This process is illustrated in **Figure 1-1B**. Microvessels with red blood cells were observed in the graft after 8 days *in vivo*. Further study is needed to verify whether the seeded endothelial cells accelerated *in vivo* vascularization, and whether the microvessels were host or donor-derived.

This approach was expanded by Machino et al, incorporating layers of fibroelastic tissue between the cartilage organoids, more like the native trachea.[34] Cartilaginous organoids were made by coculturing normal human articular chondrocytes (NHACs), human umbilical vein endothelial cells (HUVECs), and MSCs. Fibrous organoids were made using HUVECs, MSCs, and normal human dermal fibroblasts (NHDFs). These organoids were stacked in alternating layers in the needle array to mimic the rings of the trachea. These constructs were kept on the needle array for 7 days, then moved to a bioreactor to mature for 28 days. The mature grafts were then implanted in a rat model, supported by a silicone stent, and examined 7 days and 35 days after implant. Sections from 7 days *in vivo* show aggregates of CD31+ cells, indicating nascent vessel formation. At day 35 CD31+ staining showed more mature vessels with larger lumens. After 35 days *in vivo*, pan-cytokeratin positive cells were also present, suggesting the spread of the epithelium from the native tissue. This approach is well-suited for larger airways, but it may have challenges in creating smaller airways and vasculature. With small airways and alveoli, the lumens may be on a similar scale as the needles in the array, leaving significant holes in the tissue. To address this challenge, alternative support strategies should be investigated. Other printing methods use support baths of sacrificial materials, such as a slurry of gelatin microparticles in the freeform reversible embedding of suspended hydrogels (FRESH) method for printing low viscosity bioinks.[35] While gelatin is not suitable for supporting tissue geometry long term, similar approaches using other materials may be explored.

1.3: Bioprinting-Adjacent Approaches:

In addition to bioprinting approaches, there are a number of tracheal construction strategies that rely on 3D printed plastic scaffolds that could be translated to bioprinting and whose results are applicable to the future expansion of bioprinting. The following section will briefly discuss these approaches and their relevance to bioprinting.

1.3.1: 3D Printed Bellows Tracheal Scaffold:

Aiming to mimic the strength and flexibility of the trachea, Park et al. designed a bellows style graft.[36] This design was based on native rabbit trachea, 5 mm in diameter with 1.5 mm convolutions every 3 mm along the graft. Using finite element modeling, they compared their bellows style geometry to a regular hollow cylinder. The bellows demonstrated increased resistance to compression while maintaining flexibility. This graft was produced by casting a blend of polycaprolactone (PCL) and gelatin in a 3D printed sacrificial mold. To promote the formation of cartilage, rings of heparinized gelatin sponges loaded with recombinant human transforming growth factor beta 1 (TGF-β1) were seeded with human nasal chondrocytes and manually placed around the graft. A schematic of this process is shown in **Figure 1-1C**. These grafts were implanted in a nude mouse model. After 8 weeks they observed sulfated glycosaminoglycan production in the gelatin sponges, similar to native cartilage. Experimental mechanics data supported their computer modeling. Radial compression data of the explant were also like the native trachea. Using a 3-point bend test, the explant and native trachea had a similar stiffness at low strain, but the native trachea became stiffer than the explant after 2 mm of displacement. While this approach uses traditional plastic printing to create a mold for tissue casting, the same graft design could be printed using a multi-head extrusion bioprinter, allowing the fabrication of branching structures. Innovations such as the “bellows” design highlight the potential of using novel geometries to satisfy the tissue function without attempting to fully recapitulate the native organ. Although, this approach has definite strengths, this kind of graft might face functional challenges long-term. As the PCL/gelatin scaffold degrades it would likely be replaced by scar tissue. The collagen dense tissue may surround and secure the cartilage rings, but it will likely be less flexible than native tissue. Following that approach for smaller airways, without cartilage tissue, the resulting fibrotic airway may be too stiff and present other challenges. One future approach to address this would be potentially seeding the bellows graft with pulmonary fibroblasts or another ECM-secreting cell type that could produce a wider range of matrix proteins, such as elastin, in addition to the chondrocytes.

This same geometry was also used to examine epithelium growth for the tracheal lumen. In this approach, the graft was made from PCL alone, but lined with epithelium derived from human turbinate stromal cells (hTMSCs) harvested from the nasal cavity of patients undergoing septoplasties and partial turbinectomies.[37] The hTMSCs were grown as sheets on temperature-responsive dishes. These sheets were removed from the culture dish and attached to the graft lumen using a thin layer of atelocollagen, a soluble form of collagen primarily used in the cosmetic industry. These tissue grafts, 5 mm wide by 15 mm long, were then implanted in the anterior tracheal wall of a New Zealand white rabbit model. After four weeks, grafts coated with hTMSC sheets exhibited mature columnar epithelium while grafts with atelocollagen alone showed a more immature epithelium lacking mature cilia. From the staining data presented in the paper, it is unclear if the hTMSCs became part of the columnar epithelium or simply helped accelerate native cell migration and maturation. This could be further examined using fluorescence or gene-marked cells. Using this approach in a larger defect area or in the lower airways would be of interest for further investigation.

1.3.2: 3D Printed Polymer Tracheal Scaffolds:

Building on the use of autologous cartilage grafting during laryngotracheal reconstruction, Goldstein et al. designed a 3D printed patch from polylactic acid and type 1 collagen (**Figure 1-1D**).[38] This patch was designed to be sutured directly into the wall of the trachea, providing additional tissue to expand the airway. The oblong patch scaffold, 8 x 3 x 1.2 mm, was printed out of polylactic acid (PLA) with multiple channels. Rabbit chondrocytes were harvested from a donor trachea, combined with the collagen solution and injected into the printed scaffold. The completed patches were then implanted into the anterior trachea of a New Zealand white rabbit model and sacrificed at 4, 8, at 12 weeks. After 12 weeks, histological analysis showed aggrecan production without significant inflammation or granulation. In translating this approach to clinical use, the authors suggest using auricular cartilage, but it may also be worthwhile to explore using mesenchymal stromal cells (MSCs)-derived chondrocytes or another donor source site. Building on this approach, more complex 3D printed synthetic scaffolds could combine multiple cell types.

While still relying on 3D printed PCL rings for mechanical strength, Rehmani et al. combined these rings with decellularized dermal tissue (**Figure 1-1E**).[39] Basing their graft on CT scans, they were able to produce personalized rings within 72 hours after the scan. These rings were then sutured to a hydrated sheet of decellularized bovine dermal collagen matrix. These grafts were implanted in a porcine model, replacing the front half the cervical trachea. The graft was monitored for three months using bronchoscopy before animals were euthanized for histological evaluation. Five of the 7 animals survived to the end point, but all of the animals exhibited granulation at the graft interface. The authors surmised this was an effect of the ECM being rapidly resorbed by the host's cells, eliciting an immune response. They suggested seeding the bovine ECM with autologous MSCs and epithelium, relying on MSC immunomodulatory properties, and the epithelium as a barrier to pathogens. One potential challenge to this approach is its long-term stability. Over time, the PCL will degrade through hydrolysis and, without it, the bovine ECM tissue will likely collapse. To prevent this, MSC seeding could be combined with growth factor delivery to promote localized cartilage differentiation. Townsend et al. also used a ring-supported mesh technique using 3D printed PCL rings embedded in an electrospun PCL patch (**Figure 1-1F**).[40] To create this graft, they spun a base layer of isotropic PCL nanofibers on a mandrel matching the size of their target airway. The PCL rings were added to the mandrel and the spinning continued until the target thickness was reached. The PCL mesh was trimmed to be slightly larger than the tracheal defect in their animal model; a 1.5 x 2.5 cm elliptical opening on the anterior side of Rambouillet-Columbia sheep. The PCL rings extended past the defect site and were sutured into the surrounding tracheal wall. Trachea were retrieved 10 weeks after implantation due to respiratory concerns. Tissue had grown over the luminal side of the graft causing stenosis. While native epithelium grew in from the edges of the construct, it did not reach the center region. Overall, the 3D printed and electrospun PCL graft was able to create a liquid/air barrier in the ovine model. This approach has great potential as an off-the-shelf treatment for emergency surgery. However, since it has no cellular components, the long-term healing process will likely result in scar tissue formation in the defect leading to a weaker region in the tracheal wall. Therefore, the lifetime of the graft is limited by degradation of the PCL unless the graft can recruit surrounding cells.

This could be attempted by including factors into the acellular scaffold or 3D printing biologically active matrix components.

1.4: Figures

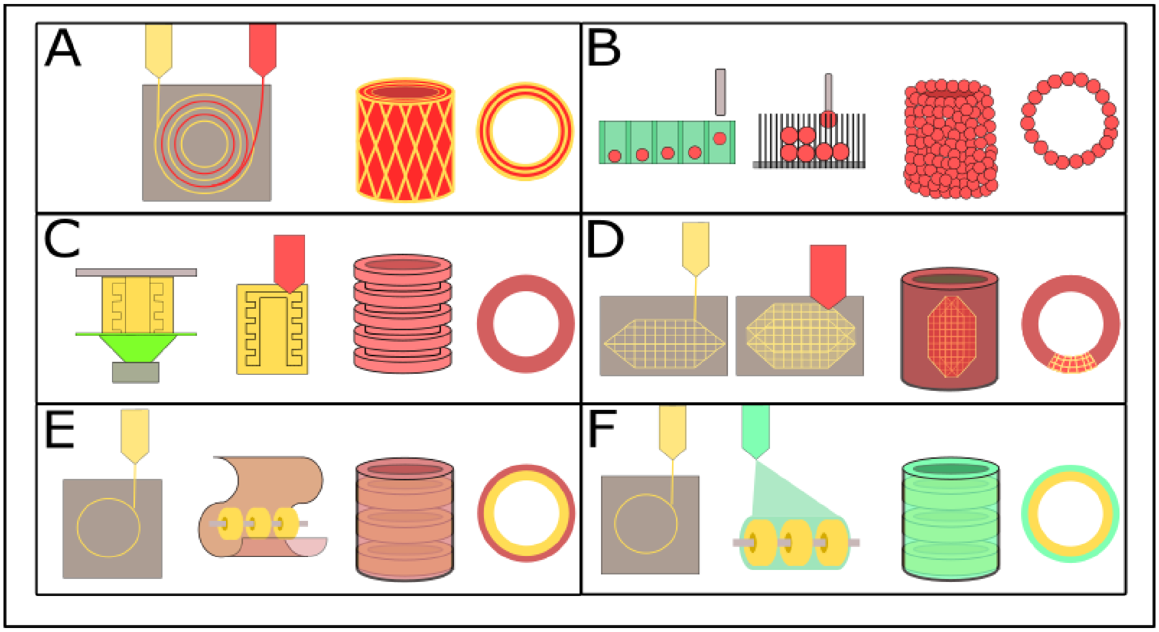

Figure 1-1: Schematic summary of tracheal fabrication methods

(A) Dual Head Extrusion Printing; multiple printing heads are used to print a construct of multiple materials with distinct regions. (B) Organoid Printing; spherical organoids are grown in a well plate, then assembled in a needle array and fused into a solid construct. (C) Bellows Graft; a mold is made using stereolithography, then the hydrogel mixture is injected and solidifies in the mold. (D) Tracheal Patch; a PCL scaffold is printed, then flooded with a cell laden hydrogel. (E) Decelled ECM supported with 3D printed PCL rings; rings are printed out of PCL and sheets of decellularized tissue are wrapped around them. (F) Electrospun PCL supported by 3D printed PCL rings; rings are printed out of PCL and then PCL is electrospun around them.

Chapter 2 Tracheal Cartilage Extracellular Matrix Isolation and Decellularization

The material in this Chapter is adapted from:

Galliger Z., Panoskaltsis-Mortari A. (2017) Tracheal Cartilage Isolation and Decellularization. In: Turksen K. (eds) Decellularized Scaffolds and Organogenesis. Methods in Molecular Biology, vol 1577. Humana Press, New York, NY. https://doi-org.ezp1.lib.umn.edu/10.1007/7651_2017_52[41]

2.1: Introduction

Decellularized tissues have gained significant popularity as scaffolds for tissue engineering, especially for tracheal regeneration.[2] Since these scaffolds are derived from native tissues, they may retain their microscopic structure and the extracellular matrix (ECM), allowing them to better recapitulate the microenvironment of living tissue when compared to synthetic materials alone.[42] One of the most attractive features of decellularized scaffolds is their minimal antigenic potential, thereby increasing the versatility of allografts and xenografts.[43]

Previously our lab has developed a method for whole organ level decellularization.[44] However, not every application requires a whole decellularized organ. There are many cases where isolated tissue-specific ECM is beneficial, such as bioprinting, chemical modification of ECM proteins, and stem cell differentiation.[45,46] The following protocol illustrates a method to isolate and decellularize tracheal cartilage ECM and prepare it for hydrogel incorporation, using porcine trachea and gelatin methacrylate as an example.

2.2: Materials & Methods

2.2.1: Tissue Isolation

After obtaining the trachea, rinse with deionized water to removed non-adhered cells and blood (**Figure 2-1A**). Using tweezers and scissors, remove the connective tissue surrounding the exterior of the trachea by pulling and snipping the outer layers (**Figure 2-1 B&C**). Open the trachea by making a full-length incision on the dorsal side (**Figure 2-1D**). Remove the epithelial layers and smooth muscle by inserting the tip of the tweezers under the superficial layer and sliding it along the full length of the trachea (**Figure 2-1E**). 5. Separate each cartilage ring by cutting them apart (**Figure 2-1F**). Cut each ring into 5-10mm sections and place in deionized water (**Figure 2-1 G & H**).

2.2.2: Decellularization

Combine the tissue with 100 ml of deionized water in a beaker. Allow tissue to soak for an hour while stirring **(Figure 2-2 A & B**). The decellularization process is best done at 4˚C to prevent the growth of bacteria during the initial wash, however room temperature also works. Make sure the entire tissue sample is immersed in fluid and moving to ensure proper mixing during the decellularization process.

Drain deionized water from tissue and add 100 ml triton X-100 (0.1% v/v). Cover the beaker and allow to spin for 18 hours **(Figure 2-2 C & D**). Replace the triton solution with 100 ml of the sodium deoxycholate solution (2% w/v) and allow it to spin for another 18 hours (**Figure 2-2 E & F**). Remove the sodium deoxycholate solution and add 100 ml of the Sodium chloride (1 M) and stir for 2 hours (**Figure 2-2 G & H**). Drain the sodium chloride solution and replace it with 100 ml the DNase solution (1 µg/ml porcine pancreatic DNase, 1.3 mM magnesium sulfate, and 2 mM calcium chloride) for another 2 hours (**Figure I & J**). Lastly, the tissue is rinsed with phosphate buffered saline (PBS) to remove any residual detergents. Aliquot the decellularized tissue into a freezer safe container and freeze the tissue overnight at -80˚C. Lyophilize the frozen matrix until the water has been removed.

2.2.3: Tissue Digestion

Using a mill or mortar, grind the dried ECM into a powder. Combine this powdered ECM at 10 mg/ml with digestion solution (pepsin 1 mg/ml in 0.01N hydrochloric acid). Allow solution to stir at room temperature for two days. Neutralize the pH of the solution using sodium hydroxide (0.1 N). Aliquot and freeze the digested ECM solution. Lyophilize the frozen ECM again and grind into a powder. Once the digested ECM is powdered and stored at -80˚C, it can be used for a variety of applications.

2.2.4: Gel Incorporation

2.2.4.1: Acellular Hydrogel Scaffolds

Prepare hydrogel solution in PBS at 50˚C. See note 4. In preparing the gel solution it is generally easiest to first dissolve the LAP, then dissolve the GelMA while heating the solution to 50˚C in a water bath. Combine the powdered ECM with the hydrogel solution at 50 mg/ml. Vortex to dissolve. Add the ECM hydrogel solution to a tissue culture well-plate, size and volume determined by your application. Crosslink the solution by exposing it to 405nm light for 10 seconds.

2.2.4.2: Cell Laden Hydrogel Scaffolds

Prepare hydrogel solution in cell culture media with half the final volume and cool to 37˚C. Combine the powdered ECM with the hydrogel solution at 50 mg/ml. Vortex to dissolve. Harvest cells using preferred lab method and create a cell suspension of half the final volume. See note 5. Concentration of cell suspension and final concentration of cell seeding depends on cell type used and your application. Combine ECM hydrogel solution with cell suspension to reach final fluid volume. Add the cell laden hydrogel solution to a tissue culture well-plate, size and volume determined by your application. Crosslink the solution by exposing it to 405nm for 10 seconds.

2.3: Acknowledgments

We would like to thank Daniel Sorby for his help procuring animal tissue and processing. We would also like to thank the Hormel company (Austin, MN) for their generosity, donating porcine trachea for research.

2.4: Figures:

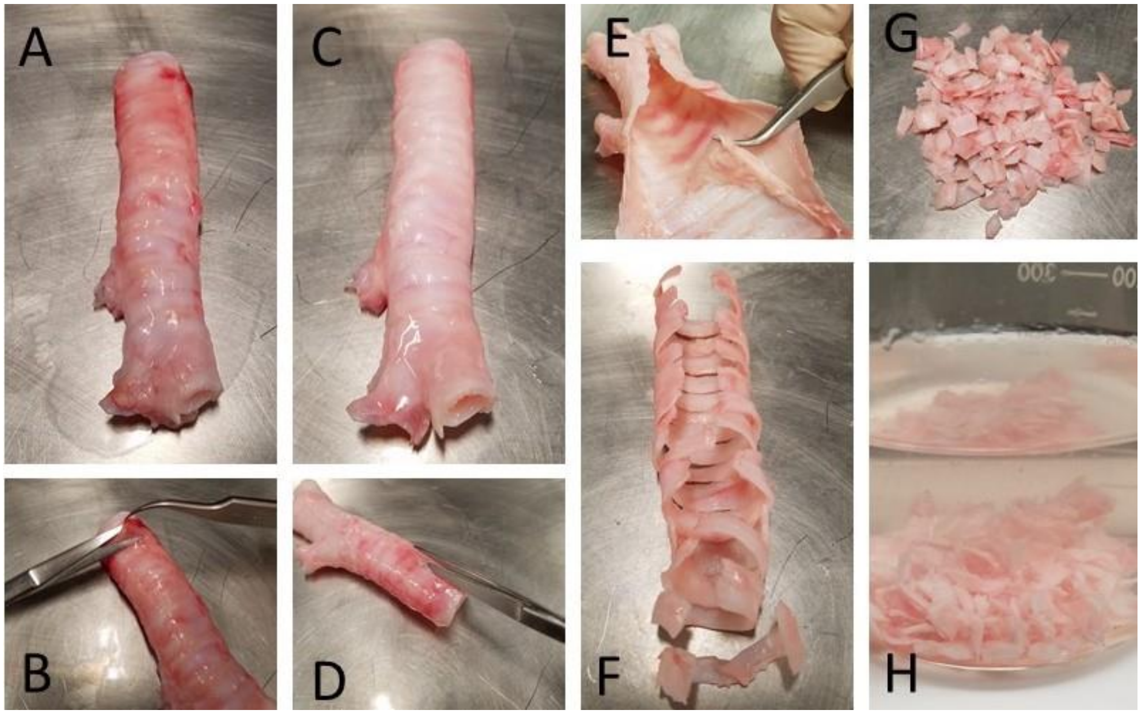

Figure 2-1:Trachea dissection overview.

A) Trachea rinsed with deionized water. B) Removal of exterior tissue. C). Cleaned trachea. D) Cutting along the dorsal side. E) Removing epithelial and muscle layers. F) Separated individual cartilage rings. G) Cartilage sections. F) Cartilage in deionized water.

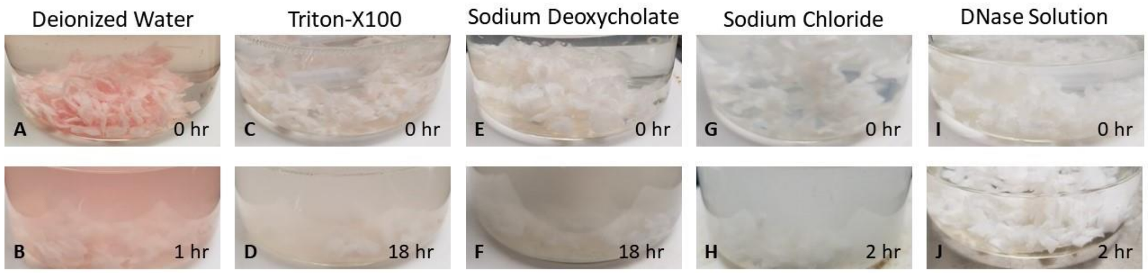

Figure 2-2: Cartilage decellularization overview.

A) Initial tissue in deionized water. B) tissue in deionized water after 1 hour. C) Tissue in Triton-X100 after first wash. D) Tissue in Triton-X100 after 18 hours. E) Tissue in sodium deoxycholate after second wash. F) Tissue in sodium deoxycholate after 18 hours. G) Tissue in sodium chloride after third wash. H) Tissue in sodium chloride after 2 hours. I) Tissue in DNase solution after fourth wash. J) Tissue in DNase solution after 2 hours.

Chapter 3 Photo-crosslinkable tracheal cartilage-derived extracellular matrix hydrogels

3.1: Overview:

Studies of cartilage-derived biomaterials have primarily focused on articular cartilage. However, the same techniques can be translated to tracheal cartilage to create photo-crosslinkable hydrogels. This work compared decellularized extracellular matrix (**ECM**) that was solubilized through pepsin digestion or through urea extraction in gelatin methacrylate (**GelMA**) hydrogels. These soluble fractions were chemically modified with glycidyl methacrylate to allow free radical-mediated crosslinking, producing extracellular matrix methacrylate. Either pepsin- or urea-ECM added to GelMA hydrogels demonstrated chondrogenic properties, however high concentrations of ECM in GelMA hydrogels decreased the mechanical properties. While the chemically modified ECM fractions significantly improved the hydrogel mechanics compared to the unmodified counterparts, bioactive properties were lost.

3.2: Introduction:

The trachea is a vital organ with limited regenerative potential. Critical length defects ranging between 30% of the total length in pediatric patients, to 50% of the total length in adults, require surgical reconstruction and transplanted tissue.[33] While synthetic materials, like silicone, have become common for tracheal grafts, they cannot grow with pediatric patients, leading to multiple surgeries to replace the graft over the patient's lifetime. Pediatric patients need a biologically integratable tracheal tissue that can grow with them over the course of their development while sustaining function. This requires a complex tissue composed of dynamic materials, satisfying the mechanics of native trachea, along with its own progenitor niche for future growth.

3D bioprinting allows the rapid production of patient-specific, tissue engineered constructs. The continued growth and versatility of bioprinting depends on the development of novel printable hydrogels, called bio-inks, that provide mechanical support, cell adhesion sites, and promote the function of the printed tissue. Gelatin methacrylamide (GelMA) and collagen methacrylamide (ColMA) have emerged as common bio-inks because of their tunable mechanical and chemical properties.[47–51] The addition of methacrylamide groups allows these biologically-derived hydrogels to covalently crosslink, significantly increasing their stiffness and stability compared to unmodified proteins. While they provide a printable matrix for cell attachment, they do not fully recapitulate the complexity of native extracellular matrix (ECM).[52,53]

One of the primary functions of the trachea is mechanical, providing a robust patent airway, resisting pressure differences during respiration and compressive forces from trauma.[54] This mechanical stability is provided by the tracheal cartilage, composed of chondrocytes and ECM. Tracheal cartilage ECM is primarily collagen II and aggrecan, similar to many cartilage tissues, but contains more matrilin-1 and epiphycan than articular cartilage.[55] Prior work in the literature has shown that articular and elastic cartilage ECM promotes the differentiation of mesenchymal stromal cells (**MSCs**) to chondrocytes.[56–61] At this time, the specific ECM proteins and signaling pathways that facilitate this differentiation are unknown. However, instructive proteoglycans that compose a small percent of the ECM have been implicated. [62,63]

There are several methods currently used to isolate tissue-specific ECM, across tissue types. The most common method has been enzymatic digestion, generally with pepsin.[64–73] This digestion cleaves the ECM proteins, greatly increasing solubility but may compromise bioactivity. This method selects for larger structural proteins, such as collagens, which can be used to make ECM-based hydrogels through fibrillogenesis.[73]

Unfortunately, this method may not effectively extract the small proteins that may be important for tissue-specific differentiation.[74] Alternatively, urea denaturation has been examined as a less destructive method to extract ECM components. Urea denaturation has been shown to be reversible for several proteins, indicating the ECM harvested with it may better retain its bioactivity once it is returned to homeostatic conditions.[75] However, urea denaturation cannot extract large structural proteins and the resulting ECM does not exhibit fibrillogenesis nor does it spontaneously form hydrogels like its digested counterpart.

Several groups have looked at modifying the ECM of articular cartilage using methacrylate groups to create photo-crosslinkable hydrogels.[46,76] While these two methods have been used separately to harvest different populations of ECM proteins, they have not yet been examined in tandem. We hypothesize that the modification of these ECM proteins will increase their compressive modulus while retaining their chondrogenic properties, and that the urea extracted ECM will exhibit a greater chondrogenic effect than the pepsin digested ECM.

3.3: Materials & Methods:

3.3.1: Decellularization and ECM Isolation

Porcine tracheal cartilage was isolated and decellularized from whole donated trachea as previously published.[41] Whole tracheae were splayed with an incision along the dorsal side, and the luminal tissue was removed. Individual rings were separated from each other and cut into approximately 5mm squares. These squares of tracheal cartilage were washed in 1x phosphate buffered saline. Cellular material was removed with a series of detergent, hypertonic, and enzymatic solutions: 0.1% triton x-100 (18 hours), 2% sodium deoxycholate (18 hours), 1M sodium chloride (2 hours), and 10 ug/ml

DNase in 1.3mM magnesium sulfate and 2mM calcium chloride (2 hours).[44] The decellularized tissue was then frozen, lyophilized, and milled using a Thomas Wiley mill (Thomas Wiley, Swedesboro, NJ). The success of decellularization was evaluated using a picogreen DNA content assay (Invitrogen, Waltham, MA).

Pepsin-digested ECM (P-ECM) was prepared using 1:10 (wt/wt) ratio of porcine pepsin to decelled ECM in 0.1M hydrochloric acid for 48 hours. The digestion was then neutralized with 1M sodium hydroxide and centrifuged at 10,000g for 5 minutes. The soluble fraction was collected from the supernatant, frozen, and lyophilized.

Urea-soluble ECM (U-ECM) was isolated by denaturing the decelled ECM at 100 mg/ml in 3M urea for 72 hours at 8°C. The insoluble fraction was removed by centrifuging at 1,500g for 20 minutes. The supernatant was dialyzed for 48 hours to remove urea at 8°C, then frozen and lyophilized. An overview of this process is shown in **Figure 3-1**.

3.3.2: Chemical Modification

Modified from a method developed for articular cartilage, the ECM (either pepsin-digested or urea-extracted) was dissolved in 1:3 acetone water solution along with triethylamine, tetrabutylammonium bromide, and glycidyl methacrylate.[76] After reacting for 6 days, the resulting extracellular matrix methacrylamide (**EMA**) was precipitated in acetone and dialyzed for two days, then frozen and lyophilized. The methacrylate modification was confirmed using H NMR to detect the methacrylate-associated hydrogen atoms (5-6 ppm), dissolving the EMA in deuterium oxide at 5 mg/ml (**Figure 3-2**). Pepsin-digested-EMA (**P-EMA**) and Urea-extracted-EMA (**U-EMA**) were estimated to be 14±9% and 5±2% modified respectively using the ratio between the methacrylate protons (5.33-6.18 ppm) and methyl protons (1.95 ppm) in the H NMR spectra (n = 4).[77]

Multiple synthesis batches were pooled, used, and analyzed to ensure adequate supply for experiments (5 batches of PEMA, and 3 batches of U-EMA).

3.3.3: 3D Printing-Assisted Casting

3D bioprinting with low viscosity inks requires a support bath and parameter optimization (pressure, speed, etc.) for each bioink. To streamline the production of identical disks from many different bioinks, with varying viscosities, 3D printing-assisted casting was used, opposed to optimizing each individual ink to print using an alternative method like Freeform Reversible Embedding in Suspended Hydrogel (FRESH) printing.[78] Dissolvable molds were 3D printed from 40% (wt/v) Pluronic F-127 using an Inkredible Bioprinter (CellInk, Boston, MA). GCode was generated by a custom Python program. Once printed, the molds were filled with the bioink and crosslinked using 405nm light. The molds were removed with chilled PBS. Cell laden disks were cast using a shallow single walled mold. Tubes were cast between an inner and outer walled mold (**Figure 3-3**).

3.3.4: Mechanical Testing

Uniaxial unconfined compression was performed using the MACH-1 mechanical testing system equipped with a 150g load cell (Biomomentum, Laval, QC, CA). After incubating in PBS for 24 hours, the hydrogel disks were compressed between parallel plates at 20% strain per minute. Compressive modulus was estimated using a linear fit between 10-20% compression. Statistics ANOVA and Tukey HSD were run using R.[79]

3.3.5: Bioactivity

Human bone marrow-derived mesenchymal stromal cells (MSCs) were generated by the University of Minnesota Molecular and Cellular Therapeutics facility (MCT) under GMP protocols through Production Assistance for Cellular Therapies

(PACT) using bone marrow from ALLCELLS (Alameda, California). Quality control analysis was performed on two 30mm wells of a 6-well plate. Cells were treated with colcemid for 3.5 hours, harvested, then analyzed. 20 metaphases were completely analyzed by G-banding at a 400-425 band level resolution. Cells were identified as MSCs by accepted criteria using flow cytometry (**Table 3-1**). They expressed a normal karyotype, with no numerical or structural chromosomal abnormalities. MSCs were combined with bioink and cast into disk molds at $1x10^6$ cells/ml and cultured for 4 weeks in chondrogenesis-permissive media. The permissive media was derived from a chondrogenesis protocol containing High glucose DMEM, L-Proline (40 ug/ml), Dexamethasone (100 nM), Ascorbic Acid (50 ug/ml), Sodium Pyruvate (100 ug/ml), L-Glutamax (10%), ITS-premix (1:1000), PenStrep (100 ug/ml). [80] TGF-β3, that is commonly used to drive chondrogenesis, was removed to evaluate the effect of the ECM and EMA alone.

3.3.6: Histology

Frozen tissue sections, 7um thick, were evaluated using a combination of immunohistochemistry and standard stains. Trichrome staining and hematoxylin & eosin staining were used to compare the engineered cartilage to porcine tracheal cartilage. Safranin-O counter stain with fast green was used to visualize glycosaminoglycan (GAG) content. Chondrogenesis was evaluated by immunostaining for collagen II (ab3092 Abcam Cambridge, UK.) as a maker of mature chondrocytes. Oil red O and alizarin red staining were used to identify adipogenesis and osteogenesis respectively. Relative ECM content was measured using ImageJ, splitting the image into red, green, and blue channels then thresholding the image to determine positive area. Significance between cellular and acellular hydrogels was determined using a T test for each pair. Porcine tracheal tissue, mouse abdominal adipose tissue and femur were obtained from discarded carcasses from unrelated studies (i.e. no approvals required), and used as staining controls.

3.4: Results:

3.4.1: Compressive Mechanics

Hydrogel blend compressive moduli were tested within 1 hour of casting and after incubating for 24 hours in PBS. At either time point, 1% wt/v additions of ECM and EMA did not significantly differ from GelMA (**Figure 3-4A**). However, at 5% wt/v P-ECM, U-ECM, and P-EMA were significantly lower than GelMA initially after casting. After 24 hours, only P-ECM remained significantly lower (**Figure 3-4B**). Compressive moduli of U-EMA samples were slightly lower than GelMA, but this difference was not statistically significant. Likewise, while compressive moduli with EMA conditions were higher than their unmodified counterparts, this improvement was not statistically significant.

3.4.2: Histology

H&E staining showed round cell morphology similar to chondrocytes in all test conditions, however the cell density was much lower than in native tracheal cartilage (**Figure 3-5, A-F**). Trichrome staining indicated collagen rich regions, stained blue, in ECM and EMA conditions but not with the GelMA alone (**Figure 3-5, G-L**). These collagen regions were not directly associated with cells, and were not significantly different that acellular hydrogel conditions, suggesting they are from the ECM and EMA added to the hydrogel rather than produced by the embedded cells (**Figure 3-6**). Safranin-O stains proteoglycans a rich red color, prevalent in the native cartilage (**Figure 3-5, M-R**). The counterstain, Fast Green, identifies fiber proteins. The only condition that contained large proteoglycan areas was the U-EMA condition. However the only condition with a significant difference between cellular and acellular hydrogels was the

U-ECM condition, with the acellular hydrogel exhibiting greater proteoglycan staining. This could be caused by proteoglycans washing out of the U-ECM hydrogel during media changes or cell driven degradation.

MSC chondrogenic differentiation was explored by staining for collagen II. Collagen II was only found associated with cells in the P-ECM and U-ECM conditions (**Figure 3-7,** white arrows). Alizarin red staining did not show any accumulation of calcium in any of the hydrogels, with no significant difference between the cellular and acellular hydrogels (i.e. no osteogenesis) (**Figure 3-8**). However, oil red O staining showed increased lipids in the cellular P-EMA condition which may indicate adipogenesis (**Figures 3-9**). These data suggest chondrogenesis in the ECM conditions, however the significance of these results should be validated using PCR to compare cell differentiation between groups. ECM accumulation could also be further examined using colorimetric assays.

3.5: Discussion:

Incorporating solubilized cartilage-derived ECM appeared to better support chondrogenic differentiation in human MSCs. Unfortunately, this signal appears to become muted during chemical modification to create EMA, either because the addition of MA disrupted signaling moieties. These data suggest these moieties were indirectly degraded during the process, or moieties were lost during dialysis. In other studies, urea-extracted ECM appears to have a greater chondrogenic effect on MSCs than pepsin-digested ECM.[74] In this work, we observed a similar effect with both ECM conditions at 1% wt/v. This discrepancy could be caused by differences in digestion, where at some point the ECM proteins become too denatured to function as signaling moieties. However, the specific ECM components needed to convey a chondrogenic signal are still unknown. They could be further probed in a top down approach by optimizing solubilization techniques and measuring the protein size distribution with gel electrophoresis at various time points. Different protein size populations could be screened to determine if any range, or combination, is required to observe their chondrogenic effect. The active protein populations could be identified using mass spectroscopy.

At the macroscale level, the addition of larger amounts of ECM disrupted the mechanics of GelMA-based hydrogels. This is most likely due to the ECM proteins physically interfering with the ability of GelMA molecules to come in contact with each other and crosslink. While this effect is mitigated with the addition of MA groups to the ECM, this comes at the cost of its chondrogenic signaling. It is of interest to further explore the effect of degree of methacrylation by comparing ECM with varying amounts of MA. Creating a hydrogel of only slightly modified ECM could potentially create a mechanically homogenous hydrogel matching or surpassing the properties of GelMA while maintaining tissue specificity. Further examination is also required to evaluate the effects of methacrylation on cell viability and the hydrogels' ability to support long term culture. The degree of methacrylation may play an important role in controlling the rate of tissue degradation, where greater covalent crosslinking may help maintain tissue integrity while new ECM is produced by embedded cells.

While cartilage engineering is a well-established research topic, it has generated few translated therapies. Since there is a limited supply of autologous chondrocytes, chondrocytes are generally differentiated from bone marrow-derived MSCs. A remaining challenge is maintaining the target chondrocyte phenotype after differentiation. Commonly, MSC-derived chondrocytes stimulated with TFG-β develop hypertrophy and produce endochondral bone-like tissue after several weeks in culture.[81] Other works have shown that the presence of chondroitin sulfate and collagen-XI in the matrix can down-regulate collagen X in MSC-derived chondrocytes in vitro, suggesting it may inhibit hypertrophy.[82,83] This relationship between chondrocyte phenotype and matrix composition warrants further exploration into the long-term outcomes of ECM-mediated MSC differentiation.

3.6: Acknowledgements:

The authors would like to acknowledge the UMN Visible Heart Lab (Dr. Paul Iaizzo) for porcine tissue donation, Darin Sumstad and the UMN Molecular and Cellular Therapeutics facility (MCT) for primary cell isolation and phenotyping, Dr. Bruce Blazar's lab (UMN) for use of mouse carcasses, and the UMN 3D Bioprinting Facility. This work was supported by the National Institutes of Health NHLBI F31 (5F31HL142313) awarded to Z. P. Galliger, a CTSI Translational Research Development Program grant awarded to Z. P. Galliger (from the National Center for Advancing Translational Sciences (grant UL1TR002494. PI: B. Blazar). The content is solely the responsibility of the authors and does not necessarily represent the official views of the National Institutes of Health's National Center for Advancing Translational Sciences. MSCs were obtained using RO1 funding (RO1HL108627, PACT supplement -0452 awarded to APM). The funders had no role in study design, data collection and analysis, decision to publish, or preparation of the manuscript.

3.7: Figures:

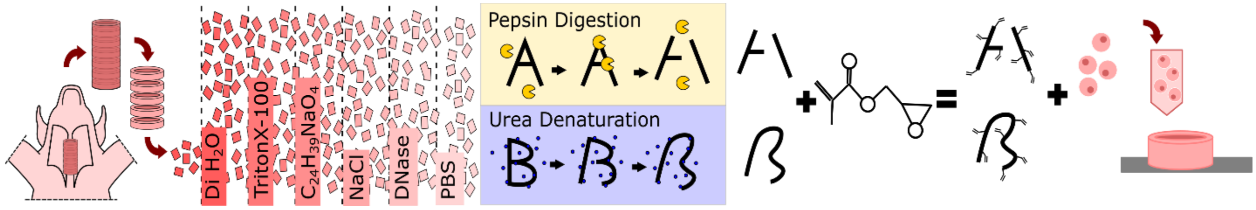

Figure 3-1: Tracheal Cartilage ECM Processing overview

Process overview (left to right). The porcine tracheal cartilage is isolated from surrounding tissue. The tissue is decellularized with deionized water, TritonX-100, sodium deoxycholate, sodium chloride, and DNAse solution then rinsed in PBS. The ECM proteins are then solubilized either with a pepsin digestion (top) or urea denaturation (bottom). These solubilized proteins are then modified with a methacrylate group and combined with cells to bio-fabricate tissue.

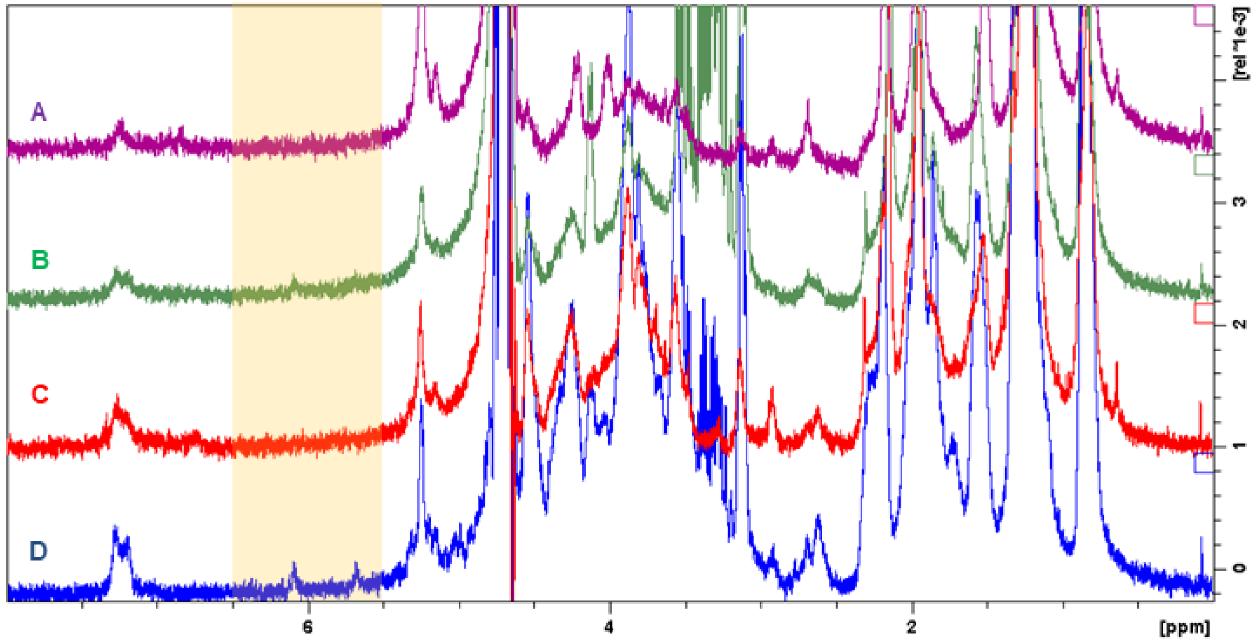

Figure 3-2: NMR spectra results.

Unmodified urea-extracted (U-ECM, A/purple) and pepsin-digested extracellular matrix (P-ECM, C/red) show no peaks between 5.5 and 6.5 ppm (shaded region). Modified urea-extracted extracellular matrix (U-EMA, B/green) has one distinct peak in this region and modified pepsin-digested extracellular matrix (P-EMA, D/blue) shows two distinct peaks indicating the protons associated with the double bonded carbon ($C=CH_2$) in the methacrylate group.

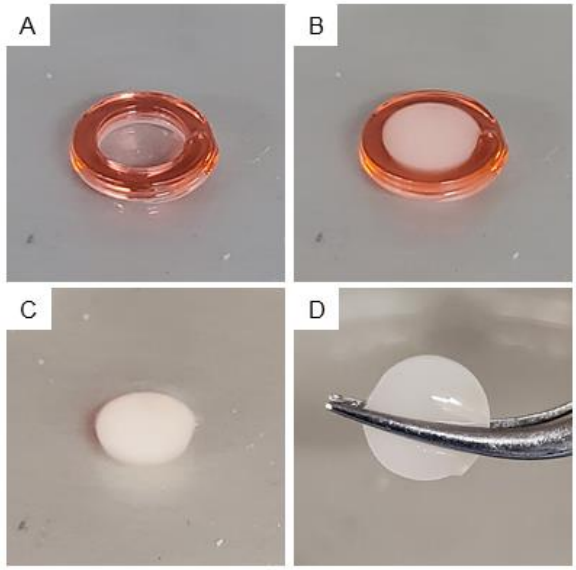

Figure 3-3: 3D Printing-assisted casting.

First a sacrificial mold is printed (A). Next the mold is filled with low viscosity bioink and photo-crosslinked (B). The mold is removed with chilled PBS (C). The final hydrogel can be picked up and manipulated (D).

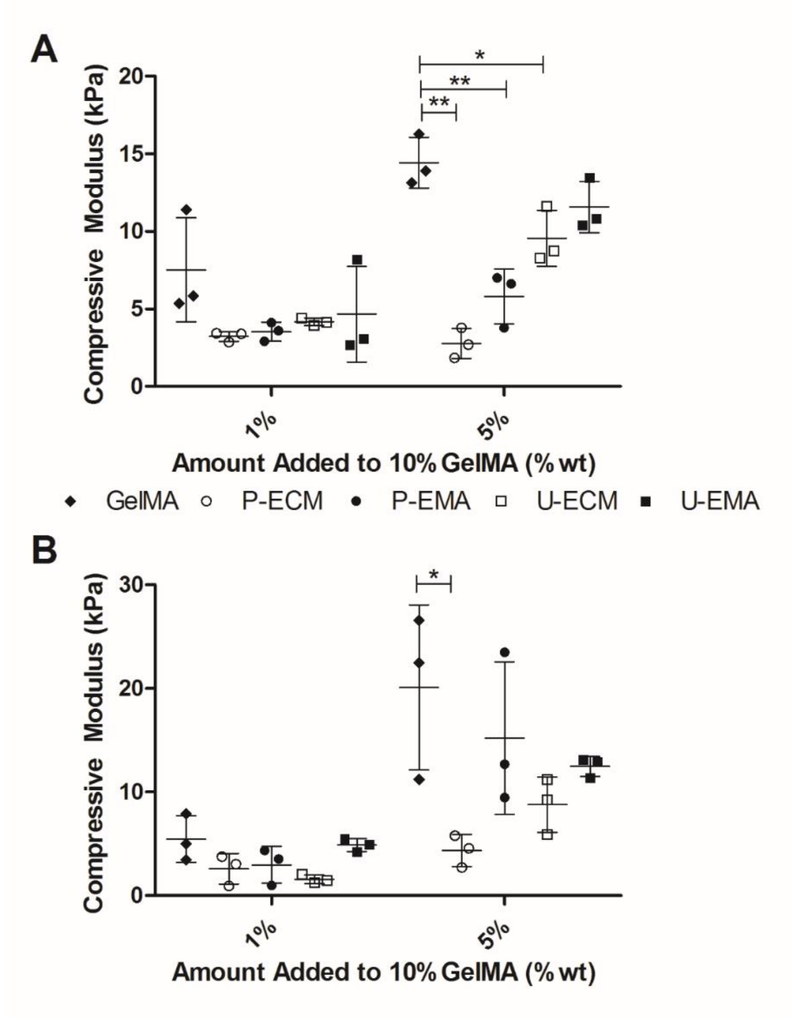

Figure 3-4: Hydrogel Compressive Mechanics

Compressive modulus estimated from 10-20% compression at 20% strain per minute. A) Hydrogels tested within 1 hour of casting. B) Hydrogels tested after incubating for 24 hours. Mean ± StDev Plotted, N = 3; Compared to control at each time point with Tukey HSD; * - P < 0.05, ** - P <0.01

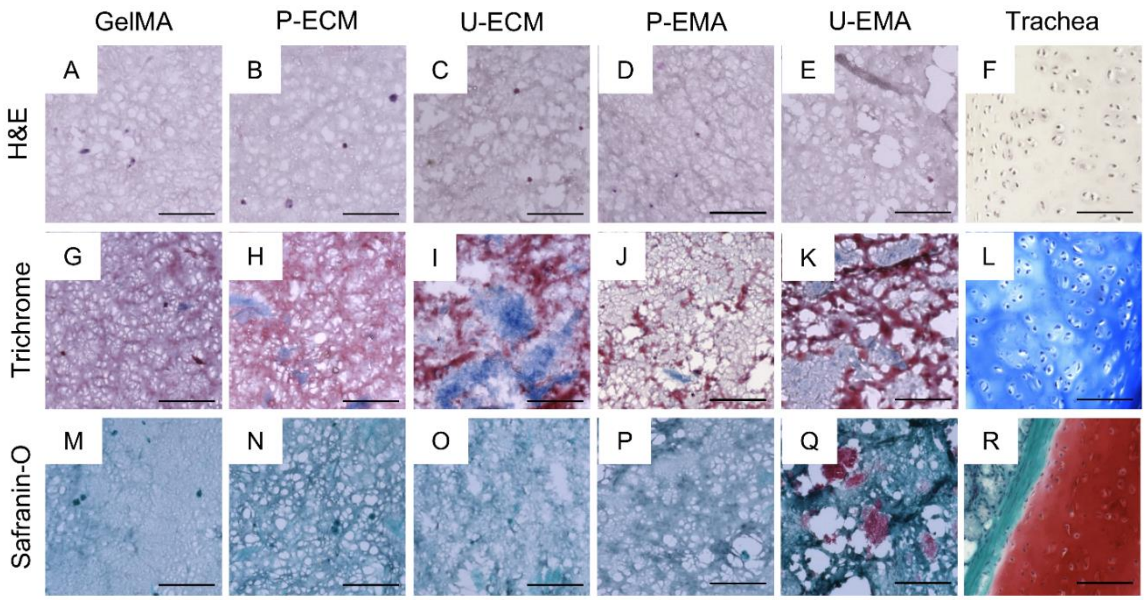

Figure 3-5: Cell-laden hydrogel tissue histology

H&E staining (A-F), Masson's Trichrome staining (G-L), Safranin-O and Fast Green staining (M-R).Hydrogels made from GelMA alone (A,G,M), GelMA with P-ECM (B,H,N), GelMA with U-ECM (C, I, O), GelMA with P-EMA (D, J, P), GelMA with U-EMA (E, K, Q), and porcine trachea as a tissue control (F, L, R). Scale bars = 100 µm.

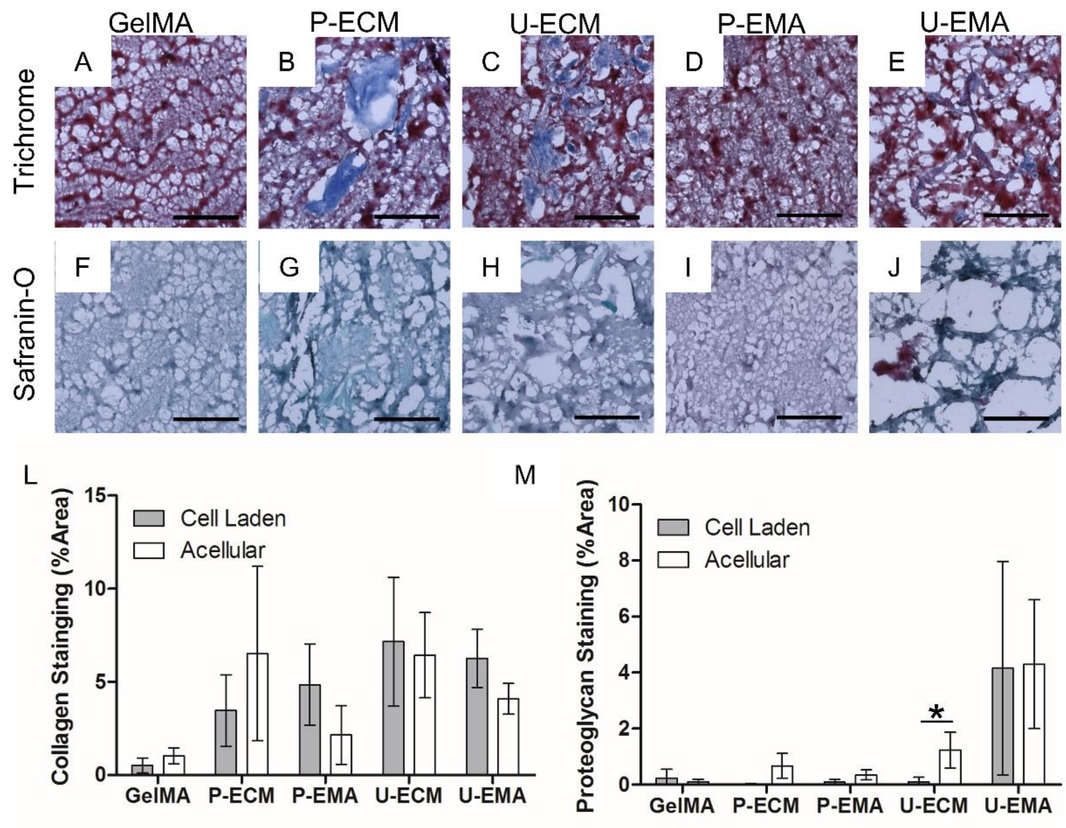

Figure 3-6: Acellular hydrogel histology

Masson's Trichrome staining (A-E), Safranin-O and Fast Green staining (F-J). Hydrogels made from GelMA alone (A & F), GelMA with P-ECM (B & G), GelMA with U-ECM (C & H), GelMA with P-EMA (D & I), and GelMA with U-EMA (E & J). Scale bars = 100 µm. Percent area of fibular collagen from trichrome staining shown in (L) mean ± StDev, n = 3, no $p<0.05$. Percent area of proteoglycans from safranin-O staining shown in (M) mean ± StDev, n = 3, *$p< 0.5$.

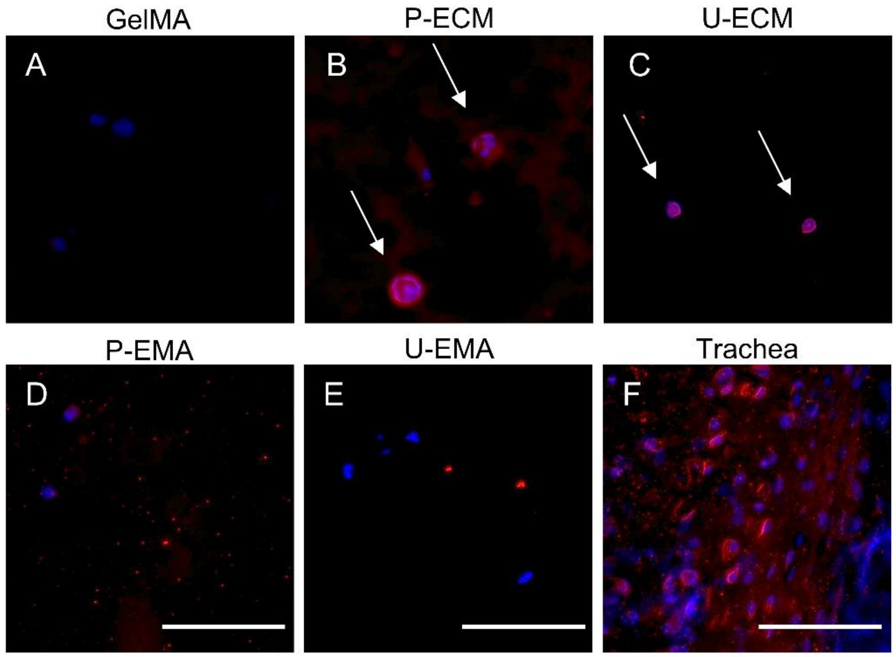

Figure 3-7: Chondrogenesis Immunofluorescent Staining

Immunofluorescence staining for Collagen II (red), nuclei (blue). Hydrogels made from GelMA alone (A), GelMA with P-ECM (B), GelMA with U-ECM (C), GelMA with P-EMA (D), GelMA with U-EMA (E), and porcine trachea as a tissue control (F). Scale bars = 100 µm.

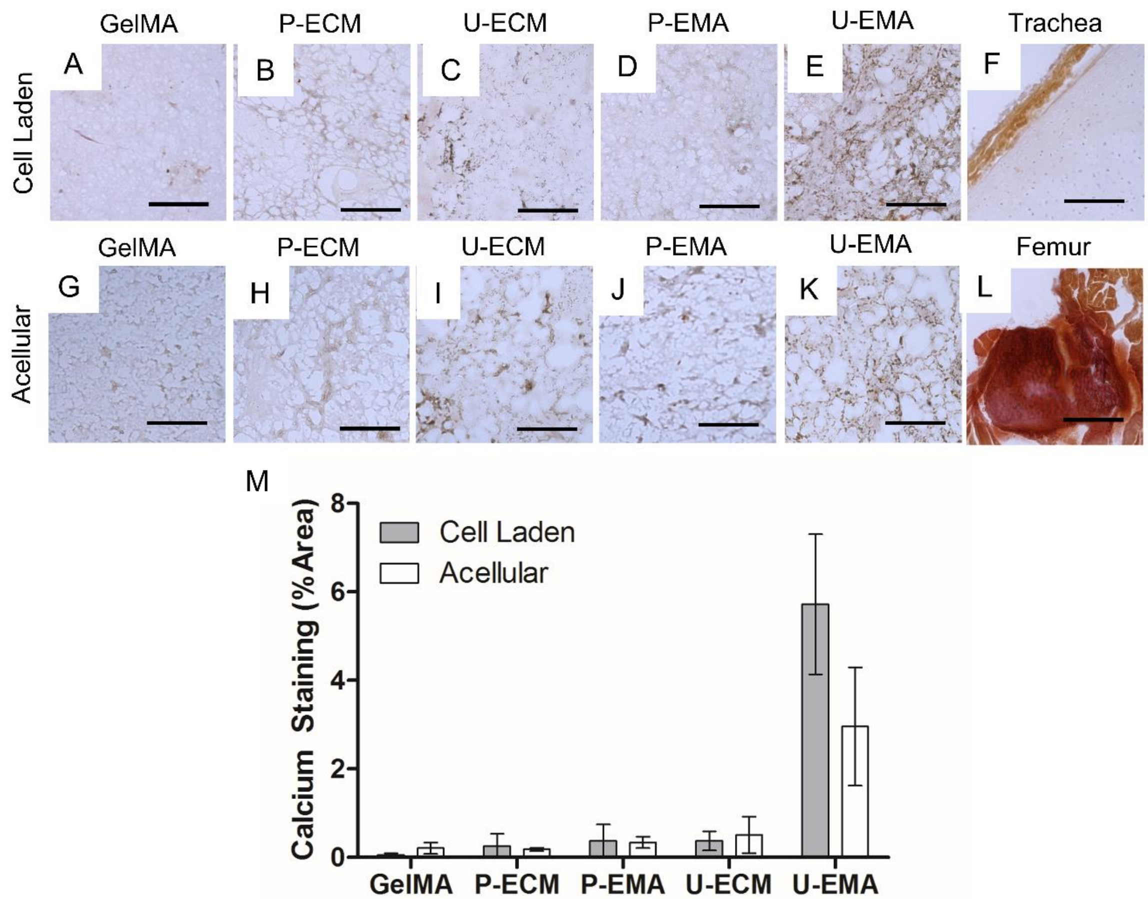

Figure 3-8: Osteogenesis Screening

Cell laden (A-E) and acellular (G-K) hydrogel staining with alizarin red for calicium deposition. Hydrogels made from GelMA alone (A & G), GelMA with P-ECM (B & H), GelMA with U-ECM (C & I), GelMA with P-EMA (D & J), GelMA with U-EMA (E, & K), porcine trachea as a negative tissue control (F), and mouse femur as a positive tissue control (L). The hydrogels exhibit nonspecific light orange staining like the native tracheal tissue, but do not show the dark red staining as seen in the bone control. Percent area of stained tissue is graphed in (M), mean ± StDev, n = 3, no $p<0.05$. Scale bars = 100 µm.

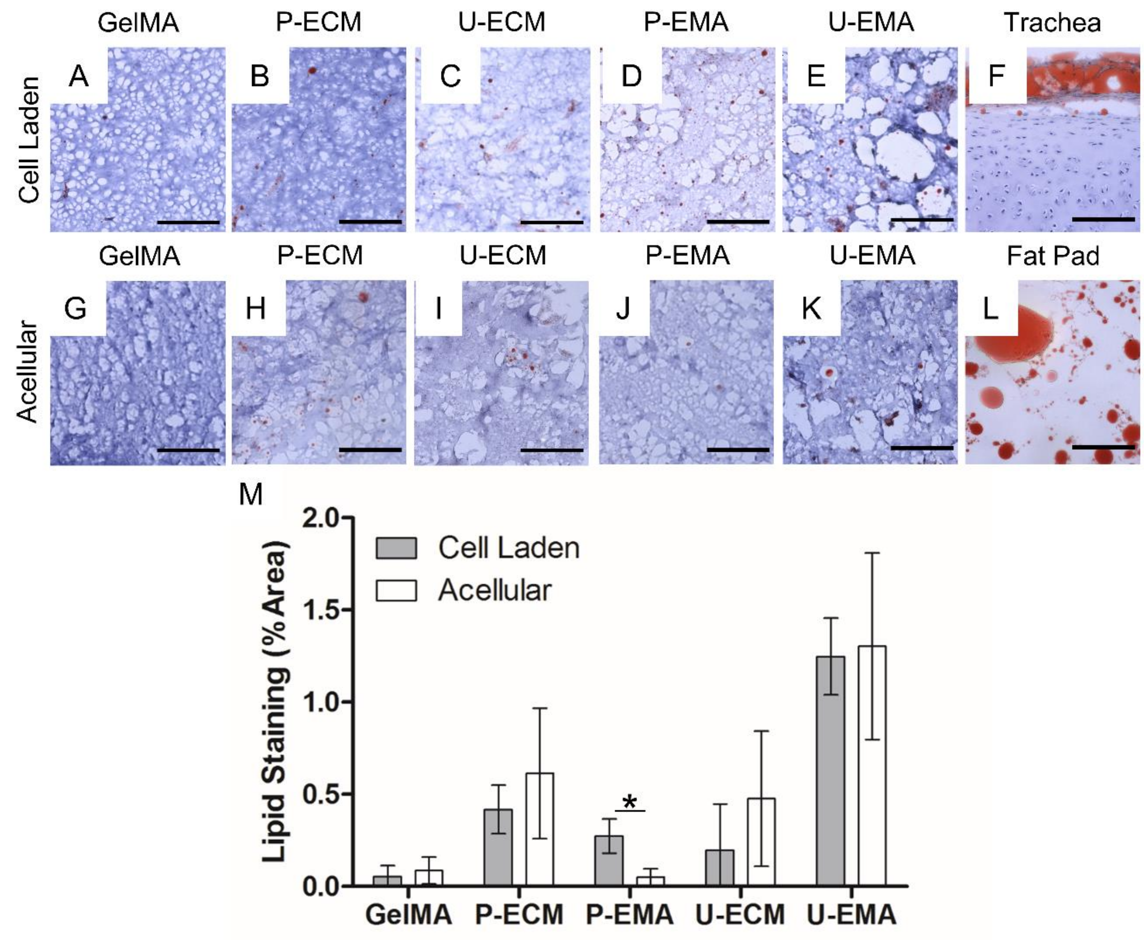

Figure 3-9: Adipogenesis Screening

Cell laden (A-E) and acellular (G-K) hydrogel staining with oil red O for lipid accumulation. Hydrogels made from GelMA alone (A & G), GelMA with P-ECM (B & H), GelMA with U-ECM (C & I), GelMA with P-EMA (D & J), GelMA with U-EMA (E, & K), porcine trachea as a negative tissue control (F), and mouse abdominal adipose as a positive tissue control (L). Percent area of stained tissue is graphed in (M), mean ± StDev, n = 3, *$p<0.05$. Scale bars = 100 µm.

3.8: Tables:

Surface Marker	**CD105**	**CD73**	**CD90**	**CD45**	**CD34**	**CD14**	**CD19**	**HLA-DR**
% positive	*99*	*99*	*99*	*1*	*2*	*1*	*0*	*0*

Table 3-1: Human MSC Phenotyping.

Chapter 4 Extracellular Matrix Microparticles as a Stabilizing Additive for 3D Bioprinting

4.1: Overview:

Current bioinks for 3D bioprinting, such as gelatin methacrylate, are generally low viscosity fluids at room temperature, requiring specialized systems to create complex geometries. Adding decellularized extracellular matrix microparticles derived from porcine tracheal cartilage to gelatin methacrylate creates a yield stress fluid, capable of self-supporting structures. This bioink blend performs similarly at 25°C to gelatin methacrylate alone at 15°C, in print fidelity and tensile mechanics This method lowers barriers to manufacturing complex tissue geometries and removes the need for cooling systems.

4.2: Introduction:

3D bioprinting has the potential for the rapid production of patient-specific, tissue engineered constructs. The continued growth and versatility of bioprinting depends on the development of novel printable hydrogels, called bioinks, that provide mechanical support, cell adhesion sites, and promote the function of the printed tissue.

Gelatin methacrylamide (GelMA) is a commonly used bioink because of its tunable mechanical and chemical properties, relatively low cost, and ability to be remodeled by mammalian cells.[47] GelMA relies on covalently crosslinking methacrylamide side groups, usually via a photoinitiator. These covalent bonds significantly increase its stiffness and stability compared to thermal gelation alone. Other proteins have been similarly modified to create photocrosslinkable hydrogels, such as collagen I to ColMA, or hyaluronic acid to HAMA.[84,85] Unfortunately, most of these materials have a narrow window of use; at room temperature they are unable to support themselves and fail to print complex structures without specialized methods. The field has managed this shortcoming by casting simple geometries, printing at low temperatures, or printing into a sacrificial support bath.[86] While these methods widen the utility of these materials, they face many challenges in scaling the process to clinically relevant manufacturing. Furthermore, these bioinks alone do not fully capture the complexity of native extracellular matrix (ECM), thus limiting their ability to recapitulate native microenvironments.

Whole organ decellularization is the leading approach to capture both the organization and diversity of tissue structure.[44] However, the technique is less effective for dense tissues and requires a donor tissue of a similar size to the target transplant or model. To overcome these limitations, decellularized ECM (dECM) can be processed into tissue-specific bioinks and 3D bioprinted into the required tissue matching the size and geometry required by the patient. This is significantly impactful for pediatric patients with a limited donor pool, for developing *in vitro* models to understand disease states, and to screen potential treatments.

Most commonly, a soluble fraction of dECM is isolated using protein denaturation or enzymatic digestion, then added to a bioink solution to provide tissue specificity or binding sites.[66,87] Other methods modify the dECM with cross-linking groups to incorporate them covalently with the bioink, improving the mechanics of the construct but potentially decreasing the bioactive benefits of the ECM.[46,76] An optimal method that incorporates dECM reproducibly without negatively affecting the tissue mechanics or bioactivity would advance the bioprinting field.

The rheology of complex fluids such as cell-laden bioinks, is dependent on the size distribution of the particles, the interactions between these particles and the solvent, the interactions between the particles themselves, and the mechanics of the particles.[88]

Generally, smaller particles and higher concentrations of particles lead to increased viscosity based on the collective surface area interacting with the bulk fluid.[89] Previous studies have shown that high density cell suspensions exhibit properties of Bingham plastics and have been used as a bioprinting medium.[90] Alternatively, this idea can be used to create a yield stress fluid bioink using high cell density or particle concentration.[91] We hypothesized that the addition of decellularized cartilage tissue particles to GelMA bioinks would widen the temperature range of GelMA 3D extrusion bioprinting, improve print resolution, and improve cell viability.

4.3: Results:

4.3.1: Synthesis and Characterization of GelMA

During GelMA synthesis, methacrylate groups are added to the primary amines of lysine and hydroxylysine in the gelatin.[92] Measuring the concentration of primary amines in GelMA compared to the unmodified gelatin provides an estimate of the degree of modification. The GelMA used in this study was determined to be 94 ± 1% modified (**Figure 4-1A**). The addition of methacrylate groups was confirmed with the emergence of two peaks between 5 and 6 ppm in the H-NMR spectra **(Figure 4-1B**). Using a temperature sweep, the gelation point of 5% wt/v GelMA was determined by modulus crossover to be 15.1 ± 0.1°C **(Figure 4-1C**).

4.3.2: Decellularization and Particle Characterization

To verify the decellularization of the dECM particles, the DNA content was measured using a fluorescence intensity assay. The dECM particles contained 1.2 ± 0.1 nanogram of DNA per milligram of dry tissue, less than 2% percent of native tissue and well below the published decellularization threshold of 50 ng DNA per mg (**Figure 4-**

2A).[85] After cryomilling and filtering, the average particle radius was 29 ± 23 µm, and 75% of all particles were below 50 µm (**Figure 4-2 B & C**).

4.3.3: Dose Dependency of dECM particles on Rheology

To characterize the effect of adding dECM particles to GelMA, a range of concentrations were produced from 0 - 10% wt/v in a 5% wt/v GelMA solution. A parallel plate rheometer was used to characterize the fluid behavior at 25°C. A shear rate flow sweep demonstrated a concentration-dependent effect of the particles on the viscosity of the fluid. The 0% dECM 5% GelMA solution at 25°C was well above its gelation temperature of 15°C and thus behaved as a moderately shear thinning fluid with relatively low viscosity (**Figure 4-3A**). Addition of even 5% dECM significantly changed the behavior, increasing the low-shear viscosity and imparting a more pronounced shear thinning behavior. Increased amounts of particles yielded a predictably higher viscosity and maintained the shear-thinning property.

Oscillatory rheometry was used to characterize the shear stress response to ascending shear rate sweep (**Figure 4-3B**). As expected from the viscosity results, the generated shear stress increased with increasing particle concentrations. The results also indicated a possible change in yield stress at the start of flow, which was further investigated by stress-controlled oscillatory sweeps. Low amplitude oscillations demonstrated a dominant storage modulus (G') consistent with the linear viscoelastic region prior to fluid yield. As the stress increased, the storage modulus decreased, and the loss modulus became dominant. Yield stress was estimated by fitting the data to a Herschel-Bulkley model (95% confidence intervals for the model parameters are listed in **Table 4-1**). This was used rather than estimating the yield stress from the modulus crossover point because some samples either exhibited solid or liquid behavior throughout the stress range (**Figure 4-4**). The particle suspensions showed an increasing apparent yield stress in a concentration-dependent manner (**Figure 4-3C**).

4.3.4: Print Resolution

The resolution of pressure-driven extrusion 3D bioprinting relies on the interplay of many factors. Some factors are a complex result of the rheological properties and the cross-linking rate specific to the bioink formulation and crosslinking mechanism. Others are easily manipulated by changing the printer setup or machine code: tip diameter, printing speed, driving pressure, and stage height.[93] This creates a multi-parameter space, where varying any of the factors will change the print resolution. Blends of 5% wt/v GelMA with 0% to 10% wt/v dECM particles were tested from 25 kPa to 200 kPa using constant print speed (5 mm/s), and stage height (0.1 mm) through 20Ga, 22Ga, and 23Ga x ½" cylindrical tips (**Figure 4-3 D-F**). At 25°C, 5% GelMA was above its gelation point and unstable as a bioink. At 10% wt/v dECM, the linear resolution at 25°C was significantly lower than with 5% GelMA alone printed at 15°C, at pressures below 100kPa for 20Ga tip, 150kPa for 21Ga tip, and 200kPa for 22Ga tip (**Table 4-2**). The 10% dECM, 25°C bioink also exhibited the highest resolution using the 23Ga tip with a line width of 250 ± 40 µm at 75kPa, compared to 5% dECM, 25°C with 470 ± 40 µm and GelMA alone at 15°C with 960 ± 30 µm.

4.3.5: Print Fidelity and Reproducibility

Beyond linear resolution, the bioink must be able to reproduce a 3D model with minimal deformation. With unstable bioinks, as layers are added they can collapse and flow rather than discretely stacking, potentially losing key features of the intended geometry. The effects of the dECM were evaluated by comparing the fidelity and reproducibility of dECM laden constructs to GelMA alone using the same g-code for a hollow tube 5 layers tall. Both reliably produced hollow cylindrical constructs (**Figure 4-5A-B**). The width of the wall of the dECM laden wall was significantly thinner than the GelMA alone (**Figure 2C**), 540 ± 20 μm and 800 ± 10 μm respectively, leading to a significant difference in lumen area (**Figure 4-5 D**). Construct height and circularity exhibited minimal differences (**Figure 4-5 E & F**). The ring constructs were further compared using tensile testing (**Figure 4-5 F**). The stress at failure remained similar for the GelMA with or without ECM, but the strain at failure significantly decreased from 74±2% to 51±1%. (**Figure 4-5 G & H**).

To further explore the dECM bioink, more complex geometries like the carina and larynx were printed. A pediatric scale carina model was designed and printed using 10% dECM, 5% GelMA, 1% LAP and compared with just 5% GelMA and 1% LAP (**Figure 4-6 A-F**). While the dECM laden bioink was able to print easily at 25°C, the GelMA bioink by itself required a chilled syringe (15°C), chilled build plate (10°C), and continuous crosslinking. If the syringe warmed above 15°C, the GelMA bioink would become fully liquid and unprintable. Similarly, if the build plate were at room temperature the bioink would melt and pool before being able to crosslink. Further, if the construct were not continuously crosslinked, layers between the build plate and syringe would warm from contact with surrounding air and melt. Once these bioprinted constructs were completed, to measure their fidelity, a 3D surface was reconstructed from micro CT imaging and compared to the initial carina model (**Figure 4-6 A-F**). From visual inspection, the dECM better exhibits the model’s height and branch angle compared to the GelMA alone. The distances between the carina model and reconstructed surface were calculated and plotted as a heat map (**Figure 4-6 G&H**). The average distance for dECM bioink was 0.5 ± 0.4 mm, with 97% of the bioprinted construct was within 1.5 mm of the initial model.

While average distance for the GelMA alone was 0.5 ± 0.5 mm, with 93% of the construct within 1.5 mm of the initial model (**Figure 4-6 I**).

The bioprinted larynx construct reached 21 mm in height, with a top flaring to 12x17 mm over the 8x12 mm diameter base. To measure the fidelity of the bioprinted construct, a 3D surface was reconstructed from micro-CT imaging and compared to the initial larynx model. The distances between the larynx model and reconstructed surface were calculated and plotted as a heat map (**Figure 4-7**). The average distance was 0.9 ± 0.4 mm. 95% of the bioprinted construct was within 1.5 mm of the initial model.

4.3.6: Cell Compatibility

One of the key properties of any bioink is the ability to sustain cell viability. To examine this, human mesenchymal stromal cells (hMSCs) were printed in GelMA with and without dECM particles and examined histologically after three weeks in culture (**Figure 4-8**). Hematoxylin and eosin (H&E) staining shows few intact cells in both conditions after three weeks (**Figure 4-8 A&D**). Masson's trichrome staining indicates far greater areas of fibrillar proteins, primarily associated with the dECM particles (**Figure 4-8 B&E**). Safranin-O staining indicates abundant proteoglycans in the dECM that are not in condition with GelMA alone (**Figure 4-8 C&F**). Overall, there is little indication the embedded cells modified the bioink hydrogel in either condition.

To further assess cell viability in the bioinks, GFP+ prostate cancer cells were chosen for their robustness and availability. Their ATP content was quantified using a luciferase assay as a proxy for viability. Cell laden GelMA and dECM bioinks were prepared and extruded at pressures between 0 and 200 kPa. Cells printed in GelMA alone showed significantly higher ATP levels than cells printed in GelMA with dECM particles, which were below the background signal of the assay (**Figure 4-9A**). To test for potential cytotoxic solutes, GelMA with and without dECM was cast on half of a well plate then cells were seeded on top. After 24 hours, there were no obvious differences between cells growing next to either bioink or on plastic alone (**Figure 4-9 B-D**). Cells seeded on both bioinks were also evaluated. While cells seeded on top of dECM containing hydrogels showed measurable ATP levels, they were still lower than their counterparts growing on GelMA alone (**Figure 4-9 E**). This difference in ATP levels was not statistically significant, indicating similar levels of cell survival on both hydrogels.

4.4: Discussion:

In this study, we demonstrate the stabilizing effect of decellularized ECM particles on GelMA bioprinting. Bioprinting with GelMA alone is a manufacturing challenge because of its sensitivity to temperature perturbations. If the bioink warms above its gel point at any time before the print is completed and crosslinked, it will greatly deform. The entire printing chamber could be cooled below the gel point, but that becomes a logistical challenge for scaling up and maintenance costs. The GelMA print can be continuously crosslinked, but this excessive exposure to intense light puts stress on the embedded cells and will likely decrease post-print viability. Another option would be to only crosslink during layer changes. Depending on the design of the bioprinter, this adds significant time to the printing process; between each layer, the print head and light source need to exchange places twice. Extended printing time negatively impacts attachment-dependent cell types in suspension in the bioink and allows for the GelMA in the tip to warm to room temperature during layer changes, causing greater print variability. Alternatively, we have shown that adding dECM particles to GelMA allows for reliable bioprinting at room temperature, removing these challenges from the manufacturing process. This is likely due to both increases in viscosity and development of significant yield stress, which resist fluid flow and structural deformation after the bioink is printed. This yield stress, coupled with shear thinning behavior, indicates that the bioink may be best modeled as a Herschel-Bulkley type fluid.

Contrary to what was expected low cell viability was seen in the dECM particle laden GelMA bioinks. There could be many potential causes for this low viability that can be further explored. The denser bioink could limit oxygen diffusion through the hydrogel, suffocating the cells inside. The particle laden bioink could be exerting increased stress on the cells during mixing and extrusion, which has shown decrease cell viability.[94,95] Further, the dECM particle could be swelling over time and exerting physical forces or osmotic pressure on the surrounding cells. Cells could also be negatively responding to partially degraded ECM fragments.[96]

In future work, we expect that cells will benefit from the shear thinning nature of the bioink, as such fluids help to decrease the shear stress experienced by the cells during flow in the printing process. Further, the addition of ECM particles may allow for tissue specificity and greater influence over cell behavior which may be clearer with higher cell seeding density. Our understanding of the role of ECM as an instructive substrate is constantly expanding. Using minimally processed ECM may better retain its bioactivity, producing more reliable cellular constructs.

4.5: Materials & Methods:

4.5.1: GelMA Synthesis and Characterization

GelMA was synthesized using a modified published protocol.[92] All materials were purchased from Sigma Aldrich (St. Louis, MO) unless otherwise specified. Porcine gelatin was dissolved at 10% w/v in reaction buffer [1.1 M sodium carbonate and 1.1M sodium bicarbonate in deionized water] at 50°C. 1% v/v Methacrylic anhydride was added dropwise and allowed to react while spinning for 3 hours at 50°C. GelMA was precipitated in acetone, then dialyzed at 50°C for 4 days. The dialyzed GelMA was then aliquoted into 50 ml conical tubes, frozen, and lyophilized. The GelMA was stored at -20°C until used.

Degree of modification was measured using TNBS assay (ThermoFisher, Waltham, MA) and confirmed using H-NMR. GelMA was compared against gelatin at 1mg/ml, and absorbance was measured at 335 nm using a Cytation3 plate reader (BioTek, Winooski, VT). For H-NMR, GelMA and gelatin samples were dissolved in deuterium oxide at 50 mg/ml and measured using Bruker Avance III HD nanobay AX-400 (Bruker, Madison, WI). Data was analyzed using TopSpin software (Bruker, Madison, WI).

4.5.2: Decellularization and Particle Characterization

Porcine tracheae were isolated and decellularized as previously published.[97] Porcine tissues from male Yorkshire pigs discarded from unrelated cardiac studies were provided by the University of Minnesota Visible Heart Lab. Whole tracheae were splayed with an incision along the dorsal side, and the luminal tissue was removed. Individual cartilage rings were separated from each other and cut into approximately 5mm squares.

The tissue was washed in 1x phosphate buffered saline (1xPBS). Cellular material was removed with a series of detergent, hypertonic, and enzymatic solutions: 0.1% triton x-100 (18 hours), 2% sodium deoxycholate (18 hours), 1M sodium chloride (2 hours), and 10 ug/ml DNAse in 1.3mM magnesium sulfate and 2mM calcium chloride (4 hours). The decellularized ECM was then frozen, lyophilized, and milled using a Spex Freezer/Mill 6700 (Spex, Metuchen, NJ). The dECM particles were filtered using a 100-um nylon mesh (LLL & Solutions LLC, Miami, FL).

The success of decellularization was evaluated using the Quant-iT PicoGreen DNA assay (Invitrogen, Waltham, MA) sensitive to 50 pg **(Figure 4-2)**. Particle size was determined by imaging particles dusted in a 6 well plate using the EVOS 2 (ThermoFisher, Waltham, MA). Particle size distributions were calculated using ImageJ.[98]

4.5.3: Bioink Rheological Characterization

The rheological properties of the dECM particles added to GelMA were measured using a TA Instruments DHR-3 with a lower peltier plate and an upper 40mm parallel plate attachment (TA Instruments New Castle, DE). Bulk rheological properties of GelMA-dECM mixtures were measured at 25°C and a gap of 1mm (>10X particle size). These mixtures were 5% wt/v GelMA with 0, 5, or 10% wt/v dECM particles. Samples were conditioned for 120s at the testing temperature (15 or 25°C), then subjected to an oscillatory strain sweep from 0.01-500% at a frequency of 1.0 Hz. This strain-controlled approach allowed for all samples to be tested with the same protocol while avoiding sample ejection at high shear rates. Next, samples were conditioned for 120s at the testing temperature and subjected to an increasing shear rate sweep (range 1x10^-2 to 1x10^2 1/s) to produce a flow curve. The oscillatory test characterized the viscoelastic behavior in terms of storage modulus (G') and loss modulus (G''). This allowed for the calculation of an apparent yield stress, observing the stress value at which the storage and loss moduli cross (tan(Δ) = 1). In cases where a yield stress could not be observed, it was inferred by fitting the flow curve data to the Herschel-Bulkley Model (**Equation 4-1**) using the TRIOS software package (TA Instruments, #4.4.0.41651, New Castle, DE).

$$\tau = \tau_o + k\dot{\gamma}^n \qquad \text{(\textbf{Equation 4-1})}$$

In this model, τ is the shear stress and $\dot{\gamma}$ is the shear rate. The parameters τ_o, k, and n are the yield stress, consistency index, and flow index, respectively. Confidence intervals for the model parameters for each ECM concentration are shown in the supplementary materials (**Table 4-1**).

4.5.4: Print Resolution

To screen the effects of the dECM additive, the 2D extrusion resolution of varying concentrations was tested using cylindrical needles (20,22, and 23 gauge, ½") with constant print speed (5 mm/s), and height (0.1 mm) while the driving pressure was varied from 25 kPa to 200 kPa using a BioX bioprinter (Cellink Boston, MA). All bioinks were 5% wt/v GelMA and 1% wt/v lithium phenyl-2,4,6-trimethylbenzoylphosphinate (LAP) with 0% - 10% wt/v dECM. The subsequent fiber diameters were measured using images obtained with an EVOS 2 fluorescence imaging system (ThermoFisher, Waltham, MA).

4.5.5: Print Fidelity and Reproducibility

To compare the utility of dECM particles as an additive, 5% GelMA with 1% LAP printed at 15°C and 125kPa and 5% GelMA and 1% LAP with 10% dECM printed at 25°C and 75kPa were printed using the same g-code with a 18 Ga tip at 5 mm/s. The g-code was a stack of 5 layers of rings with a 5 mm radius. The first layer height was set at 0.1 mm, and the four subsequent layers at 0.5 mm steps to 2.1 mm total height. After the prints were complete, the bottom layers were imaged using the EVOS 2. The area of the center lumen and the wall were measured using ImageJ. Circularity was calculated for the outer edge of the ring, $C = 4\pi\ \text{Area}/\text{Perimeter}^2$. From this measurement, the uniformity of the ring can be compared. A perfect circle has a value of 1, and the greater the deviations from 1 the more defects are present in the printed construct. The height of these tubes was measured using the surface detection function of the MACH-1 (Biomomentum, Laval, QC, CA). Tensile testing was performed using the

MACH-1 and 5mm T tensile fixtures. Rings were loaded on the tensile testing posts then pulled at 0.5 mm/s until failure. Stress and strain were calculated using established methods.[99,100]

To further explore dECM printability, a more complex geometry was tested. A pediatric scale carina was printed with 5% GelMA and 1% LAP with 10% dECM. The carina was modeled using Solidworks2020 (Solidworks Corp. Waltham, MA). The g-code was generated using Simplify3D (Simplify3D Cincinnati, Ohio) and printed using a BioX bioprinter. The printed construct was imaged using a X-TEK XT H 225 micro CT scanner (METRIS, Leuven, Belgium). CT images were processed with CT Pro 3D (XTEK) and VGSTUDIO Max 3.2, creating DICOM files. The DICOM files were then segmented using 3D Slicer to create and export a 3D mesh.[101] The resulting 3D mesh was compared to the original model using CloudCompare (www.cloudcompare.org).

4.5.6: Cell Culture and Tri-lineage Differentiation

Human bone derived mesenchymal stromal cells (hMSCs) were generated by the University of Minnesota Molecular and Cellular Therapeutics facility (MCT) under GMP protocols from Production Assistance for Cellular Therapies (PACT) using bone marrow from ALLCELLS (Alameda, California). HMSCs were maintained in minimum essential medium-alpha (Alpha-MEM) (ThermoFisher, Waltham, MA) with 10% fetal bovine serum (FBS) (R&D Systems, #S11150), 1% minimal essential medium non-essential amino acids solution (MEM NEAA) (Invitrogen Life Technology, Waltham, MA), 1% penicillin-streptomycin (Invitrogen Life Technology, #15070-063), 10 ug/mL transforming growth factor-beta 3 (TGF-beta) (R&D Systems, #8420-B3/CF), and 500 ug/mL recombinant human epidermal growth factor (EGF) (R&D Systems, Minneapolis, MN). hMSC quality and identity were confirmed using a Human Mesenchymal Stem Cell Functional Identification Kit from R&D Systems (Minneapolis, MN) (**Figure 4-10**).

Human prostate cancer cells (cell line CWR-R1, kindly provided by Dr. Dan Vallera, UMN) were used for further viability experiments. These cells were cultured in Dulbecco's Modified Eagle Medium (DMEM) with 10% FBS and 1% penicillin-streptomycin.

4.5.7: Cell Compatibility

To evaluate cell compatibility hMSCs were printed in GelMA hydrogels with and without dECM particles. Harvested MSCs were suspended in 5% GelMA with 1% LAP in media at $1x10^6$ cells/ml. The cell-laden solution was either cooled to 15°C and printed at 125 kPa for the GelMA alone condition or combined with 10% dECM and printed at 25°C and 75 kPa for the dECM condition with an 18 Ga needle. These cell-laden hydrogels were cross linked using 405 nm light for 10s, then incubated for three weeks in chondrogenic media: Dulbecco's Modified Eagle's Medium (Invitrogen), 40 ug/ml L-Proline, 100 nM dexamethasone, 50 ug/ml L ascorbic acid, 100 ug/ml sodium pyruvate (Invitrogen), 100 ug/ml Pen-Strep (Invitrogen), 1% Glutamax (Invitrogen), ITS+ premix (Corning, Corning, NY), and 10 ng/ml transforming growth factor-beta 3 (R&D Systems). After incubation, samples were fixed in 4% paraformaldehyde, paraffin-embedded, sectioned, and stained.

Prostate cancer cells were similarly harvested and suspended in each bioink at 7x106 cells/ml, brought to target temperature and printed with an 18 Ga needle. For surface seeding experiments, cells were seeded at 5x106 cells/cm2. To measure the ATP concentration, 300 mg of hydrogel were homogenized in PBS then combined with CellTiter-Glo Luminescent Cell Viability assay (Promega, Madison, WI).

4.5.8: Statistical Analysis

Comparisons of means between two groups were performed by Student's T-test, and comparisons between three or more groups were performed using one-way ANOVA and Tukey's Honest Significant Difference test. Comparison of fitted Herschel-Bulkley model parameters was accomplished using confidence intervals corrected for multiple comparisons using the Bonferroni method. Where provided, error bars represent the standard deviation. All statistical tests were performed using JMP 15.1.0. Graphs were created using Prism, JMP 15.1.0 or Microsoft Excel.

4.6: Acknowledgements

I would like to acknowledge the Visible Heart Lab for porcine tissue donation, the UMN Polymer Characterization Facility, the Minnesota Dental Research Center for Biomaterials and Biomechanics, and the UMN 3D Bioprinting Facility. I would like to thank Caleb Vogt for his work collecting and analyzing the rheological data presented in this thesis. I would like to thank Haylie Helms for her work expanding and characterizing the cells used in this work. This work was supported by the National Institutes of Health NHLBI F31 (5F31HL142313) awarded to Z. P. Galliger, a CTSI Translational Research Development Program grant awarded to Z. P. Galliger (from the National Center for Advancing Translational Sciences (grant UL1TR002494. PI: B. Blazar. The content is solely the responsibility of the authors and does not necessarily represent the official views of the National Institutes of Health's National Center for Advancing Translational Sciences.). Cells were obtained using RO1 funding (RO1HL108627, PACT supplement - 0452).

4.7: Figures:

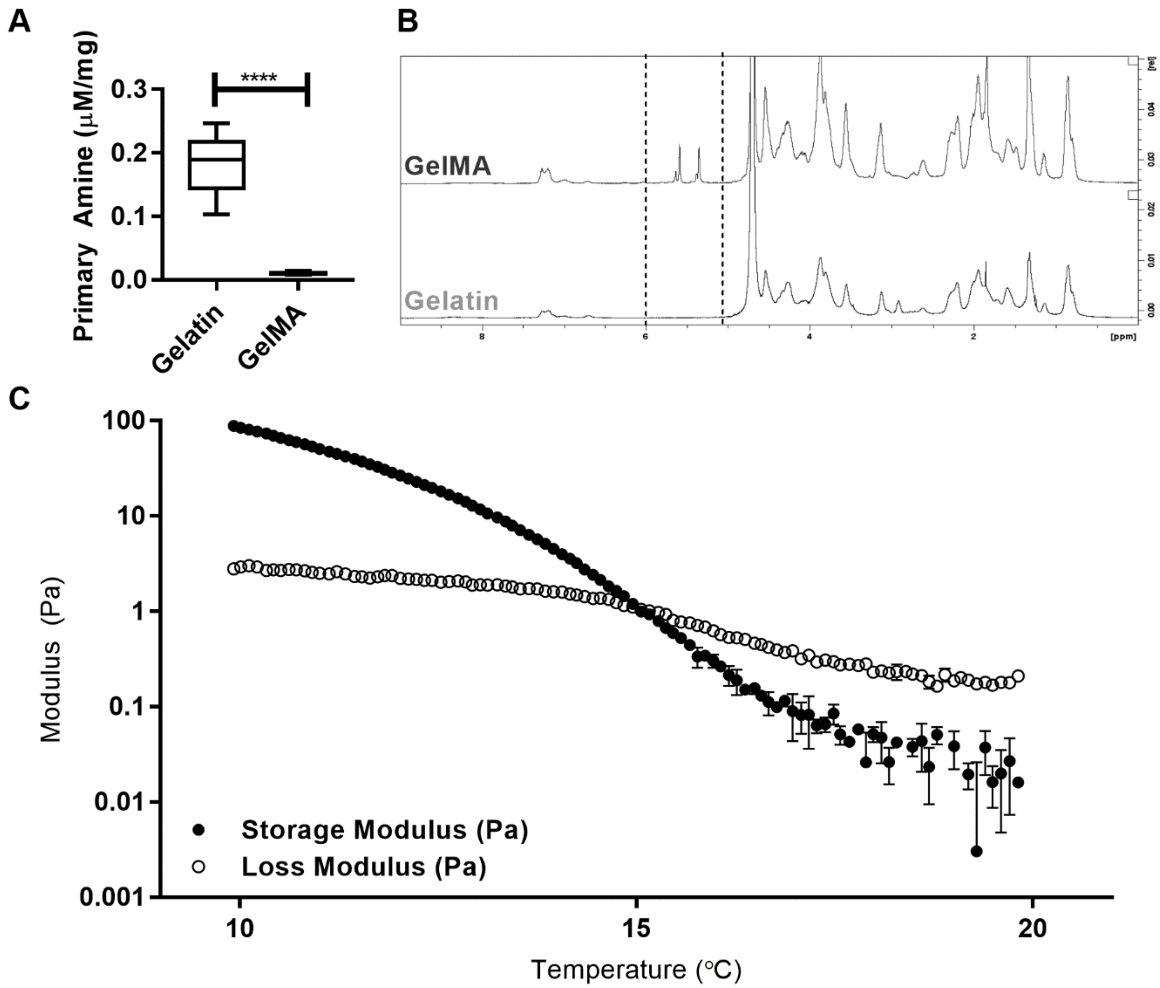

Figure 4-1: GelMA characterization

A) Primary amine concentration per milligram of gelatin or GelMA respectively, n = 3 $p<.001$. B) H-NMR spectra of gelatin and GelMA. C) GelMA Temperature Sweep, n = 3 Mean ± StDev deviation plotted.

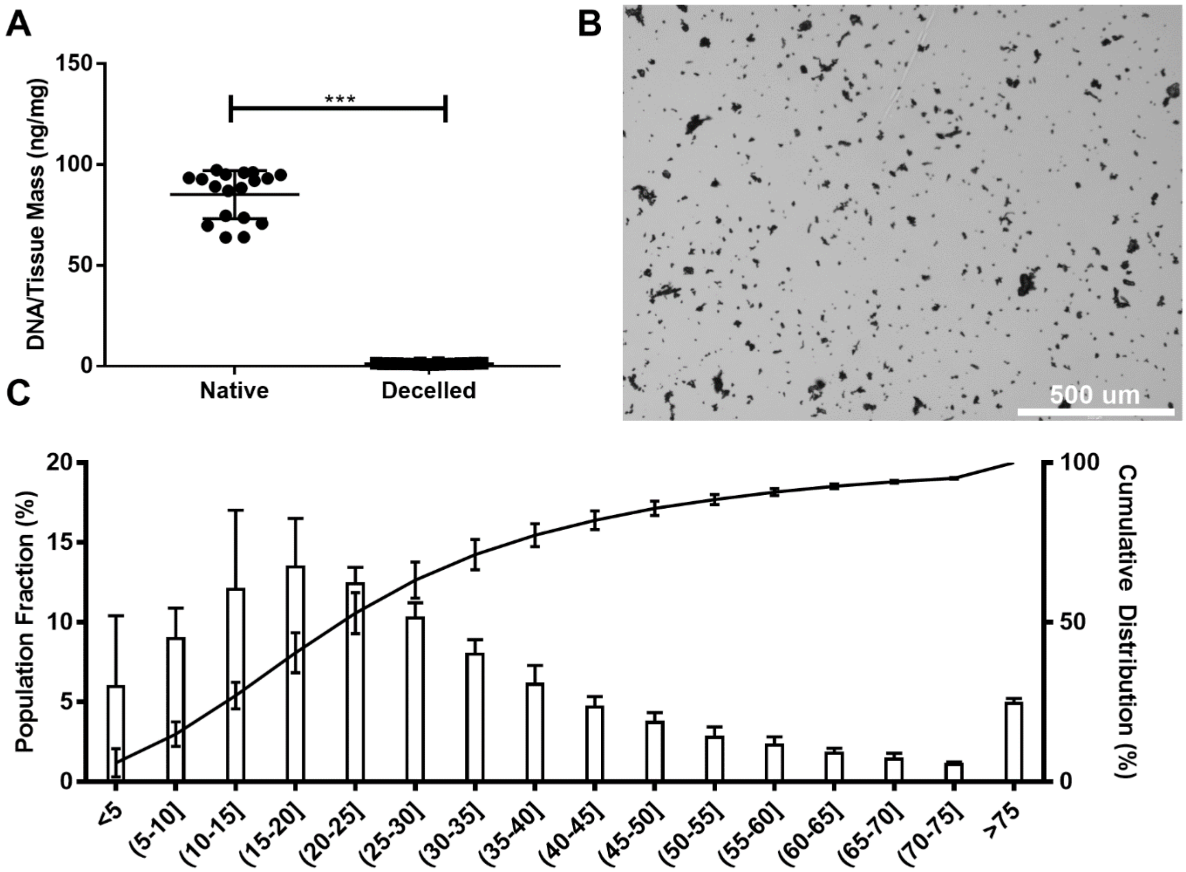

Figure 4-2: dECM Particle Characterization

A) PicoGreen Assay. Mean DNA content per mass of dry tissue, mean ± standard deviation plotted n = 3. B) 4x magnification image of decellularized, cryomilled, and filtered dECM particles, 500 um scalebar. C) Histogram of particle diameters normalized by total number of particles in each condition, mean +/- standard deviation plotted n = 3 (left). Cumulative distribution function of particle population, mean ± standard deviation plotted n = 3 (right).

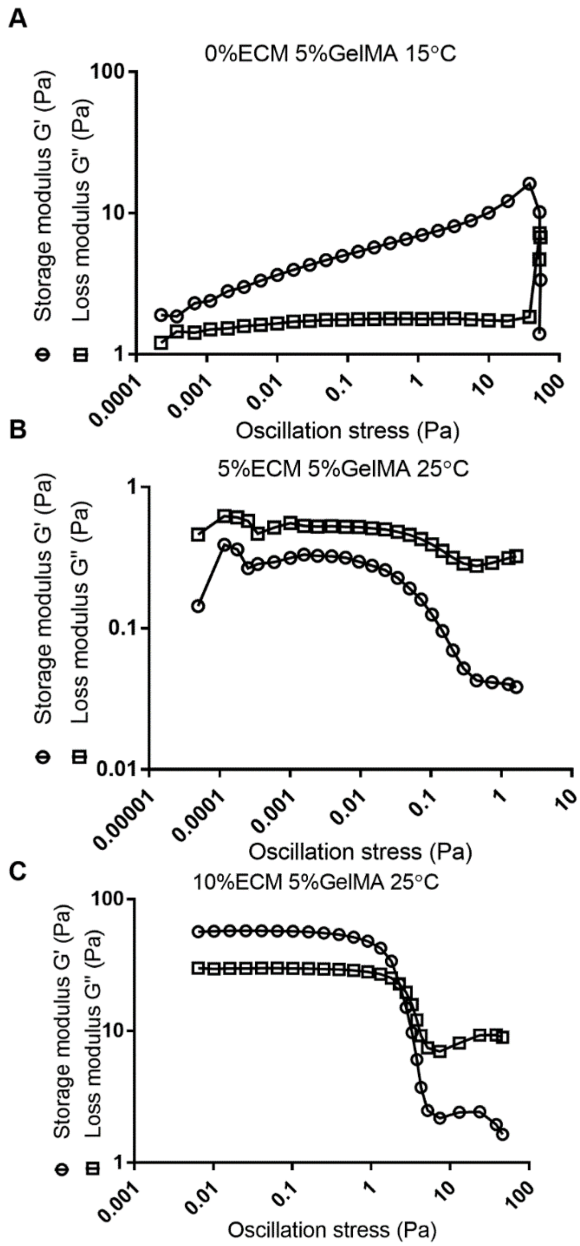

Figure 4-3: Oscillatory stress sweeps

A) 0% ECM with 5% GelMA at 15*C, B) 5% ECM with 5% GelMA at 25*C, and C) 10% ECM with 5% GelMA at 25*C.

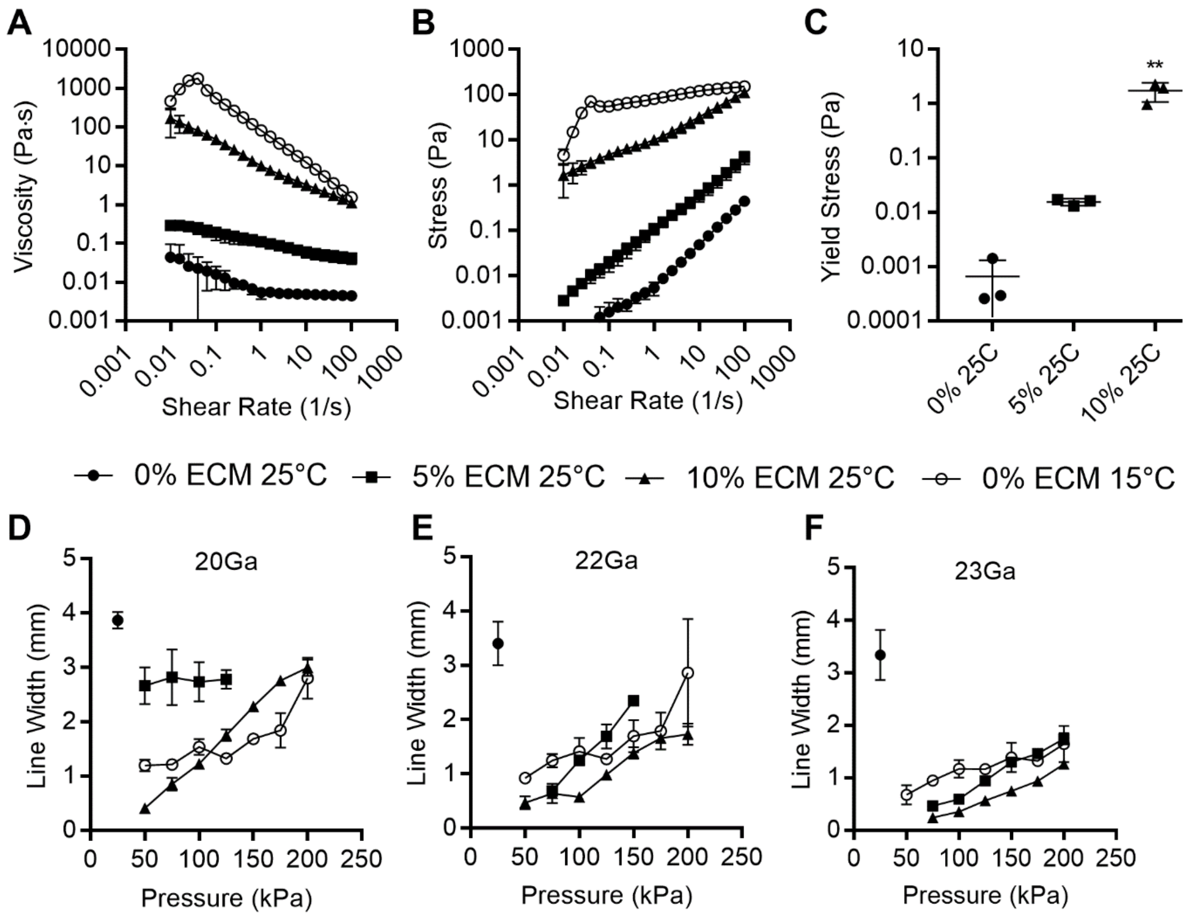

Figure 4-4: dECM dose dependent rheology

10% GelMA with dECM ranging from 0%-20% wt/v: A) Shear rate flow sweep, n = 3. B) Mean thixotropic hysteresis loops. C) Apparent yield stress, n =3, [**p<.01] between groups. D-F) Plot of filament thickness versus pressure for each bioink through 20Ga, 22Ga or 23Ga needles respectively, plotted as mean ± standard deviation n = 3, significance not shown for clarity values shown in **Table 4-2**.

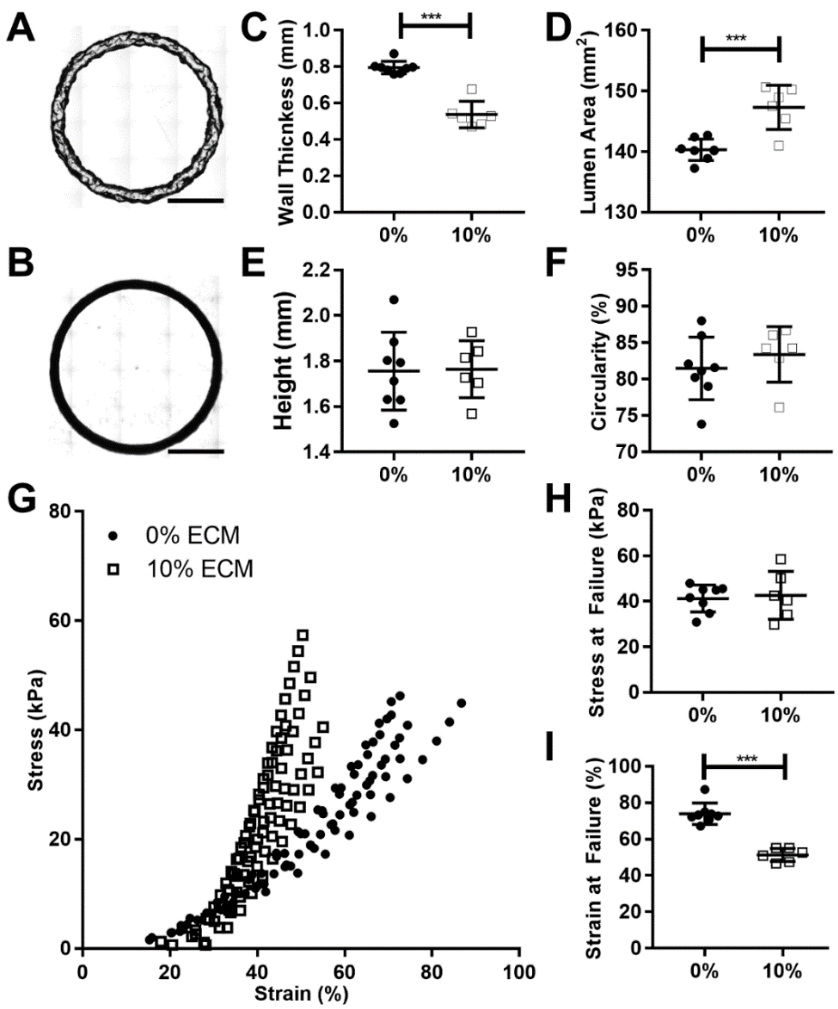

Figure 4-5: Print fidelity and reproducibility of simple geometries

A) Representative image of 5% wt/v GelMA ring printed at 15°C, scale bar 5mm. B) Representative image of 5% wt/v GelMA with 10% wt/v dECM ring printed at 25°C, scale bar 5mm. C) Graph of ring wall thickness (mm). D) Graph of lumen area (mm^2). E) Graph of ring heights (mm). F) Graph of ring outer edge circularity (%). G) Graph of tensile failure, individual runs plotted, 0% at 15°C n= 8, 20% at 25°C n = 6. H) Stress at failure for each construct. I) Strain at failure for each construct. [p<.05 *, p<.01 **, p<.001 ***]

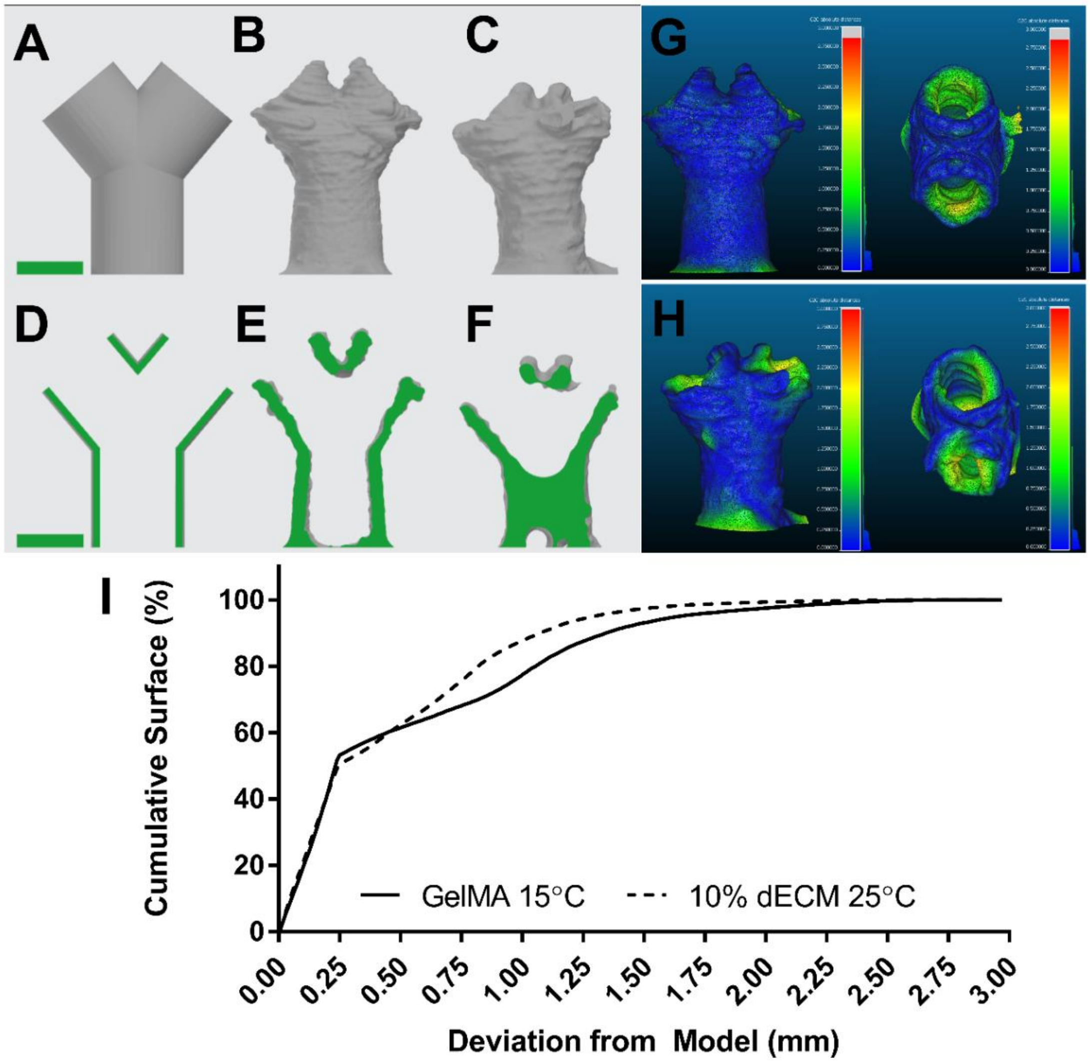

Figure 4-6: Fidelity of self-supporting carina

A&D) Carina model geometry, B&E) 3D reconstruction of dECM printed carina, C&F) reconstruction of GelMA printed carina, full surface scale bars 5mm. G) computed distance between dECM printed carina and model geometry, side (left) and top (right) view.H) computed distance between GelMA printed carina and model geometry, side (left) and top (right). I) Cumulative surface distances between bioprinted constructs and model geometry.

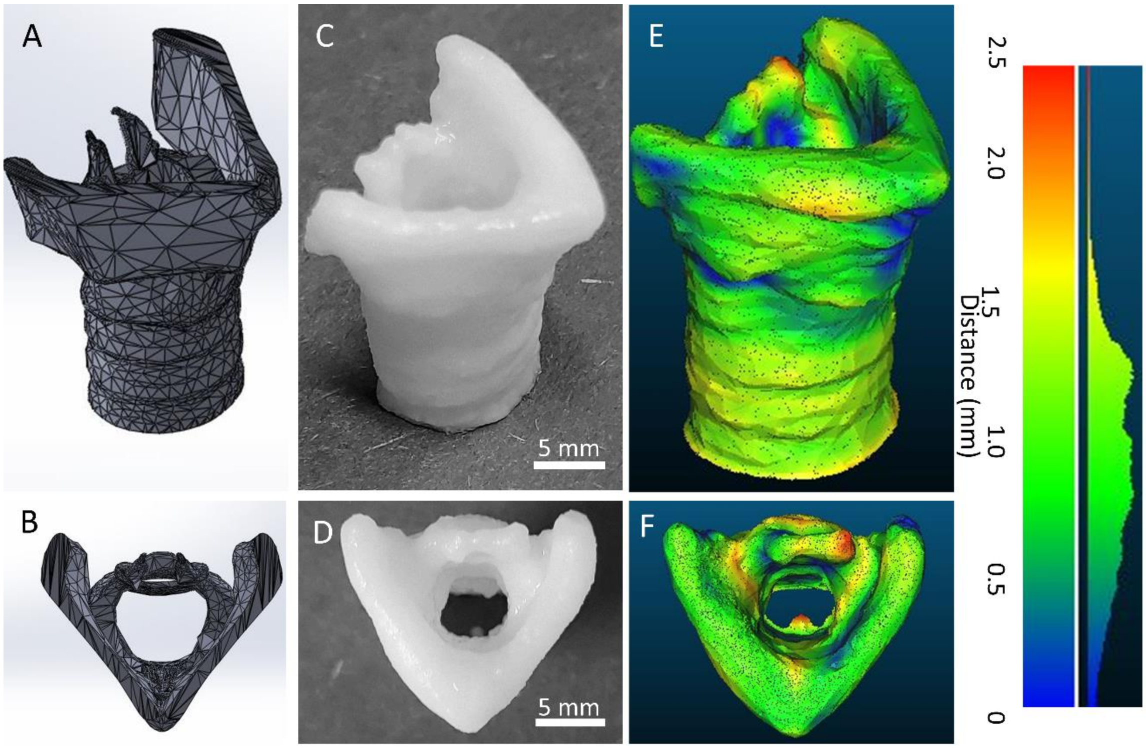

Figure 4-7: Fidelity of self-supporting, ECM bioink larynx

A & B) Larynx digital model geometry, side and top view respectively. C & D) ECM Particle laden bioprinted larynx construct side and top view respectively, 5 mm scale bar. E & F) Surface map of distance between digital model geometry and bioprinted larynx, side and top view respectively. A histogram of the distances is shown on the right.

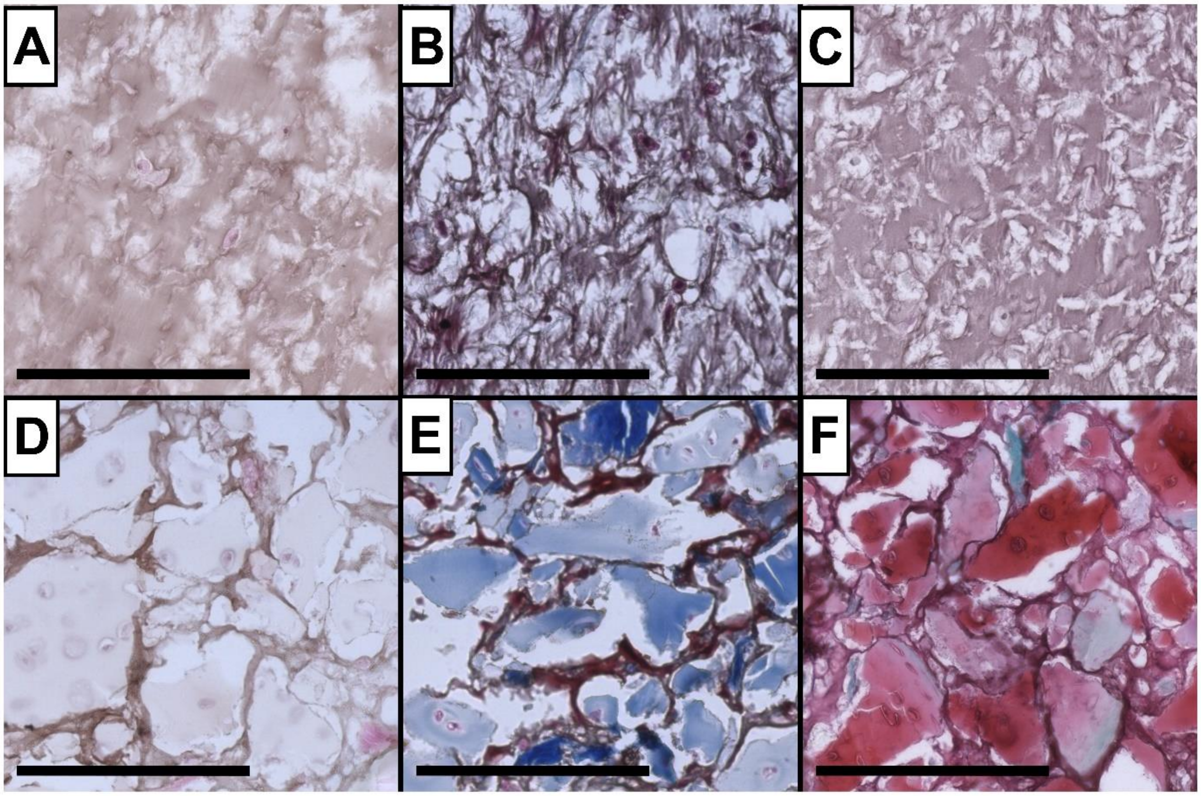

Figure 4-8: MSC-laden Histology

20x images of cell laden prints using either 5% GelMA with 1%LAP (A-C), or 10% dECM with 5% GelMA, and 1% LAP (D-F), scale bars 200um. A&D) H&E staining, B&E) Masson’s Trichrome, C&F) Safranin-O counter stained with Fast Green.

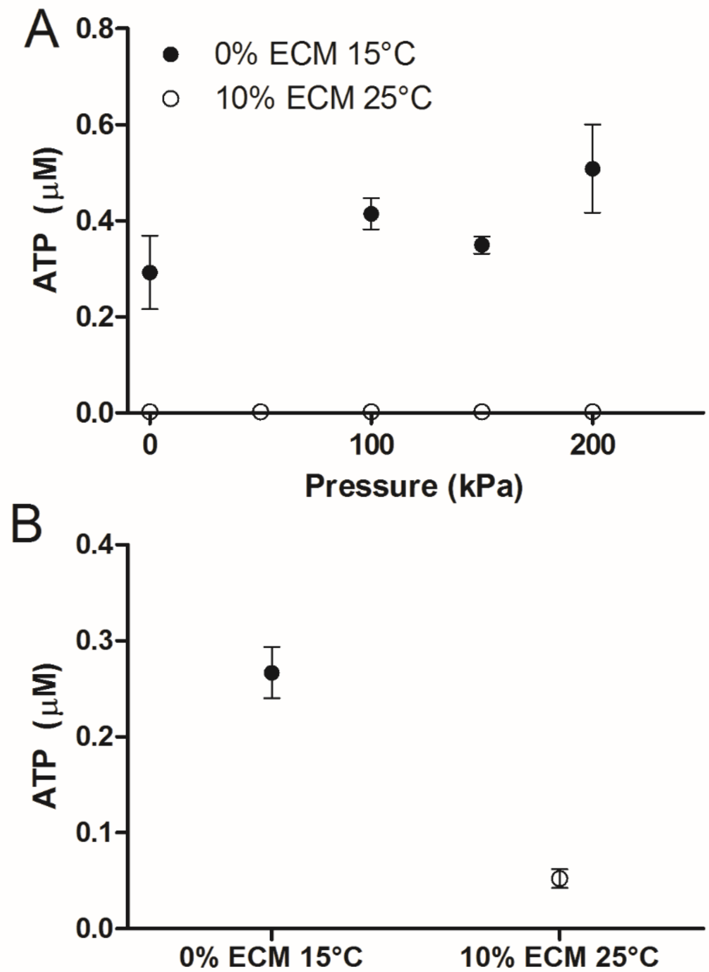

Figure 4-9: Prostate Cancer Cell Viability

A) ATP concentration in cell laden hydrogels printed at varying pressure, plotted as mean ± standard deviation n = 2. ATP was undetectable in 10% ECM 25°C, values shown as zero. B) ATP concentration in hydrogels with cells seeded on surface, mean ± standard deviation n = 2.

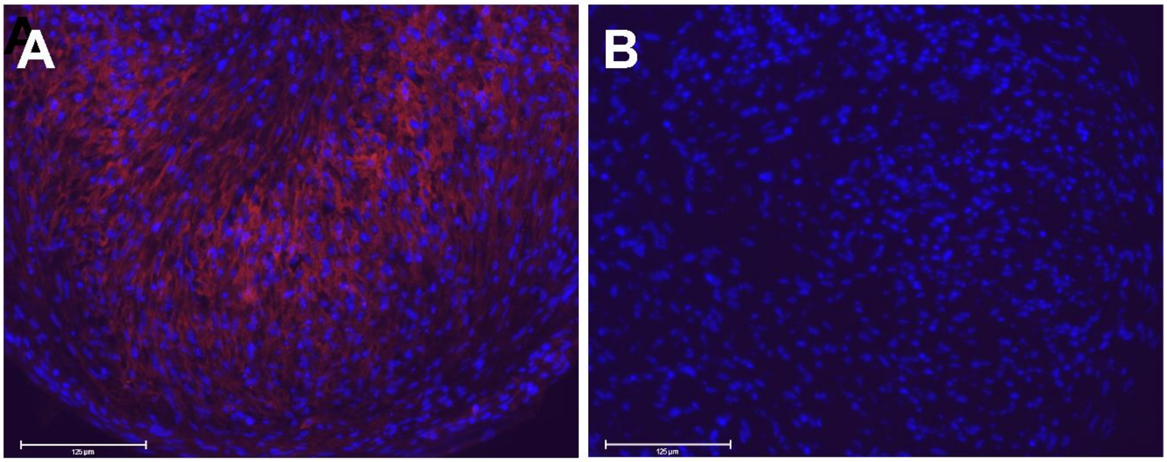

Figure 4-10: Chondrogenic pellet differentiation

A) pellet stained for aggrecan and DAPI, B) secondary only control with DAPI, scale bar 125µm.

Supplementary Table 1						
ECM Concentration	τ_o		k		n	
0%	0.01	-0.01	0.01	0.01	1.04	0.88
5%	9.98	-5.31	14.33	-5.18	0.48	0.30
10%	5.40	-0.73	8.42	0.73	0.58	0.20
15%	12.22	-3.07	33.61	14.10	0.44	0.26
20%	28.11	-13.95	133.65	79.93	0.35	0.25

Table 4-1: Herschel-Bulkley Model Parameters

95% Confidence Intervals (Bonferroni corrected) for Parameters of Herschel-Bulkley Model fit.

20 Ga		10%dECM 25°C	0%dECM 15°C
Pressure (kPa)	P value	Mean (mm)	Mean (mm)
50	0.0004	0.41 ± 0.07	1.20 ± 0.11
75	0.0077	0.85 ± 0.12	1.21 ± 0.05
100	0.0233	1.22 ± 0.04	1.54 ± 0.15
125	0.0029	1.75 ± 0.11	1.32 ± 0.04
150	0.0009	2.28 ± 0.06	1.69 ± 0.10
175	0.0078	2.76 ± 0.07	1.84 ± 0.32
200	0.4582	3.00 ± 0.15	2.80 ± 0.38

20 Ga		0%dECM 15°C	5%dECM 25°C
Pressure (kPa)	P value	Mean (mm)	Mean (mm)
50	0.0021	1.20 ± 0.11	2.67 ± 0.34
75	0.0057	1.21 ± 0.05	2.82 ± 0.52
100	0.0060	1.54 ± 0.15	2.73 ± 0.36
125	0.0001	1.32 ± 0.04	2.78 ± 0.17

22 Ga		10%dECM 25°C	0%dECM 15°C
Pressure (kPa)	P value	Mean (mm)	Mean (mm)
50	0.0040	0.47 ± 0.12	0.93 ± 0.06
75	0.0087	0.64 ± 0.18	1.25 ± 0.13
100	0.0047	0.58 ± 0.03	1.42 ± 0.25
125	0.0012	0.98 ± 0.04	1.28 ± 0.04
150	0.1631	1.39 ± 0.11	1.70 ± 0.30
175	0.5372	1.66 ± 0.08	1.79 ± 0.34
200	0.1225	1.73 ± 0.19	2.86 ± 0.99

22 Ga		0%dECM 15°C	5%dECM 25°C
Pressure (kPa)	P value	Mean (mm)	Mean (mm)
75	0.0015	1.25 ± 0.13	0.68 ± 0.01
100	0.3328	1.42 ± 0.25	1.25 ± 0.03
125	0.0346	1.28 ± 0.04	1.69 ± 0.22
150	0.0196	1.70 ± 0.30	2.35 ± 0.03

23 Ga		10%dECM 25°C	0%dECM 15°C
Pressure (kPa)	P value	Mean (mm)	Mean (mm)
75	0.0000	0.25 ± 0.04	0.95 ± 0.03
100	0.0011	0.36 ± 0.02	1.18 ± 0.17
125	0.0001	0.57 ± 0.05	1.17 ± 0.04
150	0.0181	0.76 ± 0.05	1.39 ± 0.28
175	0.0002	0.94 ± 0.04	1.33 ± 0.04
200	0.1313	1.26 ± 0.03	1.65 ± 0.35

23 Ga		0%dECM 15°C	5%dECM 25°C
Pressure (kPa)	P value	Mean (mm)	Mean (mm)
75	0.0001	0.95 ± 0.03	0.47 ± 0.04
100	0.0045	1.18 ± 0.17	0.6 ± 0.05
125	0.0017	1.17 ± 0.04	0.95 ± 0.03
150	0.6046	1.39 ± 0.28	1.3 ± 0.03
175	0.0386	1.33 ± 0.04	1.46 ± 0.07
200	0.6458	1.65 ± 0.35	1.75 ± 0.11

Table 4-2: T-test comparisons of Linear Resolution

T-test comparisons of Linear Resolution varying tip gauge and driving pressure, 10% dECM at 25°C vs GelMA alone at 15°C, GelMA alone at 15°C vs 5% dECM at 25°C.

Chapter 5 Biomechanical Characterization of Rabbit Tracheal Autografts: A Model for the Study of Neocartilage Growth

5.1: Overview:

The objective of this *in vivo* pilot study was to evaluate and compare full segment tracheal autografts to naive tracheal tissue in a rabbit model. Two sets of three rabbit tracheae were examined: 1) naïve trachea control. 2) tracheae with medial full segment autografts. Full segments of the trachea were resected and reimplanted as autografts. After 4 weeks, the tracheae were evaluated using micro-CT, mechanical testing, and histology. Micro CT revealed minimal stenosis at the anastomosis sites of the autografts, with a maximum of 34±4% occlusion of the airway. Mechanical testing showed significant stiffening of the autografted trachea compared to control, 0.24±0.04 N/mm and 0.13±3=0.03 N/mm for 50% compression respectively. Histology showed new cartilage growth in the autografted tissue. We demonstrate a model for rabbit tracheal transplants and show the development of new tracheal cartilage after transient ischemia. These results indicate this is a promising model to further investigate the origin of new tracheal chondrocytes after injury and the mechanism for their recruitment and differentiation.

5.2: Introduction:

Long segment reconstruction of human trachea presents a technical challenge.[17] Since the trachea lacks any large blood vessels to anastomose and immediately integrate donor tissues into the host vascular system, transplanted tissue relies on indirect vascularization from the surrounding tissue.[102] The few published successful human tracheal transplants have used a two-phase heterotopic approach to first pre-vascularize the graft tissue in a highly vascularized location, like the omentum or forearm, then move the implant to its orthotopic position in a second surgery.[103–106] Fortunately, improvements in microvascular surgery further mitigate this issue. In January 2021, surgeons at Mt Sinai performed the first successful human tracheal transplant. However, even with this accomplishment complete understanding of how the donor tissue integrates with the host, affects regeneration, and impacts long-term outcomes has not been achieved.

Rabbits are commonly used as animal models for tracheal transplant studies.[6] With their smaller size, surgical anastomosis for vascularization is unnecessary for graft survival.[107,108] Previous studies have focused on evaluating the tracheal epithelium, which, despite initially suffering from ischemic damage, generally recovers two weeks after surgery.[109] However, in humans and larger animals, one of the risks after transplantation is the degradation of cartilage and its replacement with scar tissue.[17] These degraded tracheal sections weaken and collapse, inhibiting normal respiration. Based on this trend, we hypothesized the autografted tracheal tissue will weaken post-transplant compared to a naïve control.

5.3: Materials and Methods:

5.3.1: Autograft Surgery Procedure

All rabbit studies were done under supervision of the Institutional Animal Care and Use Committee (IACUC Protocol 1903-36911A). New Zealand white rabbits were randomized as either autograft recipients (rAG) or as naive controls (rNC). Anesthesia was induced using ketamine hydrochloride (10-40 mg/kg) and xylazine (3-5 mg/kg) via intramuscular injection and maintained using isoflurane and propofol inhalation throughout the surgery. The trachea was accessed through a vertical cervical incision; then a segment of the trachea was resected and completely removed it from the surrounding tissue. The resected segment was reimplanted as an autograft with the cut ends anastomosed (**Figure 5-1**). To maximize vasculature around the transplanted tissue, the omentum was accessed through a second incision in the abdomen, mobilized, tunneled substernally, and wrapped around the grafted trachea. The animals were then observed for up to four weeks, at which point the tracheae were excised for analysis.

5.3.2: Micro CT Imaging

Excised tracheae were suspended with a 3D printed frame and scanned using a X-TEK XT H 225 micro-CT scanner (METRIS, Leuven, Belgium) (**Figure 5-2**). The scans were processed with CT Pro 3D (XTEK) and VGSTUDIO Max 3.2, exporting transverse section DICOM files. The transverse images were analyzed using the cross sectional area tool in 3D Slicer to measure the area of the airway in each slice.[101] The resulting data were down sampled by averaging every 10, 0.04 µm thick, sections.

5.3.3: Mechanical Testing

Tracheae were separated into approximately 1 cm segments and analyzed using a tube flattening test. The flattening test was performed using the parallel plate apparatus on the MACH-1 mechanical testing system equipped with a 10kg load cell (Biomomentum, Laval, QC, CA). The tracheal segments were compressed at a constant rate of 0.042 mm/s, similar to other studies.[110] The resistive force was normalized by segment length and by cartilage ring number.

5.3.4: Histology

Tracheal segments were frozen in OCT for histological evaluation. 7 um sections were cut and stained using hematoxylin and eosin, Masson’s trichome, and safranin-O counterstained with fast green (Sigma Aldrich, St. Louis, MO).

5.4: Results:

Of the 3 autograft rabbits, one died prematurely due to perforated stomach caused by a pyloric stenosis. Rabbit sex, weight, and survival are shown in **Table 5-1**.

5.4.1: Micro-CT

Micro-CT imaging showed minimal difference between the average airway area for the naïve (24± 2 mm^2) and autografted tracheae (23±5 mm^2) throughout the entire trachea (**Figure 5-3**). However, there was notable stenosis at the anastomoses of the autografts resulting in a maximum of 34±4% occlusion of the airway. This occlusion would be a grade I, using the Cotton-Meyer scale.[111]

5.4.2: Mechanics

According to the literature on rabbit tracheal mechanics, normally the force required to flatten the trachea decreases along the descending trachea.[110] This was seen in the naïve native trachea segments where the superior and medial segments are similar while the inferior segments exhibit less resistance to compression. However, in the autografted trachea, the medial section containing the graft required significantly greater flattening force than the superior segment per length, 0.24±0.04 N/mm and 0.13±3=0.03 N/mm for 50% compression respectively (**Figure 5-4**). This difference could be due to overlapped cartilage, increasing the stiffness (**Figure 5-5).** To account for this, the compression data were also normalized by the number of rings in each segment (**Figure 5-6**). These relationships persisted for the autograft trachea even after normalizing by the number of tracheal rings in each segment, with 0.28±0.07 N/ring for the autografts and 0.12±0.03 N/ring for the control at 50% compression.

5.4.3: Histology

Examining the tissue histologically after H&E staining revealed the emergence of dense cell regions between the tracheal cartilage rings in the autograft (**Figure 5-7A**). While this was not seen in the surrounding trachea (**Figure 5-7B**), it was present in the center of the graft (**Figure 5-7C**) and near the anastomoses (**Figure 5-7D**). To further identify this tissue, Masson's trichrome staining showed a loosely packed, unaligned network of collagens (**Figure 5-8B**) while in the naïve tissue this region was densely packed and aligned (**Figure 5-8A**). Safranin-O staining also showed an abundance of proteoglycans in this region, resembling nascent cartilage **(Figure 5-8D**). This neocartilage increased the cross-sectional area of cartilage in the sectioned graft by 19±1%. In the naïve trachea, proteoglycans were more discreetly contained in the cartilage rings (**Figure 5-8C**).

5.5: Discussion:

This study characterized the altered biomechanical properties of tracheal autografts. The rabbit autografts resulted in minimal stenosis, with two out of three animals surviving the entire 4-week time course. The cause of death for the animal that did not survive the time course, was a perforated stomach caused by severe pyloric stenosis, which is not uncommon in rabbits. Initially this study was intended to evaluate MSC-laden, 3D bioprinted constructs *in vivo* to create bioengineered, cartilage tissue; i.e. first implanting the tissue into the omentum and allowing it to mature, then transplanting it into the trachea with the mobilized omentum to maintain blood flow. However, the implanted constructs were remodeled in the host rabbit and were not suitable for the second transplant procedure. Instead, the autograft tissue initially planned as a control was compared to naïve trachea. Interestingly, the autografted tracheae stiffened significantly compared to naïve counterparts. While this stiffening could have been the result of suturing multiple cartilage rings together, this trend persisted even after normalizing by ring number. Histology suggested new cartilage growth in the transplanted tissues, with the emergence of nascent cartilage growth between mature cartilage rings. This new growth was most likely due to the hypoxic conditions in the ischemic tissue that triggered resident stem cells to differentiate.[112,113]

Resident stem cells have been implicated in the development of new cartilage growth in aortic allografts used as trachea replacements in sheep.[114–117] In the mentioned studies, new cartilage growth was observed within two months and remodeled into tracheal tissue with discrete cartilage rings 6-36 months after implantation.[115] Stented, decellularized aortic allografts for tracheal transplants have been tested in humans and demonstrated new cartilage growth; however the cell origin and signaling mechanism behind this phenomenon has not been fully described.[118] In this pilot study, new cartilage growth was seen in less than 4 weeks, indicating this model may be an efficient method to further probe the signaling mechanism of new cartilage growth and the development of discrete tracheal rings.

5.6: Acknowledgements

I would like to acknowledge our surgical collaborators Benjamin Zhang, MD; Ilitch Diaz Gutierrez, MD; and Rafael Andrade, MD. I would like to thank Experimental Surgical Services and specifically Peggy Norris, Teri Ulferts, and Michele Dunning for their help both during surgeries and in preparation for our animal protocols. I would like to thank Haylie Helms for her work collecting and processing samples for analysis. This work was supported by the National Institutes of Health NHLBI F31 (5F31HL142313) awarded to Z. P. Galliger, a CTSI Translational Research Development Program grant awarded to Z. P. Galliger (from the National Center for Advancing Translational Sciences (grant UL1TR002494. PI: B. Blazar. The content is solely the responsibility of the authors and does not necessarily represent the official views of the National Institutes of Health's National Center for Advancing Translational Sciences.).

5.7: Figures

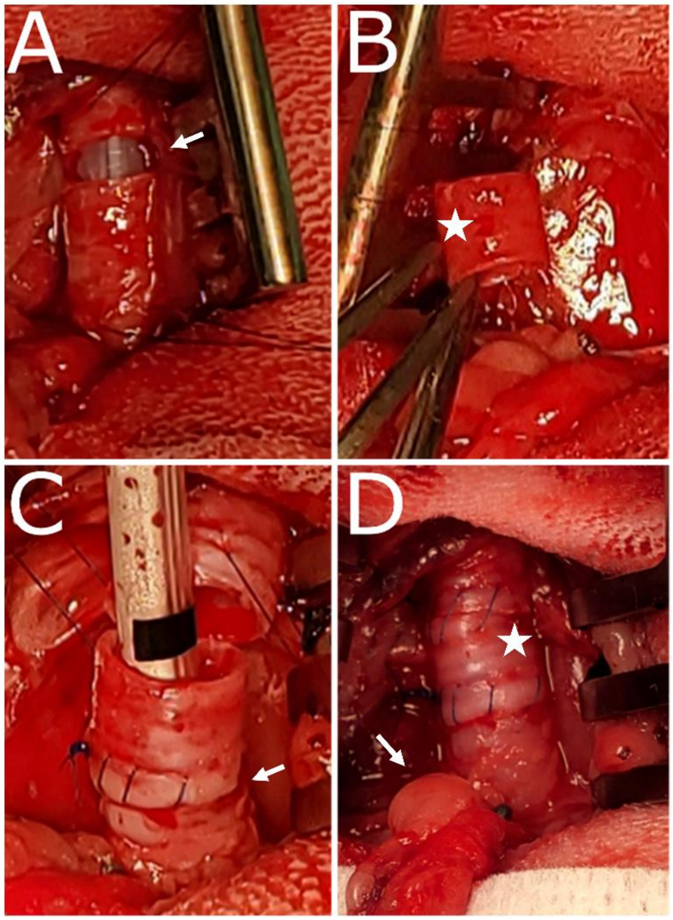

Figure 5-1: Rabbit Tracheal Resection and Reimplantation

Tracheal segment resection (A&B) and reimplantation (C&D). A) Excising trachea around intubation tube (arrow). B) Resected trachea segment (star). C) Reimplanting trachea, inferior anastomosis (arrow). D) Reimplanted autograft (star), and omentum (arrow) before being sutured over autograft.

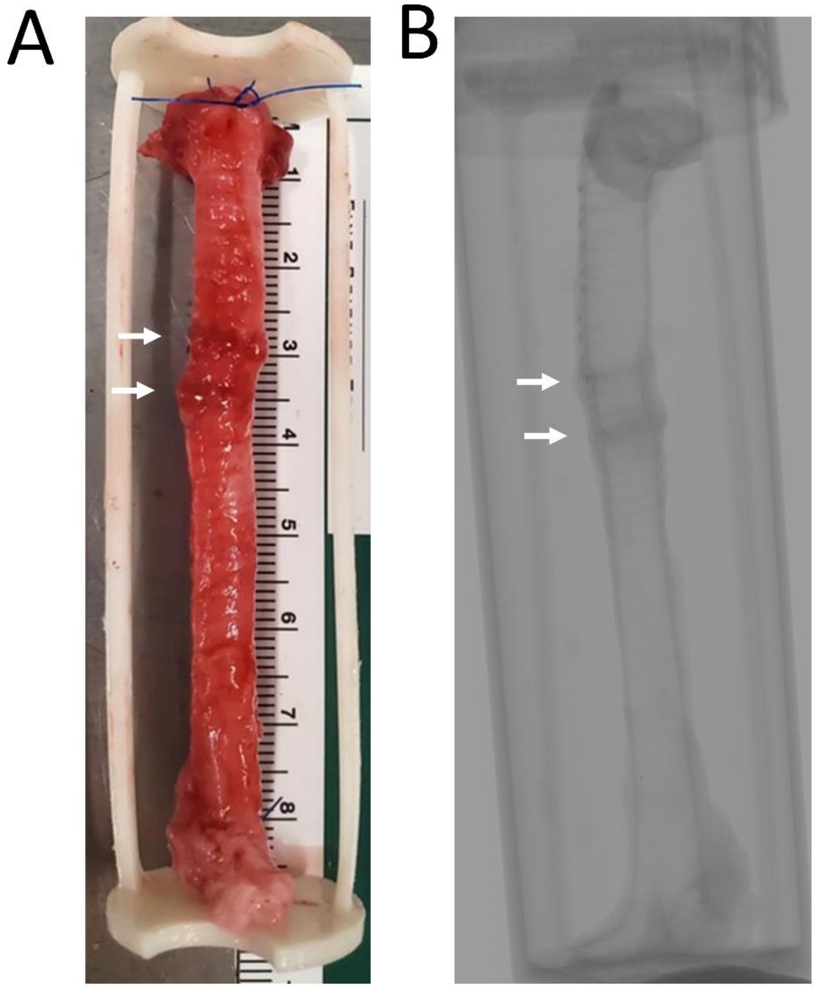

Figure 5-2: Micro CT imaging of excised tracheae

Micro CT imaging of excised tracheae. A) Trachea suspended on 3D printed frame. B) Micro CT image of trachea. White arrows indicated anastomosis on tracheal graft.

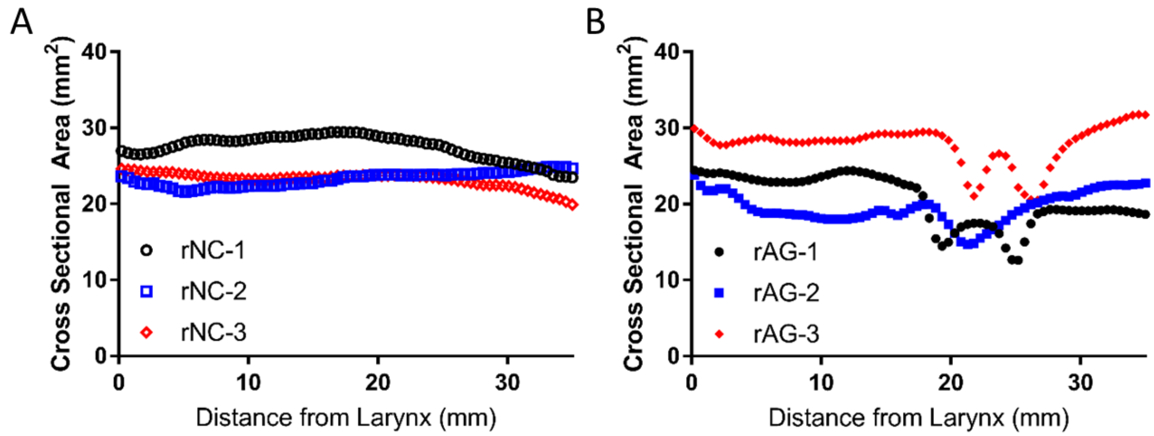

Figure 5-3: Airway Cross sectional area

A) Naïve trachea with an average area of 24± 2 mm^2 and B) autografted tracheae with an average area of 23±5 mm^2.

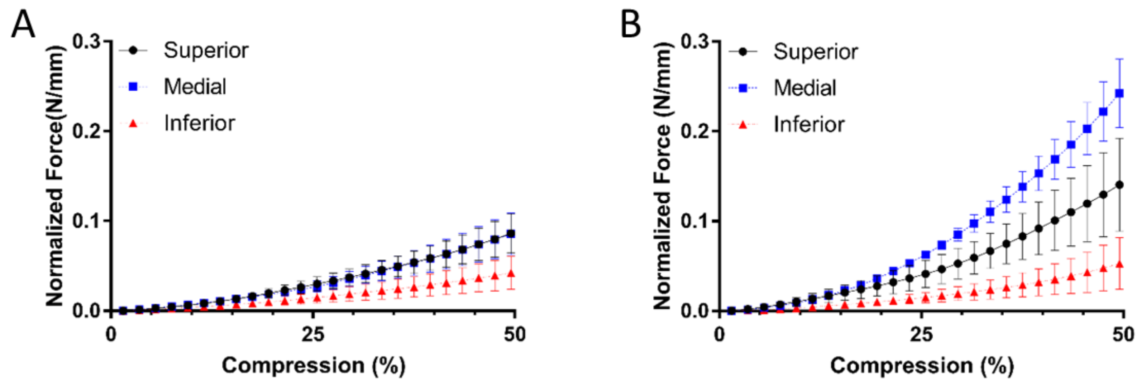

Figure 5-4: Trachea flattening force

Trachea flattening force of naive trachea (A) and tracheal autografts (B). Mean ± StDev, n = 3.

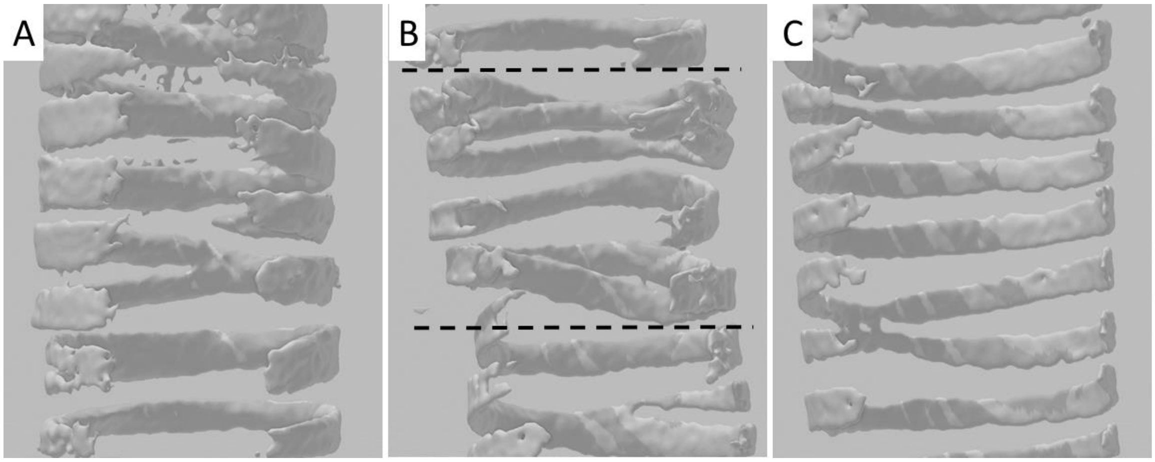

Figure 5-5: 3D Reconstruction of cartilage rings

3D Reconstruction of cartilage rings. A) Trachea superior to the graft. B) The graft region (autograft marked with dotted lines). C) Trachea inferior to the graft.

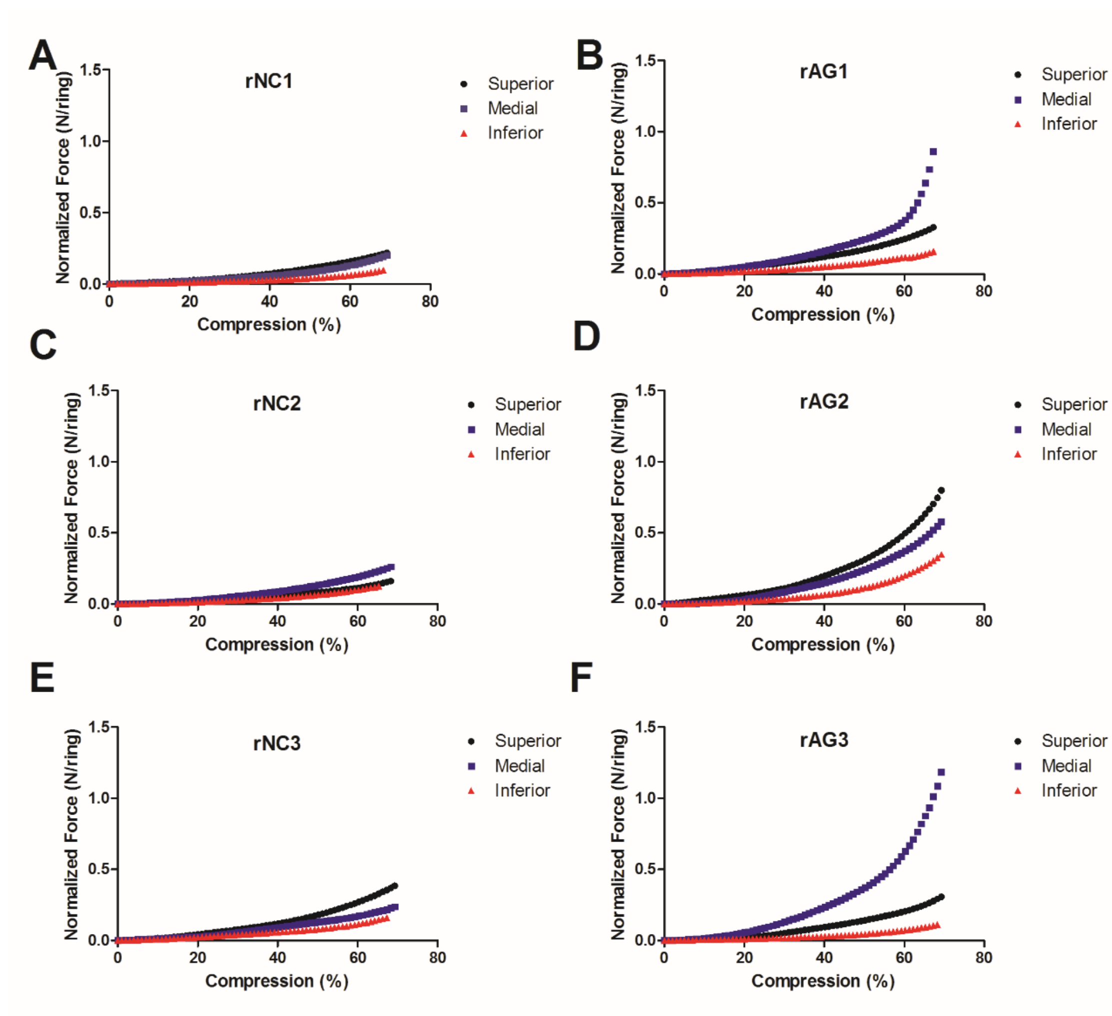

Figure 5-6: Trachea flattening normalized by ring number

Trachea flattening normalized by ring number. Naive trachea (rNT) on the left (A, C, E). Autografted trachea (rAG) on the right (B, D, F).

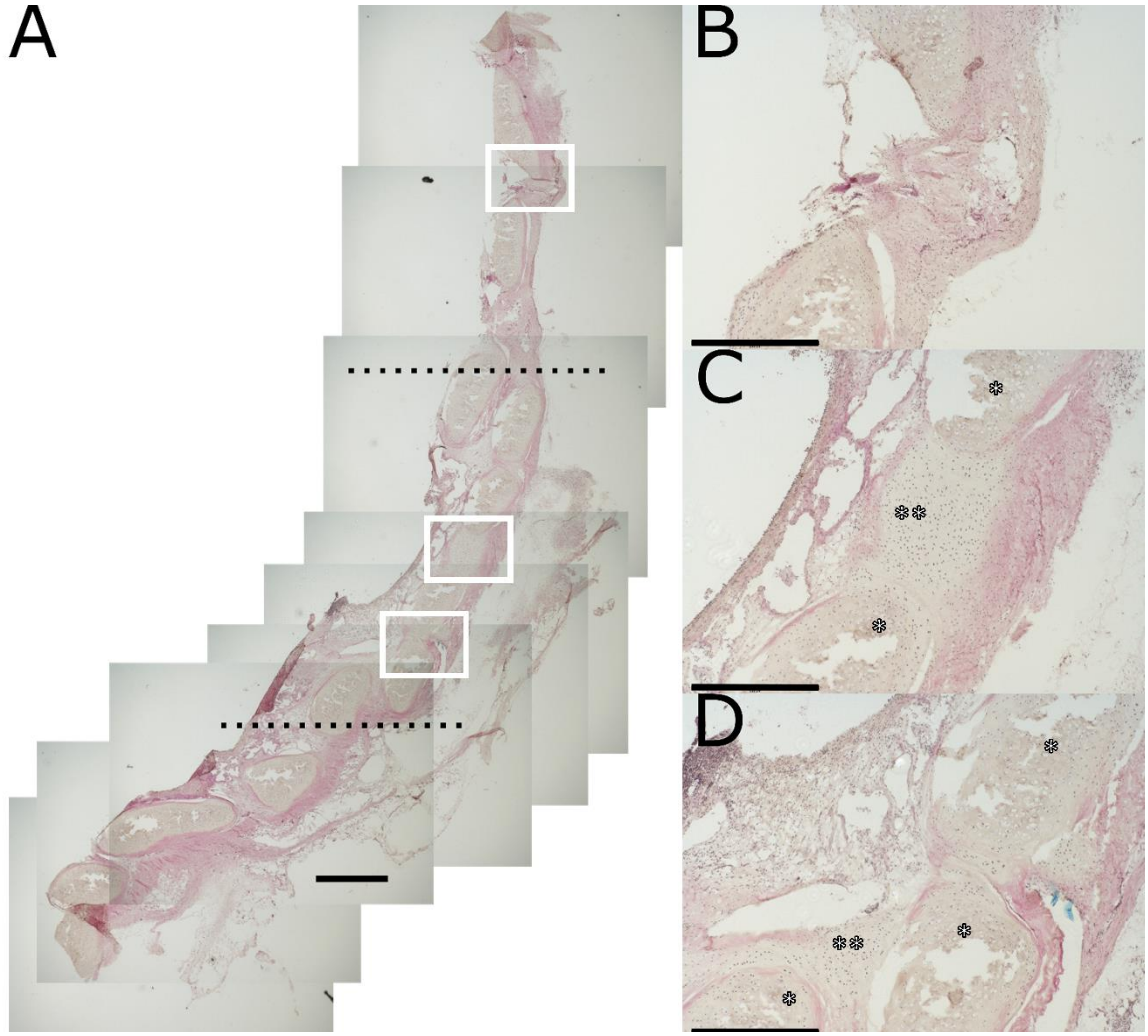

Figure 5-7: H & E staining of tracheal autograft

A) Stitched image of the graft and surrounding tissue, anastomoses marked with dotted lines and higher magnification images marked with white boxes. Scale bar 1000 µm. B) Space between cartilage rings in the trachea next to the graft. C & D) New cartilage growth (**) between mature rings (*) in the grafted trachea. Scale bar 500 µm.

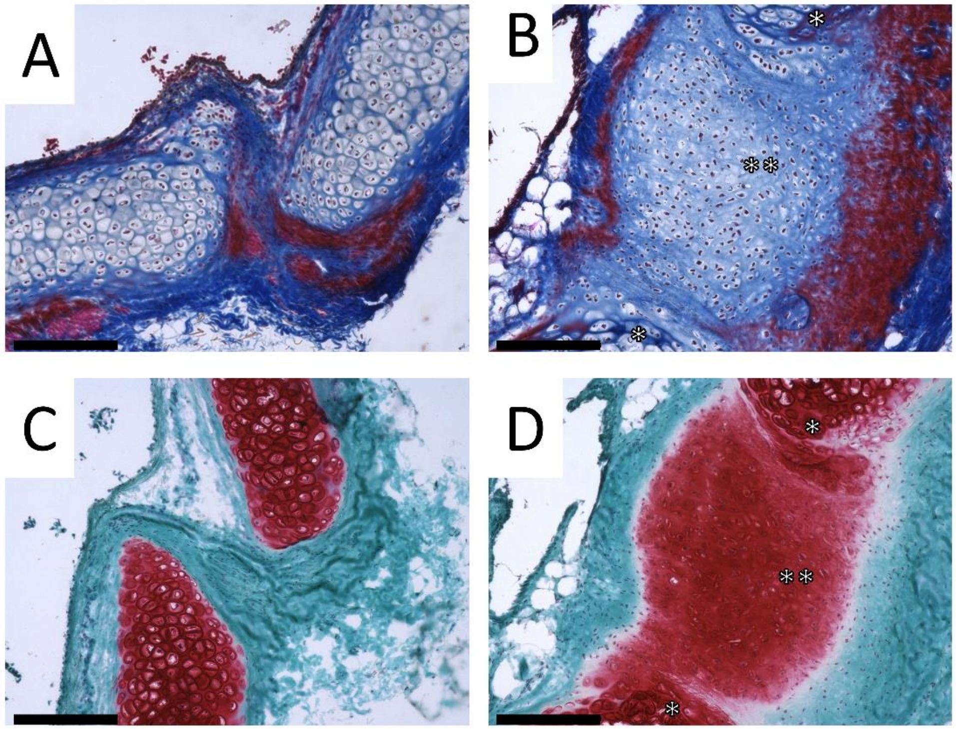

Figure 5-8: Cartilage Growth Histology

Masson’s Trichrome (A&B) and safranin-O counter stained with fast green (C & D). Naive trachea (A & C) and autografted tracheae (B&D). New cartilage growth (**) between mature rings (*) in the grafted trachea, neocartilage increased cartilage area by 19±1%. Scale bar 200 µm.

5.8: Tables

Rabbit	Sex	Weight (kg)	Survival (days)
Autograft (rAG 1)	Female	3.6	28
Autograft (rAG 2)	Male	4.2	3
Autograft (rAG 3)	Male	3.7	28
Control (rNC 1)	Male	3.4	28
Control (rNC 2)	Male	3.5	28
Control (rNC 3)	Male	3.4	28

Table 5-1: Summary of experimental rabbits including sex, weight and survival

Chapter 6 Hollow Organ Bioreactor

To better observe the maturation of 3D printed trachea, a hollow organ bioreactor was developed. This bioreactor rotates around its long axis for luminal cell seeding and providing a transient air-fluid interface, translates along its long axis to provide tensile stretching, and can perfuse media or air through the lumen of the tissue for tunable sheer stress. While other bioreactors have accomplished these actions individually, this bioreactor allows the versatile manipulation of all three at once.[119–121] This design could be further modified to examine tissue properties overtime in response to a variety of stimuli or be used to study *ex vivo* tissues.

The bioreactor components were all 3D printed using a Form2 Printer (FormLabs, Somerville, MA) and FormLabs autoclavable and biocompatible surgical guide resin. The assembly of these components is shown in **Figure 6-1**. This allows for the rapid production and alteration of the components to fit tubular tissues between 5-15mm inner diameter, 6-16mm outer diameter, and 10-28mm long. Tissue loading is shown in **Figure 6-2**. Two luer lock access ports in the base chamber allow for media exchange and monitoring. If connected to a peristaltic pump, media can be drawn from the bottom of the outer chamber with the bottom port and perfused through the top port into the inner lumen of the tissue in a closed loop. If the top port is connected to a respirator pushing and pulling air through the tissue, the bottom port can be easily plugged. Two stepper motors are mounted to the lid base and individually controlled with Arduino boards; these power the rotating and translating heads in the bioreactor. The printed circuit boards (PCB) were manufactured by JLCPCB.COM (Shenzhen, China) and the board design shown in **Figure 6-3**. Components used were Arduino Nano, ULN2003APG 7-Channel Transistor Array, and a 5 pin JST connector.

The rotating head turns the tissue in alternating directions, this provides full rotation while decreasing risk of gears jamming. If the chamber media is filled to partially expose the tissue, this rotation also introduces a transient air-fluid interface, as seen in other tracheal bioreactors.[122] An air-fluid interface could also be introduced by completely submerging the tissue and flowing air through lumen, more accurately recapitulating the native airway. One future experiment of interest is seeding the lumen of a bioprinted airway with human bronchial epithelial cells and exposing them to both types of air-fluid interfaces to characterize differences in cell polarity and the integrity of the epithelial barrier.

The translating head moves the tissue with a rack and pinion gear system. While incorporating a force transducer could provide information on tissue maturation by monitoring changes, this strain-controlled system was used for simplicity and to minimize unit cost. The current design allows for a linear resolution of approximately 0.05 mm/step, calculated by **Equation 6-1** where r is the radius of the pinion and n is the number of steps for the stepper motor to make a full rotation.

$$\frac{2\pi r_{pinion}}{n_{stepper\ motor}} = x\ mm/step \qquad \text{Equation 6-1}$$

Literature has shown that low strain cyclical loading can strengthen collagen-based constructs.[123–125] This could be used to strengthen mechanically subpar constructs into robust tissues for transplantation or further study. While I was not able to fully utilize this bioreactor during my thesis work, it will be used in future work in the lab examining tracheae and bronchi. This bioreactor could also be used to study

Figures:

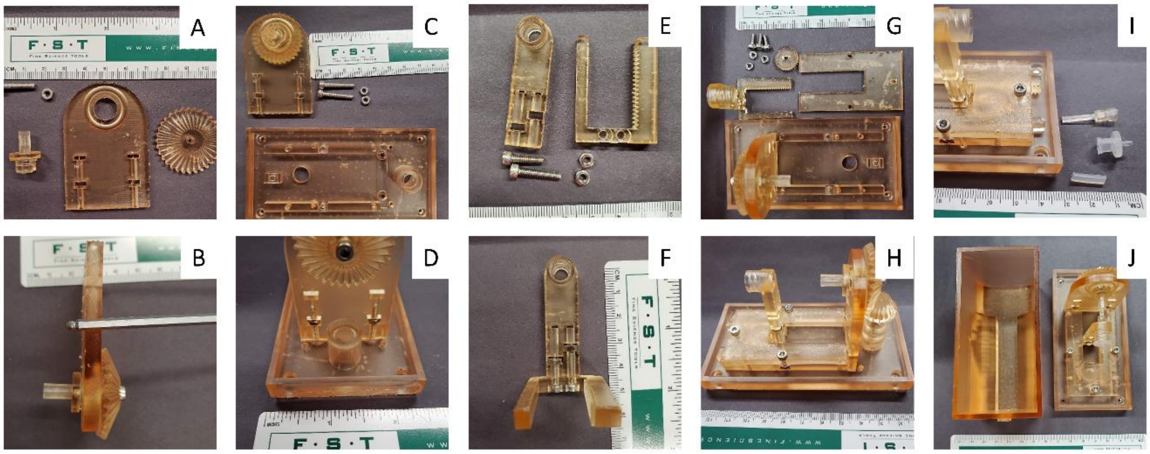

Figure 6-1: 3D Printed Bioreactor Assembly

A & B) Rotating head assembly. C & D) Installing rotating head to lid base. E & F) Translating head assembly. G & H) Installing translating head to lid base. I & J) Installing tissue holder.

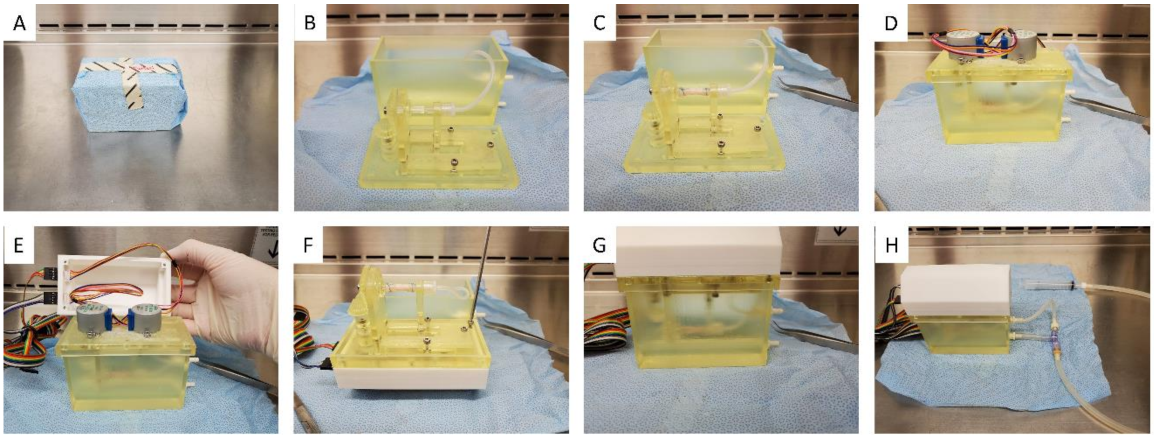

Figure 6-2: Bioreactor Tissue Loading

A) Wrapped autoclaved bioreactor. B) opened bioreactor. C) Tissue loaded onto tissue holder. D) Motors installed on top of lid base. E & F) Lid cap installed over motors. G) Assembled bioreactor. H) One way flow loop with syringe connected to side ports.

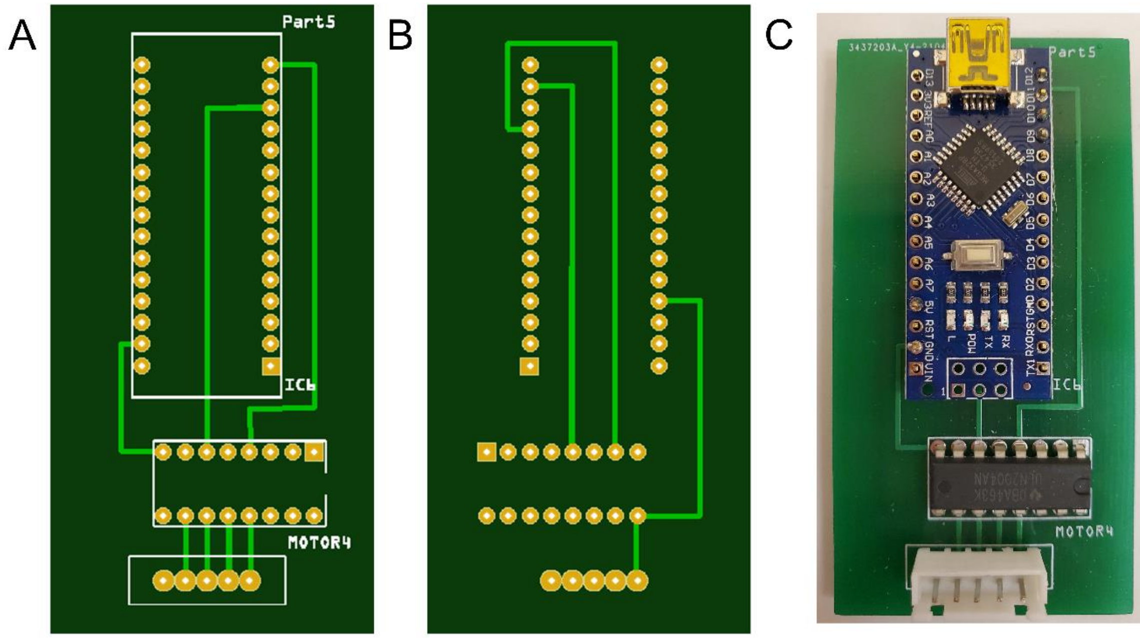

Figure 6-3: Arduino Motor Controller

A) Printed Circuit Board (PCB) Top. B) PCB Bottom. C) PCB with soldered components.

Chapter 7 Conclusions and Future Directions

7.1: Photo-crosslinkable tracheal cartilage-derived extracellular matrix hydrogels

While the full relationship between the ECM and cell behavior is not fully understood, we can continue to develop new methods of incorporating its benefits in tissue-engineered constructs. This work has shown tracheal cartilage ECM has chondrogenic effects similar to articular cartilage, although the long-term effects and tissue stability remain undetermined. While chemically modifying this ECM allows it to better integrate into GelMA-based hydrogels, it decreases its ability to support differentiation of MSCs. The next step for this works lies in identifying the key ECM components responsible for the chondrogenic effect. Using mass spectroscopy with liquid chromatography to compare the composition of pepsin-digested and urea-extracted ECM may show what components they share. The effects of those shared components on MSCs can be examined both in 2D and 3D culture, similar to published studies on stem cell differentiation.[126–129] To screen for interactions more efficiently, hydrogel gradients of these components could be generated and seeded with cells. A complex gradient could be created by 3D bioprinting multiple bioinks through a microfluidic print head while changing their relative driving pressures to create a continuous, compositional gradient. A microfluidic bioprinter capable of these kinds of experiments is commercially available from Aspect Biosystems (Vancover, CA). The gradient tissue could then be analyzed using a 2D PCR approach, where the tissue is divided into a grid and each sample is run indiviually.[130]

7.2: Extracellular Matrix Microparticles as a Stabilizing Additive for 3D Bioprinting

This work shows the utility of ECM-derived particles as a bioink additive from a rheological and print parameter perspective. These particles significantly improve the printability of GelMA bioinks at room temperature without requiring support or suspension gels for printing complex structures. This lowers the barriers to bioprinting complex tissue models and circumvents many manufacturing challenges. However, the largest question remaining in this work is why do cells embedded in the particle-laden bioinks have such low viability? There are several potential causes that could be explored. The ECM particles could be a physical barrier, decreasing the diffusion of oxygen and nutrients to the embedded cells. The cells could experience increased stresses during the mixing process. There could be physical forces or osmotic pressures exerted on the cells by the swelling particles. Or the cells could be negatively responding to degraded ECM components.[96] To screen for all of these potential causes, the next set of experiments should screen for markers of apoptosis and necrosis, such as lactate dehydrogenase (LDH) released when the cell's membrane is compromised, or histologically looking at nuclear morphology.[131]

Continuing this work, the biological effects of these particles should be examined beyond cell viability. Evaluating the ECM particles' ability to influence cells and mature into viable tissues will be key to developing more reliable tissue grafts and accurate disease models. Further, it will be of interest to examine the effects of ECM particles derived from other tissues, examining if these rheological aspects are unique to cartilage ECM or widely applicable. While the cartilage ECM contains large amounts of proteoglycans and glycosaminoglycans, other tissues that are primarily collagen, such as muscle, may not behave in the same manner.

7.3: Biomechanical Characterization of Rabbit Tracheal Autografts: A Model for the Study of Neocartilage Growth

While this pilot study demonstrates the stiffening biomechanics of rabbit tracheal transplants, it also raises questions about new cartilage growth in the trachea. Similar cartilage growth has been observed in sheep and human tracheal grafts. However, the source of this new cartilage tissue has not been confirmed. It has been speculated that pulmonary fibroblasts undergo chondrogenesis and become the neocartilage.[112] However, a type of migratory chondrogenic progenitor cell found in other hyaline cartilage could be responsible.[132,133] Because this rabbit model of neocartilage growth develops relatively quickly and would generally cost less than human or sheep studies, it could be an idea model to further explore the source of these nascent chondrocytes and the mechanism for their recruitment and differentiation. Answering these questions will not only help develop better tracheal grafts but may offer new approaches to treating other cartilage-related maladies.

Further, this model could be used to evaluate the ability of acellular grafts to recruit host cells and form neocartilage. Using a multiheaded 3D bioprinter, an acellular ECM based graft could be printed with a biodegradable, polycaprolactone (PCL) support either as an internal stent or as a deformable mesh through the graft walls. Decellularized, tissue engineered vascular grafts would also be of interest to test, such as those produced by Laura Niklason or Bob Tranquillo.[134,135]

Chapter 8 References

1. Galliger Z, Vogt CD, Panoskaltsis-Mortari A. 3D bioprinting for lungs and hollow organs. *Translational Research*. 2019;211:19-34. doi:10.1016/j.trsl.2019.05.001
2. Weiss DJ, Elliott M, Yang Q, Poole B, Birchall M. Tracheal bioengineering: The next steps: Proceeds of an international society of cell therapy pulmonary cellular therapy signature series workshop, Paris, France, April 22, 2014. *Cytotherapy*. 2014;16(12):1601-1613. doi:10.1016/j.jcyt.2014.10.012
3. Holbert JM, Strollo DC. Imaging of the normal trachea. *Journal of thoracic imaging*. 1995;10(3):171-179.
4. Abbott C. Dimensions of the Normal Human Trachea. *American Roentgen Ray Society*. 1984;141:903-906.
5. Ott LM, Vu CH, Farris AL, et al. Functional Reconstruction of Tracheal Defects by Protein-Loaded, Cell-Seeded, Fibrous Constructs in Rabbits. *Tissue Engineering Part A*. 2015;21(17-18):2390-2403. doi:10.1089/ten.tea.2015.0157
6. ten Hallers EJO, Rakhorst G, Marres HAM, et al. Animal models for tracheal research. *Biomaterials*. 2004;25(9):1533-1543. doi:10.1016/S0142-9612(03)00500-3
7. Grillo HC, Donahue DM, Mathisen DJ, Wain JC, Wright CD. Postintubation tracheal stenosis. Treatment and results. *The Journal of Thoracic and Cardiovascular Surgery*. 1995;109(3):486-493. doi:10.1016/S0022-5223(95)70279-2
8. Squire R, Brodsky L, Rossman J. The role of infection in the pathogenesis of acquired tracheal stenosis. *Laryngoscope*. 1990;100(7):765-770.
9. Carden, Kelly A., MD; Philip M. Boiselle, MD, FCCP; David A. Waltz, MD; and Armin Ernst, MD F. reviews Tracheomalacia and Tracheobronchomalacia in Children and Adults *. *Chest*. 2005;127:984-1005. doi:10.1378/chest.127.3.984
10. Ergun S, Tewfik T, Daniel S. Tracheal agenesis: A rare but fatal congenital anomaly. *McGill Journal of Medicine*. 2010;13(1):10-12.
11. van Veenendaal MB, Liem KD, Marres H a. Congenital absence of the trachea. *European journal of pediatrics*. 2000;159(1-2):8-13.
12. Paraschiv M. Tracheoesophageal fistula - a complication of prolonged tracheal intubation. 2014;7(4):516-521.
13. Noppen M, Schlesser M, Meysman M, D'Haese J, Peche R, Vincken W. Bronchoscopic balloon dilatation in the combined management of postintubation stenosis of the trachea in adults. *Chest*. 1997;112(4):1136-1140. doi:http://dx.doi.org/10.1378/chest.112.4.1136
14. Shapshay SM, Hybels RL, Beamis JF, Bohigian RK. Endoscopic treatment of subglottic and tracheal stenosis by radial laser incision and dilation. *Annals of Otology, Rhinology and Laryngology*. 1987;96(6):661-664.
15. Otti AG, Jaus MO, Barale D, et al. The first tissue-engineered airway transplantation: 5-year follow-up results. *The Lancet*. 2014;383(9913):238-244. doi:10.1016/S0140-6736(13)62033-4

16. Macchiarini P, Jungebluth P, Go T, et al. Clinical transplantation of a tissue-engineered airway. *The Lancet*. 2008;372(9655):2023-2030. doi:10.1016/S0140-6736(08)61598-6
17. Grillo HC. Tracheal replacement: A critical review. *Annals of Thoracic Surgery*. 2002;73(6):1995-2004. doi:10.1016/S0003-4975(02)03564-6
18. Lin CH, Su JM, Hsu SH. Evaluation of type II collagen scaffolds reinforced by poly(epsilon-caprolactone) as tissue-engineered trachea. *Tissue engineering Part C, Methods*. 2008;14(1):69-77. doi:10.1089/tec.2007.0336
19. Nakamura T, Ohmori K, Kanemaru SI. Tissue-engineered airway and “in situ tissue engineering.” *General Thoracic and Cardiovascular Surgery*. 2011;59(2):91-97. doi:10.1007/s11748-010-0677-9
20. Robey TC, Välimaa T, Murphy HS, Tôrmâlâ P, Mooney DJ, Weatherly R a. Use of internal bioabsorbable PLGA “finger-type” stents in a rabbit tracheal reconstruction model. *Archives of otolaryngology--head & neck surgery*. 2000;126(8):985-991.
21. Kanzaki M, Yamato M, Hatakeyama H, et al. Tissue engineered epithelial cell sheets for the creation of a bioartificial trachea. *Tissue engineering*. 2006;12(5):1275-1283. doi:10.1089/ten.2006.12.1275
22. Weidenbecher M, Tucker HM, Awadallah A, Dennis JE. Fabrication of a neotrachea using engineered cartilage. *The Laryngoscope*. 2008;118(4):593-598. doi:10.1097/MLG.0b013e318161f9f8
23. Sammartino F, Macchiarini P. Primary Tracheal Tumors. *Lung Cancer: Fourth Edition*. 2014;9781118468:267-277. doi:10.1002/9781118468791.ch17
24. Bader A, Macchiarini P. Moving towards in situ tracheal regeneration: the bionic tissue engineered transplantation approach. *Journal of Cellular and Molecular Medicine*. 2010;14(7):1877-1889. doi:10.1111/j.1582-4934.2010.01073.x
25. Naveau A, Smirani R, Catros S, de Oliveira H, Fricain JC, Devillard R. A Bibliometric Study to Assess Bioprinting Evolution. *Applied Sciences*. 2017;7(12):1331. doi:10.3390/app7121331
26. Derakhshanfar S, Mbeleck R, Xu K, Zhang X, Zhong W, Xing M. 3D bioprinting for biomedical devices and tissue engineering: A review of recent trends and advances. *Bioactive Materials*. 2018;3(2):144-156. doi:10.1016/j.bioactmat.2017.11.008
27. Bishop ES, Mostafa S, Pakvasa M, et al. 3-D bioprinting technologies in tissue engineering and regenerative medicine: Current and future trends. *Genes and Diseases*. 2017;4(4):185-195. doi:10.1016/j.gendis.2017.10.002
28. Tasoglu S, Demirci U. Bioprinting for stem cell research. *Trends in Biotechnology*. 2013;31(1):10-19. doi:10.1016/j.tibtech.2012.10.005
29. Kaye R, Goldstein T, Grande DA, Zeltsman D, Smith LP. A 3-dimensional bioprinted tracheal segment implant pilot study: Rabbit tracheal resection with graft implantation. *International Journal of Pediatric Otorhinolaryngology*. 2019;117(July 2018):175-178. doi:10.1016/j.ijporl.2018.11.010

30. Rutgers M, Pelt MJP Van, Dhert WJA, Creemers LB, Saris DBF. Review Evaluation of histological scoring systems for tissue-engineered , repaired and osteoarthritic cartilage. *Osteoarthritis and Cartilage*. 2010;18(1):12-23. doi:10.1016/j.joca.2009.08.009
31. Bae S woo, Lee KW, Park J hyun, et al. 3D Bioprinted Artificial Trachea with Epithelial Cells and Chondrogenic-Differentiated Bone Marrow-Derived Mesenchymal Stem Cells. *International Journal of Molecular Sciences*. 2018;19(6):1624. doi:10.3390/ijms19061624
32. Park JH, Yoon JK, Lee JB, et al. Experimental Tracheal Replacement Using 3-dimensional Bioprinted Artificial Trachea with Autologous Epithelial Cells and Chondrocytes. *Scientific Reports*. 2019;9(1):2103. doi:10.1038/s41598-019-38565-z
33. Taniguchi D, Matsumoto K, Tsuchiya T, et al. Scaffold-free trachea regeneration by tissue engineering with bio-3D printing†. *Interactive CardioVascular and Thoracic Surgery*. 2018;26(5):745-752. doi:10.1093/icvts/ivx444
34. Machino R, Matsumoto K, Taniguchi D, et al. Replacement of Rat Tracheas by Layered, Trachea-Like, Scaffold-Free Structures of Human Cells Using a Bio-3D Printing System. *Advanced Healthcare Materials*. 2019;1800983:1800983. doi:10.1002/adhm.201800983
35. Hinton TJ, Jallerat Q, Palchesko RN, et al. Three-dimensional printing of complex biological structures by freeform reversible embedding of suspended hydrogels. *Science Advances*. 2015;1(9):e1500758. doi:10.1126/sciadv.1500758
36. Park JH, Hong JM, Ju YM, et al. A novel tissue-engineered trachea with a mechanical behavior similar to native trachea. *Biomaterials*. 2015;62:106-115. doi:10.1016/j.biomaterials.2015.05.008
37. Park JH, Park JY, Nam IC, et al. Human turbinate mesenchymal stromal cell sheets with bellows graft for rapid tracheal epithelial regeneration. *Acta Biomaterialia*. 2015;25:56-64. doi:10.1016/j.actbio.2015.07.014
38. Goldstein TA, Smith BD, Zeltsman D, Grande D, Smith LP. Introducing a 3-dimensionally Printed, Tissue-Engineered Graft for Airway Reconstruction. *Otolaryngology-Head and Neck Surgery*. 2015;153(6):1001-1006. doi:10.1177/0194599815605492
39. Rehmani SS, Al-Ayoubi AM, Ayub A, et al. Three-Dimensional-Printed Bioengineered Tracheal Grafts: Preclinical Results and Potential for Human Use. *The Annals of Thoracic Surgery*. 2017;104(3):998-1004. doi:10.1016/j.athoracsur.2017.03.051
40. Townsend JM, Ott LM, Salash JR, et al. Reinforced Electrospun Polycaprolactone Nanofibers for Tracheal Repair in an In Vivo Ovine Model. *Tissue Engineering Part A*. 2018;24(17-18):1301-1308. doi:10.1089/ten.tea.2017.0437
41. Galliger Z, Panoskaltsis-Mortari A. Tracheal Cartilage Isolation and Decellularization. In: Turksen K, ed. *Decellularized Scaffolds and Organogenesis:*

Methods and Protocols. Springer New York; 2017:155-160. doi:10.1007/7651_2017_52
42. Saldin LT, Cramer MC, Velankar SS, White LJ, Badylak SF. Extracellular Matrix Hydrogels from Decellularized Tissues: Structure and Function. *Acta Biomaterialia*. 2016;49:1-15. doi:10.1016/j.actbio.2016.11.068
43. Badylak SF, Freytes DO, Gilbert TW. Extracellular matrix as a biological scaffold material : Structure and function. *Acta Biomaterialia*. 2009;5(1):1-13. doi:10.1016/j.actbio.2008.09.013
44. Price AP, England KA, Matson AM, Blazar BR, Panoskaltsis-Mortari A. Development of a Decellularized Lung Bioreactor System for Bioengineering the Lung: The Matrix Reloaded. *Tissue Engineering Part A*. 2010;16(8):2581-2591. doi:10.1089/ten.tea.2009.0659
45. Pati F, Jang J, Ha DH, et al. Printing three-dimensional tissue analogues with decellularized extracellular matrix bioink. *Nature communications*. 2014;5:3935. doi:10.1038/ncomms4935
46. Visser J, Levett PA, te Moller NCR, et al. Crosslinkable hydrogels derived from cartilage, meniscus, and tendon tissue. *Tissue engineering Part A*. 2015;21(7-8):1195-1206. doi:10.1089/ten.TEA.2014.0362
47. Benton JA, DeForest CA, Vivekanandan V, Anseth KS. Photocrosslinking of gelatin macromers to synthesize porous hydrogels that promote valvular interstitial cell function. *Tissue engineering Part A*. 2009;15(11):3221-3230. doi:10.1089/ten.TEA.2008.0545
48. Gaudet ID, Shreiber DI. Characterization of methacrylated Type-I collagen as a dynamic, photoactive hydrogel. *Biointerphases*. 2012;7(1-4):1-9. doi:10.1007/s13758-012-0025-y
49. Ying G, Jiang N, Yu C, Zhang YS. Three-dimensional bioprinting of gelatin methacryloyl (GelMA). *Bio-Design and Manufacturing*. 2018;1(4):215-224. doi:10.1007/s42242-018-0028-8
50. Ning L, Mehta R, Cao C, et al. Embedded 3D Bioprinting of Gelatin Methacryloyl-Based Constructs with Highly Tunable Structural Fidelity. *ACS Applied Materials and Interfaces*. 2020;12(40):44563-44577. doi:10.1021/acsami.0c15078
51. Pepelanova I, Kruppa K, Scheper T, Lavrentieva A. Gelatin-methacryloyl (GelMA) hydrogels with defined degree of functionalization as a versatile toolkit for 3D cell culture and extrusion bioprinting. *Bioengineering*. 2018;5(3). doi:10.3390/bioengineering5030055
52. Choudhury D, Tun HW, Wang T, Naing MW. Organ-Derived Decellularized Extracellular Matrix: A Game Changer for Bioink Manufacturing? *Trends in Biotechnology*. 2018;36(8):787-805. doi:10.1016/j.tibtech.2018.03.003
53. Chiang CE, Fang YQ, Ho CT, et al. Bioactive Decellularized Extracellular Matrix Derived from 3D Stem Cell Spheroids under Macromolecular Crowding Serves as a Scaffold for Tissue Engineering. *Advanced Healthcare Materials*. 2021;10(11). doi:10.1002/adhm.202100024

54. Johnson C, Sheshadri P, Ketchum JM, Narayanan LK, Weinberger PM, Shirwaiker RA. In vitro characterization of design and compressive properties of 3D-biofabricated/decellularized hybrid grafts for tracheal tissue engineering. *Journal of the Mechanical Behavior of Biomedical Materials*. 2016;59:572-585. doi:10.1016/j.jmbbm.2016.03.024
55. Önnerfjord P, Khabut A, Reinholt FP, Svensson O, Heinegård D. Quantitative proteomic analysis of eight cartilaginous tissues reveals characteristic differences as well as similarities between subgroups. *Journal of Biological Chemistry*. 2012;287(23):18913-18924. doi:10.1074/jbc.M111.298968
56. Mahzoon S, Detamore MS. Chondroinductive Peptides: Drawing Inspirtations from Cell-Matrix Interactions. 2019;25(3):249-257. doi:https://doi.org/10.1089/ten.teb.2018.0003
57. Kim YS, Majid M, Melchiorri AJ, Mikos AG. Applications of decellularized extracellular matrix in bone and cartilage tissue engineering. *Bioengineering & Translational Medicine*. 2019;4(1):83-95. doi:10.1002/btm2.10110
58. Sun Y, Yan L, Chen S, Pei M. Functionality of decellularized matrix in cartilage regeneration: A comparison of tissue versus cell sources. *Acta Biomaterialia*. 2018;74:56-73. doi:10.1016/j.actbio.2018.04.048
59. Rothrauff BB, Shimomura K, Gottardi R, Alexander PG, Tuan RS. Anatomical region-dependent enhancement of 3-dimensional chondrogenic differentiation of human mesenchymal stem cells by soluble meniscus extracellular matrix. *Acta Biomaterialia*. 2017;49:140-151. doi:10.1016/j.actbio.2016.11.046
60. Utomo L, Pleumeekers MM, Nimeskern L, et al. Preparation and characterization of a decellularized cartilage scaffold for ear cartilage reconstruction. *Biomedical Materials (Bristol)*. 2015;10(1). doi:10.1088/1748-6041/10/1/015010
61. Chang CH, Chen CC, Liao CH, Lin FH, Hsu YM, Fang HW. Human acellular cartilage matrix powders as a biological scaffold for cartilage tissue engineering with synovium-derived mesenchymal stem cells. *Journal of Biomedical Materials Research - Part A*. 2014;102(7):2248-2257. doi:10.1002/jbm.a.34897
62. Neill T, Schaefer L, Iozzo R V. Decoding the Matrix: Instructive Roles of Proteoglycan Receptors. *Biochemistry*. 2015;54(30):4583-4598. doi:10.1021/acs.biochem.5b00653
63. Zha K, Sun Z, Yang Y, et al. Recent developed strategies for enhancing chondrogenic differentiation of MSC: Impact on MSC-based therapy for cartilage regeneration. *Stem Cells International*. 2021;2021. doi:10.1155/2021/8830834
64. Schwarz S, Koerber L, Elsaesser AF, et al. Decellularized Cartilage Matrix as a Novel Biomatrix for Cartilage Tissue-Engineering Applications. *Tissue Engineering Part A*. 2012;18:120720085805006. doi:10.1089/ten.tea.2011.0705
65. Ma X, Yu C, Wang P, et al. Rapid 3D bioprinting of decellularized extracellular matrix with regionally varied mechanical properties and biomimetic microarchitecture. *Biomaterials*. 2018;185:310-321. doi:10.1016/j.biomaterials.2018.09.026

66. De Santis MM, Alsafadi HN, Tas S, et al. Extracellular-Matrix-Reinforced Bioinks for 3D Bioprinting Human Tissue. *Advanced Materials*. 2021;33(3). doi:10.1002/adma.202005476
67. Lin H, Yang G, Tan J, Tuan RS. Influence of decellularized matrix derived from human mesenchymal stem cells on their proliferation, migration and multi-lineage differentiation potential. *Biomaterials*. 2012;33(18):4480-4489. doi:10.1016/j.biomaterials.2012.03.012
68. Pouliot RA, Young BM, Link PA, et al. Porcine Lung-Derived Extracellular Matrix Hydrogel Properties Are Dependent on Pepsin Digestion Time. *Tissue Engineering - Part C: Methods*. 2020;26(6):332-346. doi:10.1089/ten.tec.2020.0042
69. Dequach JA, Yuan SH, Goldstein LSB, Christman KL. Decellularized porcine brain matrix for cell culture and tissue engineering scaffolds. *Tissue Engineering - Part A*. 2011;17(21-22):2583-2592. doi:10.1089/ten.tea.2010.0724
70. Freytes DO, Martin J, Velankar SS, Lee AS, Badylak SF. Preparation and rheological characterization of a gel form of the porcine urinary bladder matrix. *Biomaterials*. 2008;29(11):1630-1637. doi:10.1016/j.biomaterials.2007.12.014
71. Kusuma GD, Yang MC, Brennecke SP, O'Connor AJ, Kalionis B, Heath DE. Transferable Matrixes Produced from Decellularized Extracellular Matrix Promote Proliferation and Osteogenic Differentiation of Mesenchymal Stem Cells and Facilitate Scale-Up. *ACS Biomaterials Science and Engineering*. 2018;4(5):1760-1769. doi:10.1021/acsbiomaterials.7b00747
72. Poon CJ, Maria M v., Sinha S, et al. Preparation of an adipogenic hydrogel from subcutaneous adipose tissue. *Acta Biomaterialia*. 2013;9(3):5609-5620. doi:10.1016/j.actbio.2012.11.003
73. Wolf MT, Daly KA, Brennan-Pierce EP, et al. A hydrogel derived from decellularized dermal extracellular matrix. *Biomaterials*. 2012;33(29):7028-7038. doi:10.1016/j.biomaterials.2012.06.051
74. Rothrauff BB, Yang G, Tuan RS. Tissue-specific bioactivity of soluble tendon-derived and cartilage-derived extracellular matrices on adult mesenchymal stem cells. *Stem Cell Research and Therapy*. 2017;8(1):1-17. doi:10.1186/s13287-017-0580-8
75. Bennion BJ, Daggett V. The molecular basis for the chemical denaturation of proteins by urea. *Proceedings of the National Academy of Sciences of the United States of America*. 2003;100(9):5142-5147. doi:10.1073/pnas.0930122100
76. Beck EC, Barragan M, Tadros MH, Gehrke SH, Detamore MS. Approaching the compressive modulus of articular cartilage with a decellularized cartilage-based hydrogel. *Acta Biomaterialia*. 2016;38(785):94-105. doi:10.1016/j.actbio.2016.04.019
77. Khanlari A, Detamore MS, Gehrke SH. Increasing cross-linking efficiency of methacrylated chondroitin sulfate hydrogels by copolymerization with

oligo(ethylene glycol) diacrylates. *Macromolecules*. 2013;46(24):9609-9617. doi:10.1021/ma401838h

78. Hinton TJ, Jallerat Q, Palchesko RN, et al. Three-dimensional printing of complex biological structures by freeform reversible embedding of suspended hydrogels. *Science Advances*. 2015;1(9). doi:10.1126/sciadv.1500758
79. R Core Team. R: A Language and Environment for Statistical Computing. Published online 2016.
80. Solchaga LA, Penick KJ, Welter JF. Chondrogenic Differentiation of Bone Marrow-Derived Mesenchymal Stem Cells: Tips and Tricks. In: *Methods*. Vol 698. ; 2011:253-278. doi:10.1007/978-1-60761-999-4_20
81. Somoza RA, Welter JF, Correa D, Caplan AI. Chondrogenic differentiation of mesenchymal stem cells: Challenges and unfulfilled expectations. *Tissue Engineering - Part B: Reviews*. 2014;20(6):596-608. doi:10.1089/ten.teb.2013.0771
82. Varghese S, Hwang NS, Canver AC, Theprungsirikul P, Lin DW, Elisseeff J. Chondroitin sulfate based niches for chondrogenic differentiation of mesenchymal stem cells. *Matrix Biology*. 2008;27(1):12-21. doi:10.1016/j.matbio.2007.07.002
83. Li A, Wei Y, Hung C, Vunjak-Novakovic G. Chondrogenic properties of collagen type XI, a component of cartilage extracellular matrix. *Biomaterials*. 2018;173:47-57. doi:10.1016/j.biomaterials.2018.05.004
84. Kupfer ME, Lin WH, Ravikumar V, et al. In Situ Expansion, Differentiation and Electromechanical Coupling of Human Cardiac Muscle in a 3D Bioprinted, Chambered Organoid . *Circulation Research*. Published online 2020:207-224. doi:10.1161/circresaha.119.316155
85. Abbadessa A, Mouser VHM, Blokzijl MM, et al. A Synthetic Thermosensitive Hydrogel for Cartilage Bioprinting and Its Biofunctionalization with Polysaccharides. *Biomacromolecules*. 2016;17(6):2137-2147. doi:10.1021/acs.biomac.6b00366
86. Hinton TJ, Jallerat Q, Palchesko RN, et al. Three-dimensional printing of complex biological structures by freeform reversible embedding of suspended hydr(1) Hinton, T. J.; Jallerat, Q.; Palchesko, R. N.; Park, J. H.; Grodzicki, M. S.; Shue, H.-J.; Ramadan, M. H.; Hudson, A. R.; Feinberg, A. W. Thr. *Sci Adv*. 2015;1(October):1-10. doi:10.1126/sciadv.1500758
87. Abaci A, Guvendiren M. Designing Decellularized Extracellular Matrix-Based Bioinks for 3D Bioprinting. *Advanced Healthcare Materials*. 2020;2000734:1-18. doi:10.1002/adhm.202000734
88. Krüger T. *Computer Simulation Study of Collective Phenomena in Dense Suspensions of Red Blood Cells under Shear*. Vieweg+Teubner Verlag; 2012. doi:10.1007/978-3-8348-2376-2
89. Bentz DP, Ferraris CF, Galler MA, Hansen AS, Guynn JM. Influence of particle size distributions on yield stress and viscosity of cement-fly ash pastes. *Cement*

and Concrete Research. 2012;42(2):404-409. doi:10.1016/j.cemconres.2011.11.006
90. Skylar-Scott MA, Uzel SGM, Nam LL, et al. Biomanufacturing of organ-specific tissues with high cellular density and embedded vascular channels. *Science Advances*. 2019;5(9). doi:10.1126/sciadv.aaw2459
91. Beck EC, Barragan M, Libeer TB, et al. Chondroinduction from Naturally Derived Cartilage Matrix: A Comparison Between Devitalized and Decellularized Cartilage Encapsulated in Hydrogel Pastes. *Tissue Engineering - Part A*. 2016;22(7-8):665-679. doi:10.1089/ten.tea.2015.0546
92. Shirahama H, Lee BH, Tan LP, Cho NJ. Precise Tuning of Facile One-Pot Gelatin Methacryloyl (GelMA) Synthesis. *Scientific reports*. 2016;6(August):31036. doi:10.1038/srep31036
93. Zhang Z, Jin Y, Yin J, et al. Evaluation of bioink printability for bioprinting applications. *Applied Physics Reviews*. 2018;5(4). doi:10.1063/1.5053979
94. Lemarié L, Anandan A, Petiot E, Marquette C, Courtial EJ. Rheology, simulation and data analysis toward bioprinting cell viability awareness. *Bioprinting*. 2021;21:e00119. doi:10.1016/j.bprint.2020.e00119
95. Han S, Kim CM, Jin S, Kim TY. Study of the process-induced cell damage in forced extrusion bioprinting. *Biofabrication*. 2021;13(3). doi:10.1088/1758-5090/ac0415
96. Adair-Kirk TL, Senior RM. *Fragments of Extracellular Matrix as Mediators of Inflammation*. Vol 40.; 2008:1101-1110. doi:10.1016/j.biocel.2007.12.005
97. Galliger Z, Panoskaltsis-Mortari A. Tracheal Cartilage Isolation and Decellularization. In: Humana Press; 2017:155-160. doi:10.1007/7651_2017_52
98. Schindelin J, Arganda-Carreras I, Frise E, et al. Fiji: An open-source platform for biological-image analysis. *Nature Methods*. 2012;9(7):676-682. doi:10.1038/nmeth.2019
99. Lillie MA, Chalmers GWG, Gosline JM. The effects of heating on the mechanical properties of arterial elastin. *Connective Tissue Research*. 1994;31(1):23-35. doi:10.3109/03008209409005632
100. Lillie MA, Gosline JM. Mechanical properties of elastin along the thoracic aorta in the pig. *Journal of Biomechanics*. 2007;40(10):2214-2221. doi:10.1016/j.jbiomech.2006.10.025
101. Fedorov A, Beichel R, Kalpathy-Cramer J, et al. 3D Slicer as an image computing platform for the Quantitative Imaging Network. *Magnetic Resonance Imaging*. 2012;30(9):1323-1341. doi:10.1016/j.mri.2012.05.001
102. Delaere P, van Raemdonck D, Vranckx J. Tracheal transplantation. *Intensive Care Medicine*. 2019;45(3):391-393. doi:10.1007/s00134-018-5445-9
103. Klepetko W, Marta GM, Wisser W, et al. Heterotopic tracheal transplantation with omentum wrapping in the abdominal position preserves functional and structural integrity of a human tracheal allograft. *Journal of Thoracic and Cardiovascular Surgery*. 2004;127(3):862-867. doi:10.1016/j.jtcvs.2003.07.050

104. Delaere P, Goeleven A, Poorten V vander, Hermans R, Hierner R, Vranckx J. Organ preservation surgery for advanced unilateral glottic and subglottic cancer. *Laryngoscope*. 2007;117(10):1764-1769. doi:10.1097/MLG.0b013e3181238397
105. Delaere PR, Vranckx JJ, Dooms C, Meulemans J, Hermans R. Tracheal autotransplantation: Guidelines for optimal functional outcome. *Laryngoscope*. 2011;121(8):1708-1714. doi:10.1002/lary.21869
106. Loos E, Meulemans J, Vranckx J, Poorten V vander, Delaere P. Tracheal Autotransplantation for Functional Reconstruction of Extended Hemilaryngectomy Defects: A Single-Center Experience in 30 Patients. *Annals of Surgical Oncology*. 2016;23(5):1674-1683. doi:10.1245/s10434-015-5033-y
107. Tanaka H, Maeda K, Okita Y. Transplantation of the Cryopreserved Tracheal Allograft in Growing Rabbits. *Journal of Pediatric Surgery*. 2003;38(12):1707-1711. doi:10.1016/j.jpedsurg.2003.08.036
108. Shi H, Xu H, Lu D, Wu J. Animal models of tracheal allotransplantation using vitrified cryopreservation. *Journal of Thoracic and Cardiovascular Surgery*. 2009;138(5):1222-1226. doi:10.1016/j.jtcvs.2009.05.028
109. Hondt M den, Vanaudenaerde B, Verbeken E, Vranckx JJ. Requirements for successful trachea transplantation: A study in the rabbit model. *Plastic and Reconstructive Surgery*. 2018;141(6):845e-856e. doi:10.1097/PRS.0000000000004429
110. Jones MC, Rueggeberg FA, Faircloth HA, et al. Defining the Biomechanical Properties of the Rabbit Trachea. 2014;(October):2352-2358. doi:10.1002/lary.24739
111. Myer Iii CM. *PROPOSED GRADING SYSTEM FOR SUBGLOTTIC STENOSIS BASED ON ENDOTRACHEAL TUBE SIZES*. Vol 103.; 1994:319-323. doi:10.1177/000348949410300410
112. Sabatini F, Petecchia L, Tavian M, de Villeroché VJ, Rossi GA, Brouty-Boyé D. Human bronchial fibroblasts exhibit a mesenchymal stem cell phenotype and multilineage differentiating potentialities. *Laboratory Investigation*. 2005;85(8):962-971. doi:10.1038/labinvest.3700300
113. Borthwick DW, Shahbazian M, Todd Krantz Q, Dorin JR, Randell SH. *Evidence for Stem-Cell Niches in the Tracheal Epithelium*. Vol 24.; 2001. www.atsjournals.org
114. Radu DM, Seguin A, Bruneval P, Fialaire Legendre A, Carpentier A, Martinod E. Bronchial Replacement With Arterial Allografts. *Annals of Thoracic Surgery*. 2010;90(1):252-258. doi:10.1016/j.athoracsur.2010.03.079
115. Martinod E, Seguin A, Pfeuty K, et al. *Long-Term Evaluation of the Replacement of the Trachea With an Autologous Aortic Graft*.; 2003.
116. Seguin A, Martinod E, Kambouchner M, et al. Carinal replacement with an aortic allograft. *Annals of Thoracic Surgery*. 2006;81(3):1068-1074. doi:10.1016/j.athoracsur.2005.07.079

117. Martinod E, Seguin A, Holder-Espinasse M, et al. Tracheal regeneration following tracheal replacement with an allogenic aorta. *Annals of Thoracic Surgery*. 2005;79(3):942-948. doi:10.1016/j.athoracsur.2004.08.035
118. Martinod E, Chouahnia K, Radu DM, et al. Feasibility of bioengineered tracheal and bronchial reconstruction using stented aortic matrices. *JAMA - Journal of the American Medical Association*. 2018;319(21):2212-2222. doi:10.1001/jama.2018.4653
119. Zink R, Rees H, Heiny O. Bioreactor. Published online December 25, 2014.
120. Haykal S, Salna M, Zhou Y, et al. Double-Chamber Rotating Bioreactor for Dynamic Perfusion Cell Seeding of Large-Segment Tracheal Allografts: Comparison to Conventional Static Methods. *Tissue engineering Part C, Methods*. 2014;20(8):1-12. doi:10.1089/ten.TEC.2013.0627
121. Lin CH, Hsu S hui, Huang CE, Cheng WT, Su JM. A scaffold-bioreactor system for a tissue-engineered trachea. *Biomaterials*. 2009;30(25):4117-4126. doi:10.1016/j.biomaterials.2009.04.028
122. Asnaghi MA, Jungebluth P, Raimondi MT, et al. A double-chamber rotating bioreactor for the development of tissue-engineered hollow organs: From concept to clinical trial. *Biomaterials*. 2009;30(29):5260-5269. doi:10.1016/j.biomaterials.2009.07.018
123. Isenberg BC, Tranquillo RT. Long-term cyclic distention enhances the mechanical properties of collagen-based media-equivalents. *Annals of Biomedical Engineering*. 2003;31(8):937-949. doi:10.1114/1.1590662
124. Seliktar D, Black RA, Vito RP, Nerem RM. Dynamic Mechanical Conditioning of Collagen-Gel Blood Vessel Constructs Induces Remodeling In Virto. *Annals of Biomedical Engineering*. 2000;28:351-362.
125. Weidenhamer NK, Tranquillo RT. Influence of cyclic mechanical stretch and tissue constraints on cellular and collagen alignment in fibroblast-derived cell sheets. *Tissue engineering Part C, Methods*. 2013;19(5):386-395. doi:10.1089/ten.TEC.2012.0423
126. Jung JP, Sprangers AJ, Byce JR, et al. ECM-incorporated hydrogels cross-linked via native chemical ligation to engineer stem cell microenvironments. *Biomacromolecules*. 2013;14(9):3102-3111. doi:10.1021/bm400728e
127. Tran QA, Ajeti V, Freeman BT, Campagnola PJ, Ogle BM. Developmental pathways pervade stem cell responses to evolving extracellular matrices of 3D bioprinted microenvironments. *Stem Cells International*. 2018;2018. doi:10.1155/2018/4809673
128. Kreeger PK, Strong LE, Masters KS. Engineering Approaches to Study Cellular Decision Making. *Annual Review of Biomedical Engineering*. 2018;20:49-72. doi:10.1146/annurev-bioeng-062117-121011
129. Jung JP, Bache-Wiig MK, Provenzano PP, Ogle BM. Heterogeneous Differentiation of Human Mesenchymal Stem Cells in 3D Extracellular Matrix

Composites. *BioResearch Open Access*. 2016;5(1):37-48. doi:10.1089/biores.2015.0044
130. Armani M, Rodriguez-Canales J, Gillespie J, et al. 2D-PCR: A method of mapping DNA in tissue sections. *Lab on a Chip*. 2009;9(24):3526-3534. doi:10.1039/b910807f
131. Cummings BS, Schnellmann RG. Measurement of Cell Death in Mammalian Cells. *Current Protocols in Pharmacology*. 2004;25(1). doi:10.1002/0471141755.ph1208s25
132. Koelling S, Kruegel J, Irmer M, et al. Migratory Chondrogenic Progenitor Cells from Repair Tissue during the Later Stages of Human Osteoarthritis. *Cell Stem Cell*. 2009;4(4):324-335. doi:10.1016/j.stem.2009.01.015
133. Vinod E, Johnson NN, Kumar S, et al. Migratory chondroprogenitors retain superior intrinsic chondrogenic potential for regenerative cartilage repair as compared to human fibronectin derived chondroprogenitors. *Scientific Reports*. 2021;11(1):23685. doi:10.1038/s41598-021-03082-5
134. Dahl SLM, Kypson AP, Lawson JH, et al. Readily Available Tissue-Engineered Vascular Grafts. *Science Translational Medicine*. 2011;3(68). doi:10.1126/scitranslmed.3001426
135. Isenberg BC, Williams C, Tranquillo RT. Small-diameter artificial arteries engineered in vitro. *Circulation Research*. 2006;98:25-35. doi:10.1161/01.RES.0000196867.12470.84